The Pennsylvania State University

The Graduate School

SHIPBOARD HELICOPTER GUST RESPONSE ALLEVIATION USING ACTIVE TRAILING EDGE FLAPS

A Thesis in

Aerospace Engineering

by

Pamela L. Montanye

Submitted in Partial Fulfillment

of the Requirements

for the Degree of

Master of Science

August 2008

The thesis of Pamela L. Montanye was reviewed and approved* by the following:

Edward C. Smith
Professor of Aerospace Engineering
Thesis Co-Advisor

Christopher D. Rahn
Professor of Mechanical Engineering
Thesis Co-Advisor

Stephen C. Conlon
Assistant Professor of Aerospace Engineering
Thesis Co-Advisor

Joseph F. Horn
Associate Professor of Aerospace Engineering

George A. Lesieutre
Professor of Aerospace Engineering
Head of the Department of Aerospace Engineering

*Signatures are on file in the Graduate School.

Abstract

Helicopter shipboard launch and recovery operations can result in high pilot workload due to the unsteady, turbulent ship airwake. Successful gust response alleviation could improve safety and potentially expand operational envelopes. The results of a feasibility study of using active trailing edge flaps as gust alleviation mechanisms are presented. Previous researchers have used the primary flight control effectors, including the swashplate and the tail rotor, to successfully improve the vehicle response and reduce the pilot workload. Other researchers have analyzed trailing edge flaps for the purposes of vibration control, noise reduction, and blade loads control. Until now, time-domain, non-harmonic controllers have seen little use in automated on-blade actuation studies. Additionally, using on-blade actuation is a novel method for gust alleviation. The benefits of on-blade actuation and previous gust alleviation control methods are combined in this study, yielding a system that uses trailing edge flaps for gust disturbance rejection while the swashplate provides primary flight control.

The control architecture used in this analysis is comprised of two distinct controllers with separate actuators. The primary flight control system is a standard model-following controller (MFC) architecture that uses the swashplate and pedals to ensure that the vehicle follows a desired response to pilot inputs, based on handling qualities specifications. Separately, the airwake compensator rejects airwake disturbances with trailing edge flaps and a robust H_2 controller. In this way, command tracking is decoupled from disturbance rejection. The controller is

implemented in the GENHEL flight simulation code of the UH-60A Black Hawk with a CFD airwake solution for an LHA-class ship. Simulations are performed in hover. The size of the trailing edge flaps used in this study (fifteen percent blade span and twenty percent blade chord) is on the low range of the size of flaps studied for vibration control.

Results indicate that trailing edge flaps are capable of alleviating the magnitude of the vehicle angular gust response in the roll and pitch axes. Roll response is significantly impacted in all cases, including a roll rate reduction of as much as ninety percent in specific wind-over-deck conditions. Pitch response sees a modest improvement in all conditions. Specifically, in a hover maneuver above a Landing Helicopter Assault-class ship with a thirty knot wind from thirty degrees from the bow of the ship, the maximum roll rate response of the vehicle is reduced by ninety-one percent. The maximum pitch rate response is reduced by thirty-two percent using a trailing edge flap controller designed for that flight condition. Varying performance and actuation parameters within the control synthesis has a strong impact on the magnitude and frequency of the required trailing edge flap deflections. Deflection requirements can be kept below current actuation technology stroke and rate limits while achieving the performance of a similar swashplate-based controller. The results of this study suggest that trailing edge flaps can be effective for shipboard gust alleviation.

Table of Contents

List of Figures

List of Tables

List of Symbols

C_l	Blade section lift coefficient
$C_{l\alpha}$	Blade section lift curve slope
I_x, I_y, I_z	Vehicle moments of inertia
I_{xz}	Vehicle product of inertia
K_D	Derivative gain in a PID controller
K_I	Integral gain in a PID controller
K_P	Proportional gain in a PID controller
L	Vehicle roll moment about the center of mass
M	Mach number, or alternatively, vehicle pitch moment about the center of mass
$M_{vehicle}$	Total vehicle mass
N	Vehicle yaw moment about the center of mass
R	Rotor radius
$\underline{R}(\psi_k)$	Transformation matrix from fixed to rotating frame TEF deflections
$T_{1...15}$	Theodorsen geometric functions for quasi-steady analysis
$T_{z\omega}(s)$	Transfer function from ω to z
$\|T_{z\omega}(s)\|_2$	H_2 norm of the transfer function

TEF	Trailing edge flap
V	Local free stream velocity
$\underline{W}_{act}$	Actuator weighting functions
$\underline{W}_{p}$	Performance weighting functions
X	Longitudinal external force on the vehicle center of mass
Y	Lateral external force on the vehicle center of mass
Z	Vertical external force on the vehicle center of mass
b	Rotor blade semi-chord
b_f	Trailing edge flap span
c	Rotor blade chord
c_f	Trailing edge flap chord
g	Gravitational acceleration
k	Reduced frequency, or alternatively, rotor blade reference number
j	Imaginary number, $j = \sqrt{-1}$
p	Vehicle roll rate
q	Vehicle pitch rate
r	Vehicle yaw rate
u	Vehicle longitudinal translational velocity
$\vec{u}$	Control vector, or alternatively, outputs of the system or controller design
v	Vehicle lateral translational velocity
w	Vehicle vertical translational velocity
$\vec{w}$	Gust disturbance vector
$\vec{x}$	State vector

x_c TEF location from the center of the blade chord, non-dimensionalized with respect to blade semi-chord

x_f TEF location from the blade leading edge, non-dimensionalized with respect to chord

$\vec{z}$ Performance variable used in controller design

ΔC_l Change in local blade section lift coefficient due to TEF deflection

$\Delta C_{l_{circ}}$ Circulatory portion of the change in blade section lift coefficient due to TEF deflection

$\Delta C_{l_{non-circ}}$ Non-circulatory portion of the change in blade section lift coefficient due to TEF deflection

Ω Rotor rotational velocity

α Blade section effective angle of attack

β Blade flapping angle, or alternatively, Glauert compressibility factor

δ_f Trailing edge flap deflection angle

$\dot{\delta}_f$ Trailing edge flap deflection velocity

δ_f^k Trailing edge flap deflection angle of the k^{th} blade

δ_0 Collective trailing edge flap deflection

δ_{1C} Lateral TEF deflection

δ_{1S} Longitudinal TEF deflection

δ_2 Differential TEF deflection

δ_{lat} Lateral cyclic control stick deflection

δ_{long} Longitudinal cyclic control stick deflection

δ_{ped} Pedal deflection

$\vec{\nu}$ Pseudo-commands

ω Frequency of oscillation

ω_n	Natural frequency
ϕ	Vehicle roll attitude
ψ	Vehicle yaw attitude
ψ_k	Azimuthal location of blade number k
θ	Blade section pitch angle, or alternatively, vehicle pitch attitude
θ_0	Blade section collective pitch angle
θ_{1C}	Blade section lateral pitch angle
θ_{1S}	Blade section longitudinal pitch angle
θ_2	Blade section differential pitch angle
ζ	Damping ratio
$\dot{a}$	Derivative of a with respect to time
$\underline{A}$	Matrix quantity of A
$A(s)$	Transfer function
$\vec{a}$	Vector quantity of a
$\vec{a}_{cmd}$	Commanded value of a, based on pilot input
$\vec{a}_c$	Ideal value of a, based on ideal response model

Acknowledgments

This project was sponsored by the Office of Naval Research Grant Number N00014-06-1-0205 and the Applied Research Laboratory at the Pennsylvania State University Exploratory and Foundational Program.

Several faculty here at Penn State contributed to this project, and I am thankful to all of them. The project could not have been possible without the creativity and supervision of my advisor, Dr. Smith. Having Dr. Rahn join the project was a blessing. Many enjoyable discussions with him led to increased clarity and new approaches. I am very grateful to Dr. Horn for the time and effort he spent teaching me about the controller and the simulation facilities, which were crucial to this project. Additionally, I would like to thank Dr. Conlon at the Applied Research Lab for his continuous support of the project and my education.

A graduate education would not be complete without learning much from your coworkers. Thank you Sade Sparbanie, Conor Marr, Jason Steiner, Russ Rufino, Jamie Bluman, and Kirsten Bossenbroek. Also, thanks to those coworkers and friends for the emotional support that keeps me smiling.

Lastly, thank you to my parents. Without the support you gave me when I was younger, I would not be at this stage of my life now.

Chapter 1

Introduction

1.1 Background and Motivation

1.1.1 Challenges of Shipboard Operations

Operation near a ship remains one of the more challenging and workload-intensive helicopter flight regimes. The unsteady flow field, turbulence, and high frequency gust content found in ship airwakes contribute to the antagonistic environment. Additionally, the tasks performed within this environment are often high precision maneuvers, such as landing, takeoff, and station-keeping. These missions are referred to as shipboard dynamic interface (DI) operations.

Because DI operations can involve a combination of high-precision tasks and a degraded flight environment, limits are imposed on operations based on flight conditions for safety. The allowable flight conditions are based on several aspects: relative wind speed, azimuth angle, the particular ship/aircraft combination, and landing spot. For each vehicle combination, the limits are combined into Wind-over-Deck (WOD) envelopes (or Ship Helicopter Operating Limits (SHOL) in the U.K., Canada, and Australia), which indicate that the helicopter is permitted to

operate when the combination of WOD angle and speed is within the envelope. An example of a WOD envelope is shown in Figure 1.1. To create the envelopes, flight simulations and extensive flight tests are performed.

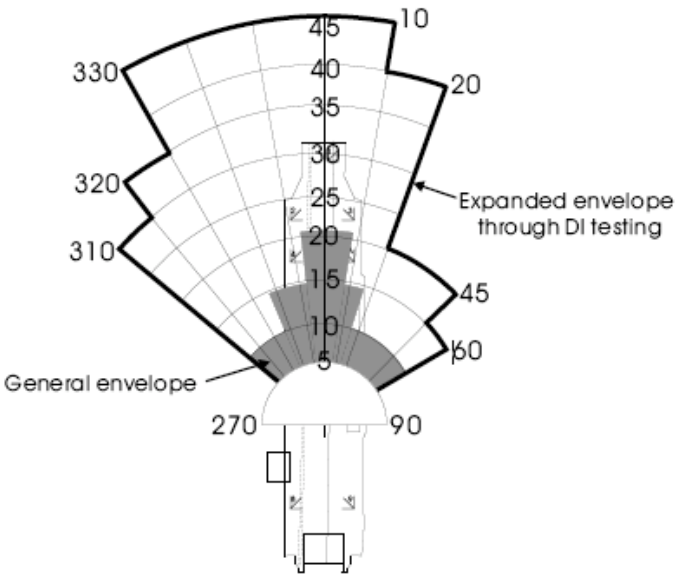

Figure 1.1. Typical WOD Envelope [1]

If improvements in helicopter safety or reductions in pilot workload could be realized, WOD envelopes could be expanded, increasing the helicopter's operational capabilities. Thus, there has been much research in alleviating the helicopter's response to the gusts found in ship airwakes. These methods include altered flight control systems that attempt to reject gust disturbances automatically by compensating for the airloads in the ship airwake. Some researchers have proposed higher levels of flight controller augmentation [2] and feedback loop optimization [3], [4]. More recent research has proposed a modern model-following control law architecture [5].

1.1.2 Current Helicopter Control Methods

To date, shipboard gust alleviation research has involved using the existing control surfaces and effectors on the vehicle. On a helicopter with the traditional configuration of a main rotor plus a tail rotor, the swashplate, illustrated in Figure 1.2, provides control in the lateral, longitudinal, and vertical axes. The tail rotor provides yaw control. On the main rotor, each blade is able to change its pitch. Collective pitch – when all the blades increase or decrease in pitch simultaneously – is a means for changing the magnitude of the thrust on the rotor. Cyclic pitch provides lateral and longitudinal control by altering the blade pitch so that one side of the rotor produces more lift than the other side.

Figure 1.2. AH-64A Main Rotor Hub Assembly [6]

While the swashplate is used for primary flight control in the traditional sense, new control methods and surfaces are being explored for a variety of purposes. Methods most pertinent to this study are those that utilize individual blade control (IBC). IBC involves controlling the behavior, usually associated with the lift or pitching moment, of the main rotor blades individually. It can be achieved by altering the blade pitch of each blade independent of the other blades, or by placing a control surface on each blade. The tailoring of the aerodynamic environment of each blade individually can lead to potential reductions in vibration, blade loads,

and noise. Currently, IBC has not been studied extensively for gust alleviation; however, its possibilities should be noted and warrant exploration.

1.1.3 Potential Advantages of Using Trailing Edge Flaps

Although the current control effectors on the vehicle have shown promise for alleviating gust response, using a separate control surface located on the rotor blades could have added advantages. One such choice of on-blade actuation is the trailing edge flap (TEF). Illustrations of TEFs are shown in Figures 1.3 – 1.4. Since trailing edge flaps are significantly smaller than the swashplate, they can move at much higher frequencies than the swashplate can. Additionally, they can provide individual blade control, yielding as many separate control surfaces as there are rotor blades. For these reasons, they have been studied for vibration reduction for many years [7], [8], [9], [10], and they have shown promise for blade loads control [11] and noise reduction [12], [13] as well. This study seeks to extend their usage into the realm of gust alleviation.

Figure 1.3. Rotor Blade with Trailing Edge Flap Developed by the Boeing Co. [14]

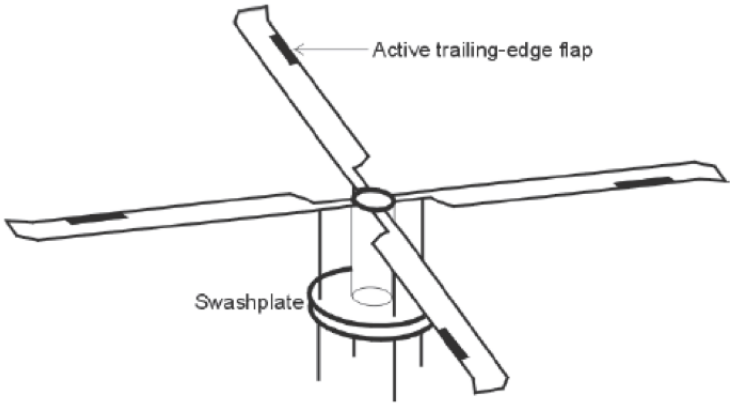

Figure 1.4. Schematic of TEF and Swashplate System [11]

1.2 Literature Survey

In order to study the ability of trailing edge flaps to alleviate helicopter gust response, a review of helicopter flight dynamics modeling as well as trailing edge flap usage and modeling techniques is required. This section provides a brief background on these subjects.

1.2.1 Helicopter Modeling and Shipboard Operations

1.2.1.1 Background on Helicopter Flight Dynamics Modeling

Helicopter behavior is both highly nonlinear and complex, resulting in the need to simplify the description of the helicopter motion in numerical and analytical modeling. Helicopter flight dynamics models must include the dynamics, aerodynamics, and kinematics of the vehicle and its subsystems, which include the main rotor, fuselage, empennage, tail rotor, power plant, and primary flight control system [15]. The various components of a helicopter model are shown in Figure 1.5.

To simplify the analysis and computational requirements, the model used for

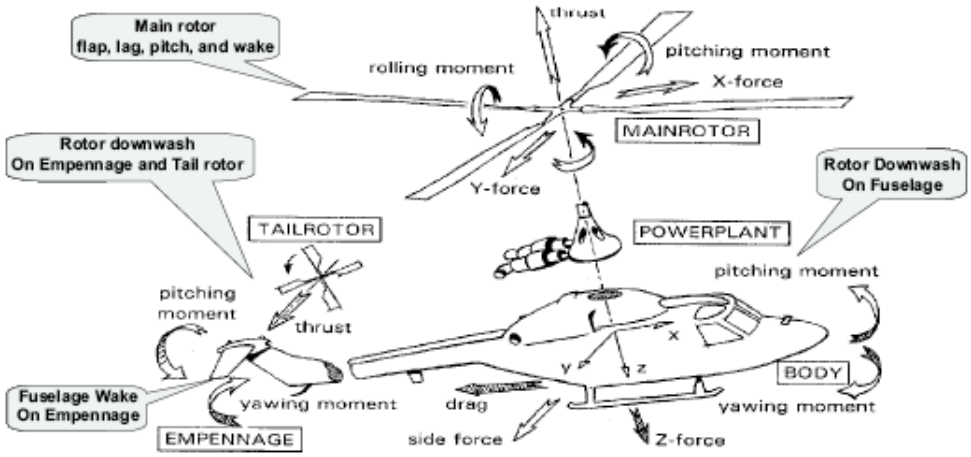

Figure 1.5. Components of a Helicopter Model [16]

flight control design and flight dynamics modeling is often reduced to a six degree-of-freedom (DOF) model that includes the rigid body translational and rotational velocity components. The translational and rotational equations of motion are

$$\begin{aligned}
\dot{u} &= \frac{X}{M_{vehicle}} - qw + rv - g\sin\theta, \\
\dot{v} &= \frac{Y}{M_{vehicle}} - ru + pw + g\cos\theta\sin\phi, \\
\dot{w} &= \frac{Z}{M_{vehicle}} - pv + qu + g\cos\theta\cos\phi, \\
\dot{p} &= \frac{L}{I_x} + \frac{I_y - I_z}{I_x}qr + \frac{I_{xz}}{I_x}(\dot{r} + pq), \\
\dot{q} &= \frac{M}{I_y} + \frac{I_z - I_x}{I_y}pr + \frac{I_{xz}}{I_y}(r^2 - p^2), \\
\dot{r} &= \frac{N}{I_z} + \frac{I_x - I_y}{I_z}pq + \frac{I_{xz}}{I_z}(\dot{p} - rq).
\end{aligned} \tag{1.1}$$

The equations for the Euler angles are

$$
\begin{aligned}
p &= \dot{\phi} - \dot{\psi}\sin\theta, \\
q &= \dot{\theta}\cos\phi + \dot{\psi}\sin\phi\cos\theta, \\
r &= -\dot{\theta}\sin\phi + \dot{\psi}\cos\phi\cos\theta.
\end{aligned}
\tag{1.2}
$$

1.2.1.2 Overview of the GENHEL Simulation Model

The flight dynamics model that is used in this research is the GENHEL (General Helicopter) flight dynamics simulation code, which was originally developed by Sikorsky Aircraft and documented under contract by NASA [17]. This nonlinear model simulates the UH-60A Black Hawk helicopter via a time-domain, iterative solution.

GENHEL includes many of the helicopter components. The overall block diagram for the simulation is shown in Figure 1.6. The vehicle motion is determined by iteratively summing the six forces and moments acting on the center of gravity and computing the vehicle accelerations. Additionally, the aerodynamics of the main rotor, fuselage, empennage, and tail rotor are included. Within the main rotor, rigid blade flapping, lagging, and hub rotational motion are modeled. The main rotor uses a blade element method with five equal annuli segments on each blade. Each segment's lift and drag are determined from wind tunnel data tables, based on local Mach number and angle of attack.

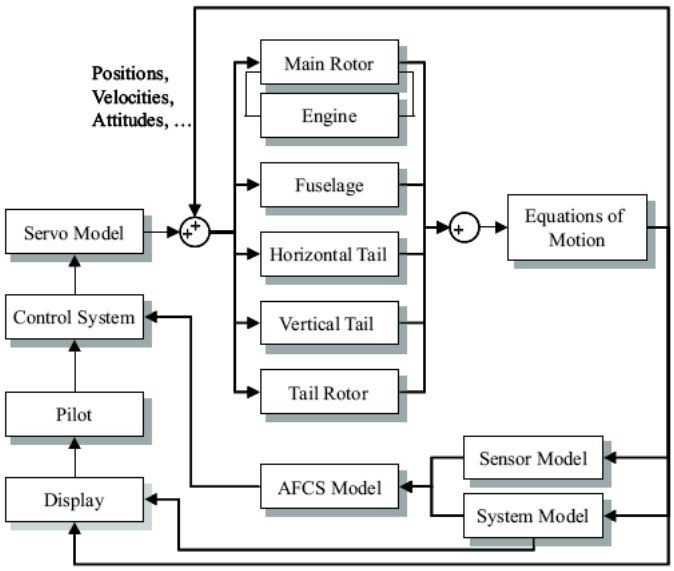

Figure 1.6. GENHEL Flight Simulation Model Block Diagram [17]

1.2.1.3 Modeling of a Ship Airwake and Helicopter Response

While modeling a helicopter by itself is a challenge, predicting its response to a ship airwake is significantly more daunting because it entails predicting the helicopter motion, the ship airwake, and their interactions. Properties of a ship airwake flowfield include unsteadiness, high vorticitiy, large regions of unseparated flow, and low Mach number. The turbulence in the flow can be higher than that found in natural wind [15]. All of this must be incorporated into a model that also includes the helicopter flight dynamics. An accurate model could have a variety of benefits. It could be used to train pilots, to reduce the number of required flight tests during the WOD evaluation process, and to help engineers design improved control systems. For these reasons, a number of programs have focused on developing accurate representations of the helicopter and airwake interface [18].

One of the most notable and recent programs focusing on the helicopter and ship airwake interface is the Joint Shipboard Helicopter Integration Process

(JSHIP). Overall, JSHIP is used to investigate the complexities (such as procedures, training, and compatibility) of using helicopters on Navy ships that were not specifically designed for that purpose. The Dynamic Interface Modeling and Simulation System (DIMSS) was developed in order to evaluate WOD envelopes for these aircraft [15]. Although many more modeling advances are necessary before developing operational envelopes from flight simulation can become a standard process, incorporating airwake models in simulation is becoming more common.

In order to represent the ship airwake in a flight simulation model, the airwake can be investigated in a few different ways: through full-scale testing, model-scale testing, and simulation. Although it is the most accurate, full-scale testing is very expensive and time-consuming. Though less expensive, model-scale testing can still be costly and adds complexities associated with proper scaling of the model and the aerodynamic environment. Thus, using CFD validated by some full-scale test data is common.

However, the large quantity of CFD data necessary to represent an airwake can be prohibitive for real-time implementation in a simulation environment. Thus, recent studies [19], [20], [21] have investigated using equivalent disturbance models to determine helicopter gust response without requiring extensive data storage. For shipboard operations, stochastic models that are similar to classical atmospheric turbulence models can be derived. The airwake properties and the corresponding disturbances on the vehicle motion are then extracted. Based on pilot comments, simplified stochastic models of the airwake are not significantly different than the complex CFD model. Thus, they are suitable for real-time use [20]. Additionally, there is another benefit of using stochastic models that include the spectral characteristics of the airwake: those characteristics can be used to design flight control systems specifically for airwake disturbance rejection [15].

A series of studies conducted by Lee, et al. [18] investigated tuning the flight control system based on the equivalent disturbance models. Stochastic disturbance models are used in the control design; the method for extracting the airwake properties was based on the method developed by Lusardi, et al. [21]. The helicopter and ship airwake interface models used by Lee, et al. are also used in this study. Like the JSHIP program, the study uses a UH-60A Black Hawk and a landing helicopter assault (LHA) class ship. The flow over the ship was computed using the parallel unstructured maritime aerodynamics CFD solver (PUMA2). The temporal and spatial variations of the flow are incorporated into the GENHEL flight dynamics model. A high-order Peters-He inflow model and a gust penetration model are also added. Local gust disturbances caused by the airwake are included at various locations along the aircraft. The airwake flowfield contributes to the helicopter's distributed inflow, downwash, and sidewash aerodynamics; however, the effects of the rotor wake on the ship airwake are not modeled [18].

1.2.1.4 Methods of Gust Alleviation

Armed with a high fidelity model of the helicopter and ship airwake interface, researchers can investigate methods of alleviating the helicopter gust response and high pilot workload. One method is to use higher levels of augmentation in the automatic flight control system [2]. Another method is to optimize the feedback loops specifically for gust rejection in a ship airwake. Lee, et al. [4] developed a modified limited authority Stability Augmentation System (SAS). This modified SAS incorporates the spectral properties of the airwake into the design of a robust airwake compensator by using the stochastic representation of the airwake to tune the controller. The compensator was tested with the GENHEL model of the UH-60A hovering above an LHA-class ship in a 30-degree, 30-knot wind-over-deck

condition. Flight tests of the baseline aircraft had shown that this WOD condition results in unacceptably high pilot workload. The modified SAS resulted in significant angular rate reduction and control activity reduction, as evidenced in Figure 1.7. The closed loop response to pilot inputs was altered, however [4]. For instance, if the pilot gave a control input at the same frequency as the gust model, the compensator would also try to reject the pilot input.

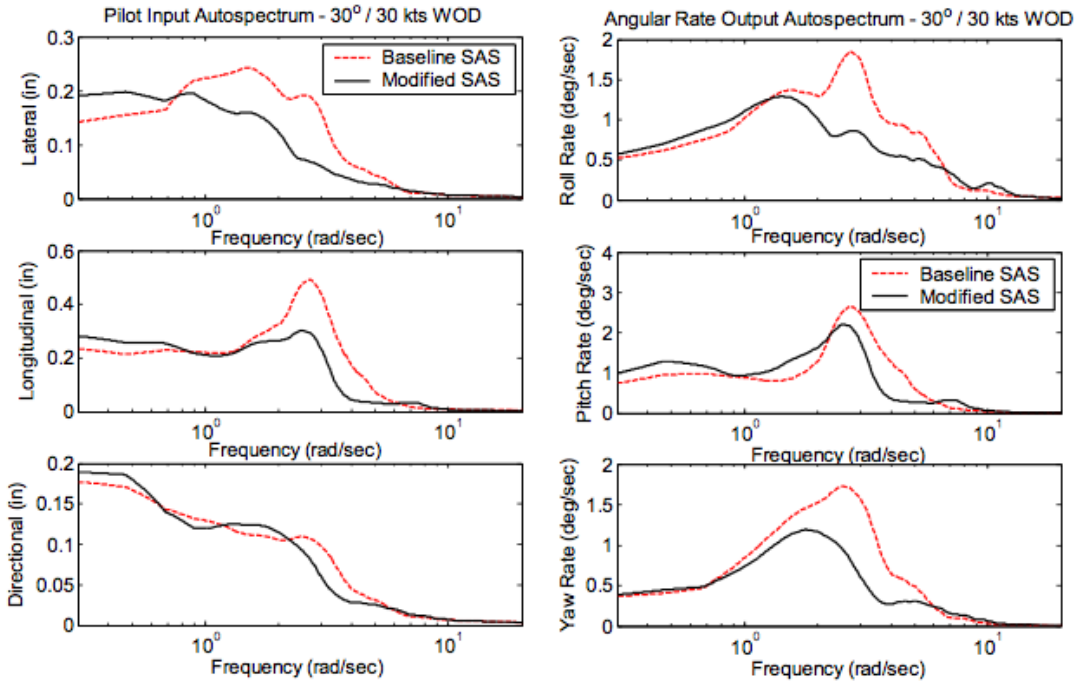

Figure 1.7. Autospectra of Pilot Inputs and Angular Rates, 30-deg/30-kt WOD with Modified SAS [5]

In order to differentiate between desired pilot input and undesired gust disturbances, a model-following control (MFC) architecture was developed by Horn et al. [5]. This is a full-authority controller that uses handling qualities specifications to determine the ideal response of the helicopter to the pilot input. The model-following controller and the airwake compensator operate on the tracking error

between the observed response and the actual response. Vehicle gust response and pilot control activity are reduced significantly while pilot command interference is minimized [5]. The reduction in vehicle angular rates caused by the airwake compensator is evident in Figure 1.8, which shows the time history of vehicle angular rates for a hover maneuver in a 30-degree, 30-knot wind. This architecture is also used in this research and will be discussed in detail in Chapter 3.

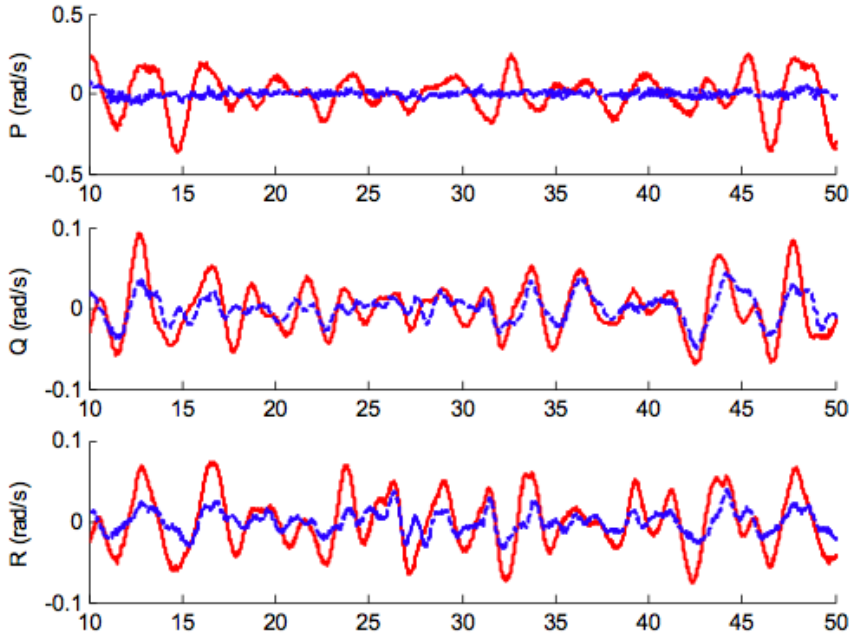

Figure 1.8. Hover Maneuver – Airwake Compensator Comparisons with MFC [5]

1.2.2 Trailing Edge Flaps

1.2.2.1 Current Applications of On-Blade Control

While gust alleviation is a novel use for trailing edge flaps, they have been studied for other purposes. The most extensively studied use for TEFs is vibration reduction. The benefits of reduced vibration are clear: decreased structural fatigue on

the rotor blade, hub, control system, and fuselage, as well as improved passenger comfort. Many analytical and experimental studies have shown that TEFs are able to reduce vibration [7], [8], [9], [10]. Other purposes of TEFs include blade loads control [11], noise reduction [12], [13], and primary flight control [22], [23], [24].

Many researchers have performed analytical studies on the effectiveness of trailing edge flaps for varying purposes. For example, Milgram [10] used 3/rev and 4/rev flap commands through an open-loop controller in order to predict a 98 percent reduction in vertical hub shear load in addition to vibration reduction. In support of a full-scale rotor test program, Straub and Charles [25] investigated vibration and noise control as well as aerodynamic performance and actuation needs and effects. Kim [11] simulated multiple trailing edge flaps on a single rotor blade in order to achieve both blade loads and vibration control. By commanding the flaps to straighten the blade, he predicted bending moment reductions of 32 percent and vibratory hub load reductions of 57 percent. Liu, et al. [9] studied both single and dual flap configurations for simultaneous vibration and rotor shaft power reduction using 2 – 5/rev harmonic flap commands. The largest reductions were found at higher rotor thrust and advance ratio. In another study, Liu, et al. [12] used the flaps to reduce blade-vortex interaction (BVI) noise.

Swashplateless rotor studies, which use trailing edge flaps for primary flight control, seek to eliminate the high maintenance and heavy swashplate from the rotor. This purpose requires substantially higher flap authority, which can surpass the capabilities of available actuators in some flight conditions. While vehicle trim is achievable with trailing edge flaps [23], maneuverability requirements necessitate another control surface, such as a moveable horizontal tail, as proposed by Bluman [22].

While the studies discussed so far have been analytical and computational studies that seek to extend the capabilities of active trailing edge flaps, there have been practical implementations of related concepts. In particular, the Kaman Corporation has used servo-flaps (flaps that extend beyond the trailing edge of the blade) for primary flight control by allowing the servo-flaps to control the blade pitch. Although it is much smaller and lighter than most swashplates, a swashplate is still used to move the servo-flap control assemblies. This concept has been used on each of Kaman Corporation's aircraft, including the SH-2 Seasprite, a U.S. Navy vehicle that has been in service since 1967. Additionally, trailing edge flaps and their actuation system have been whirl tower tested by Boeing with the full-scale Smart Material Actuated Rotor Technology (SMART) system [14]. Eurocopter [8] flight tested a vehicle with the ADASYS rotor system, which uses active trailing edge flaps for vibration and noise reduction.

These studies suggest that trailing edge flaps can be useful for a variety of purposes. It is possible that the same TEFs on a single rotor could accomplish more than one of these goals. For instance, vibration reduction would be most beneficial in high speed flight, while gust alleviation is necessary only in the low speed and hover regimes. Thus, the same flaps could be programmed for both purposes, providing more use for the flaps and more benefits.

1.2.2.2 Modeling of Trailing Edge Flaps

In order to predict the benefits of trailing edge flaps, an analytical model that includes the TEFs' aerodynamic effects must be incorporated. Various modeling techniques are used among researchers. The most complete model would predict lift, drag, and pitching moment caused by the flaps, as well as include compressibility, unsteadiness, and flow separation effects. However, the aerodynamic en-

vironment of the rotor is complex to model. Simplified aerodynamic models are often used. The type of model used can depend on the expected frequency of the TEF motion, with higher frequency motion requiring more comprehensive models due to phase attenuation.

Theodorsen extended thin airfoil theory to include trailing edge flaps and unsteady effects [26] and to provide a relatively simple solution for predicting the aerodynamic environment. However, his work is based in the frequency domain, which makes it difficult to apply his solution directly to TEFs with non-sinusoidal motions. If the reduced frequency is low enough, a quasi-steady version of his method can be used [27]. Most researchers include the Glauert factor when using Theodorsen methods in order to account for compressibility effects. Other researchers also include modifications based on experimental values for lift, drag, and pitching moment predictions [22].

When modeling TEFs for purposes that require higher rates of deflection, such as vibration reduction, unsteady effects become increasingly important. Researchers have developed more inclusive models that are suitable for rotorcraft applications. Leishman [28] developed an indicial method in the time domain that captures non-sinusoidal flap and airfoil motion, brief aerodynamic phenomena, and transients due to wind gusts. Hariharan and Leishman [29] extended the method to include both compressible and unsteady effects. Other researchers have expanded upon this work. Jose and Baeder [30] included time-varying freestream velocities but have not included trailing edge flaps. Myrtle and Friedmann [31] used Laplace transform methods to develop a rational function approximation of the time-varying freestream, compressible, unsteady loads on a flapped airfoil. Although these methods are more accurate, the difference between a quasi-steady Theodorsen-based model and a more complex model may be sufficiently small for

the environment the TEFs encounter during gust alleviation. This will be discussed further in Chapter 2.

1.2.2.3 Actuation Capabilities of Trailing Edge Flaps

The size, weight, and capabilities of available trailing edge flap actuation systems dictate how much and how fast the flaps can deflect. Piezo-electric benders can deflect up to five degrees at rates of up to 40 Hertz, but the TEF size is limited to one to five inches [32]. Thus, they are not powerful enough for gust alleviation on a full-scale rotor.

Piezo stack actuators are a more viable alternative. They are able to produce larger forces, but they require an amplification device in order to provide sufficient stroke. Several types of amplifiers have been developed. A full-scale MDART rotor was tested at Boeing. It uses a double X-frame amplification scheme to deflect the trailing edge flaps ± 3.5 degrees [33]. Trailing edge flaps on a rotor built by Eurocopter are able to deflect ± 5.0 degrees with an 11 percent span flap [8]. Another amplifying device in development, shown in Figure 1.9, is built by Szefi [34] and uses a buckling beam actuator. Based on smaller scale testing and analysis, Szefi predicts deflections of four degrees on a three-foot flap. In the current study, the commanded trailing edge flap deflections will be kept within the ranges of current actuation technology.

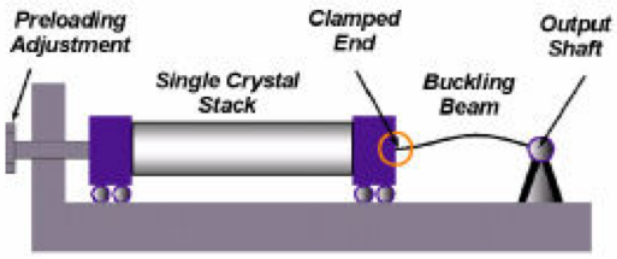

Figure 1.9. Buckling Beam Actuation Device Developed by Szefi [34]

1.3 Focus of Current Research

Combining the current trailing edge flap technology with gust alleviation control methods could result in a new, improved controller. The capabilities of using trailing edge flaps for helicopter gust alleviation are explored in this study. First, an appropriate trailing edge flap aerodynamic model is added to the GENHEL flight dynamics model. Then, the authority of the trailing edge flaps over the vehicle motion is evaluated in order to size the flaps. Airwake compensation control methods that incorporate the airwake spectral properties are applied.

A variety of control parameters as well as flap sizes and locations are simulated in order to determine their effects on helicopter gust response rejection and required trailing edge flap motions. Then, the performance of the resulting controller is evaluated for various wind conditions in hover in a ship airwake. Performance of the controllers is based on the vehicle angular motion reduction that can be achieved while keeping the trailing edge flap deflection magnitudes below five degrees. The trailing edge flap controller performance is compared to that of a similar swashplate-based airwake compensator.

Chapter 2

Trailing Edge Flap Model and Authority

2.1 Trailing Edge Flap Model

The first task in studying the feasibility of using active trailing edge flaps for helicopter gust alleviation is to implement a model of the TEF to be used in simulation. This section details the selection of flap type and the development of the appropriate numerical model.

2.1.1 Choice of Trailing Edge Flap Type

Based on their primary aerodynamic effect, trailing edge flaps used in rotorcraft vibration control, blade loads, noise reduction, and primary control studies can be classified into two broad categories: lift flaps and moment flaps. Lift flaps affect rotor forces and moments by increasing or decreasing the local blade section lift, whereas moment flaps primarily alter the blade pitching moment. In reality, any trailing edge flap will affect both the local blade section lift and the pitching moment. The degree to which each is affected depends on the stiffness of the rotor hub-blade system.

The choice of which type of trailing edge flap to use depends on physical

characteristics of the system as well as the required magnitude of changes in rotor forces and moments due to the TEF deflection. Due to the combined effects of increased pitching moment and lift, moment flaps are able to impart a larger change in blade forces than lift flaps for a given flap deflection. However, moment flaps require that the pitch link or blade torsional stiffness be low enough that the TEF can produce the required moment by either causing a change in pitch at the root or by twisting the blade. Thus, although moment flaps can be more powerful, there are hub-rotor design requirements associated with their use.

The balance of available authority and design necessities must be considered when selecting what type of flap to use. Studies of swashplate-less rotors that use trailing edge flaps for primary flight control use moment flaps because of the high required authority [22]. Trailing edge flap applications that require less authority can use lift flaps and assume that the pitching moment is minimally altered. Because gust alleviation requires forces that are small relative to the total vehicle forces and moments, lift flaps are used in this study. In addition to eliminating the need for a torsionally soft blade or pitch link, using lift flaps for this feasibility analysis provides the added benefit that should the use of lift flaps be successful, control schemes for moment flaps – with their larger ability to impact rotor forces – could also be tailored for gust alleviation.

2.1.2 Aerodynamic Model

The trailing edge flap model used in this initial TEF gust alleviation study includes the effect of flap deflections on the local blade section lift coefficient. With a lift flap, the magnitude of the change in rotor forces due to the lift force is much greater than other aerodynamic or inertial forces caused by the TEF motion, since it is

assumed that the flap can have relatively little impact on blade pitching moment. Subsequent analyses could add TEF drag and pitching moment.

In this study, a Theodorsen-based quasi-steady aerodynamic model is used. A Theodorsen approach is only valid for incompressible flows, as it is based on thin airfoil potential flow theory. A flow can only be assumed to be incompressible when its Mach number, M, and reduced frequency, k, satisfy the following requirements [29]:

$$\begin{aligned} M &<< 1, \\ Mk &<< 1, \\ M^2k^2 &<< 1. \end{aligned} \tag{2.1}$$

The reduced frequency, k, is given by

$$k = \frac{\omega b}{V}, \tag{2.2}$$

in which ω is the frequency of oscillation, b is the blade semi-chord with $b = c/2$, and V is the free stream velocity. The value of the reduced frequency indicates the unsteadiness of the flow, as indicated in Table 2.1.2 [35].

Table 2.1. Approximation of Variation of Flow Unsteadiness with Reduced Frequency

Reduced Frequency	Level of Unsteadiness
$k = 0$	Steady
$0 < k \leq 0.05$	Quasi-steady
$0.05 < k < 0.2$	Unsteady
$k \geq 0.2$	Highly unsteady

The Theodorsen quasi-steady model is reasonably accurate for the aerodynamic environment that the trailing edge flaps will encounter during shipboard gust alleviation, and it is easier to implement numerically than an unsteady model. If

trailing edge flaps were added to a UH-60A Black Hawk, a TEF that is present from 70 to 85 percent blade span would see approximately Mach 0.57 at its outboard point while hovering at sea level with no wind. In order to account for occasionally higher Mach numbers and the associated compressibility effects, the Glauert factor is included. If the flap oscillates at five Hertz – the maximum expected frequency for gust alleviation – the maximum reduced frequency is 0.05 (at the inboard location of the flap). Most of the TEF operation is expected to occur within a much lower reduced frequency range.

Considering the maximum expected Mach numbers and reduced frequencies, a quasi-steady aerodynamic model that includes compressibility effects is sufficient. The method of Hariharan and Leishman [29] provides higher fidelity for modeling the aerodynamic and inertial effects of the TEFs. This method employs indicial functions that can also account for the hereditary loads caused by non-circulatory terms. Stevens [27] compared the Theodorsen incompressible theory with Hariharan and Leishman's subsonic compressible flow theory, as well as with experimental data. At $M = 0.5$ and $k = 0.098$, the difference in prediction of lift and moment coefficient was insignificant. Significant differences could be seen at $M = 0.768$ and $k = 0.268$ [27]. Trailing edge flaps used for gust alleviation will be operating close to the former Mach number and reduced frequency. Therefore, the simpler Theodorsen model is adequate. Chord-wise geometric parameters of the trailing edge flap used in this model are shown in Figure 2.1, in which

$$x_f = \frac{c - c_f}{c} \tag{2.3}$$

and

$$x_c = 2x_f - 1. \tag{2.4}$$

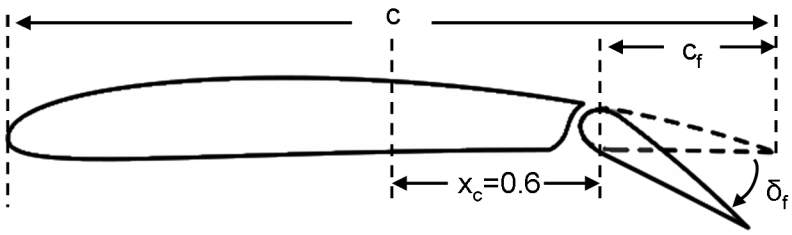

Figure 2.1. Geometric Parameters for Theordorsen Analysis

Theodorsen's method assumes an incompressible flow and is derived from thin airfoil theory. Equations for the lift of the whole airfoil are readily available in literature [22]. Since this study uses the GENHEL flight dynamics model, which already computes the lift of the unflapped airfoil via blade element theory and nonlinear aerodynamic table lookups, only the change in local blade segment lift coefficient due to the trailing edge flap motion is needed and detailed here. The change in local lift coefficient due to the TEFs includes circulatory terms as well as non-circulatory terms. The circulatory terms are given by

$$\Delta C_{l_{circ}} = \frac{1}{\beta}(2T_{10}\delta_f + \frac{b\dot{\delta}}{V}T_{11}). \tag{2.5}$$

The non-circulatory terms are

$$\Delta C_{l_{non-circ}} = \frac{-b\dot{\delta}}{V}T_4 - \frac{b^2\delta}{V^2}T_1, \tag{2.6}$$

which account for apparent mass effects. Normally, the circulatory terms in the frequency domain are scaled by Theodorsen's lift deficiency function, $C(K)$, which is a function of reduced frequency. However, the gust alleviation problem is non-

harmonic and solved in the time domain; therefore, it is not suited to this representation. $C(K)$ is assumed to be one in this study. The change in local blade section lift is then the sum of the circulatory and non-circulatory effects:

$$\Delta C_l = \Delta C_{l_{circ}} + \Delta C_{l_{non-circ}}. \tag{2.7}$$

Compressibility effects are included by the addition of the Glauert factor, β, where

$$\beta = \sqrt{1 - M^2}, \tag{2.8}$$

in which the local segment Mach number is used.

The geometric Theodorsen functions used in this analysis are dependent only on trailing edge flap chord-wise location. The remaining geometric Theodorsen functions can be found in reference [22]. The functions needed in this study are

$$T_1 = -\frac{1}{3}(2 + x_c^2)\sqrt{1 - x_c^2} + x_c \cos^{-1} x_c, \tag{2.9}$$

$$T_4 = x_c\sqrt{1 - x_c^2} - \cos^{-1} x_c, \tag{2.10}$$

$$T_{10} = \sqrt{1 - x_c^2} + \cos^{-1} x_c, \tag{2.11}$$

and

$$T_{11} = (2 - x_c)\sqrt{1 - x_c^2} + (1 - 2x_c)\cos^{-1} x_c. \tag{2.12}$$

In the numerical implementation, in any blade segment where the trailing edge flap is present, the change in lift is calculated at each time step by Eqn. 2.7 and added to the local blade segment lift. That change in lift subsequently affects the

vehicle motion by altering the total blade lift, which affects the forces produced at the hub and on the vehicle.

2.2 Authority Analysis

In order to quantify the effects of the trailing edge flap deflection on the vehicle motion and to determine the physical capabilities of using TEFs for gust alleviation, an authority analysis is performed. The goal of this analysis is two-fold. First, it is necessary to know that TEFs are able to impart as large of a change in forces and moments on a helicopter as the swashplate does when it has been used for gust alleviation in previous studies. Second, an authority analysis allows for the most accurate initial sizing and placement of the TEF.

To determine the authority of the trailing edge flaps, the aerodynamic model described in the previous section is implemented numerically within the GENHEL model, and the result of TEF deflection is compared to the result of cyclic pitch deflection. Because the tail rotor provides most of the authority in the yaw axis, only pitch and roll authorities are analyzed. The TEFs are given open-loop, harmonic, 1/rev commands so that

$$\delta_f = \delta_0 + \delta_{1C}\cos(\psi_k) + \delta_{1S}\sin(\psi_k). \tag{2.13}$$

The TEF deflections replicate the commands possible from the swashplate using cyclic pitch:

$$\theta = \theta_0 + \theta_{1C}\cos(\psi_k) + \theta_{1S}\sin(\psi_k). \tag{2.14}$$

The simulation is performed with the fuselage states frozen, as though the

vehicle is constrained in location and attitude. In this case, the fuselage does not translate or rotate, allowing the forces and moments that act on the rotor hub to be examined directly. For example, if one degree in lateral cyclic pitch is commanded, it causes a rolling moment at the rotor hub that would result in vehicle motion if it were not constrained; likewise, the application of longitudinal cyclic pitch causes a pitching moment. These values of hub moments are used throughout this authority analysis. The moment produced by the TEF is computed as the difference between the average of the steady-state moments after and before the TEF deflection was applied. An example of this change in moment is shown in Figure 2.2, in which the TEF is commanded at time $t = x$.

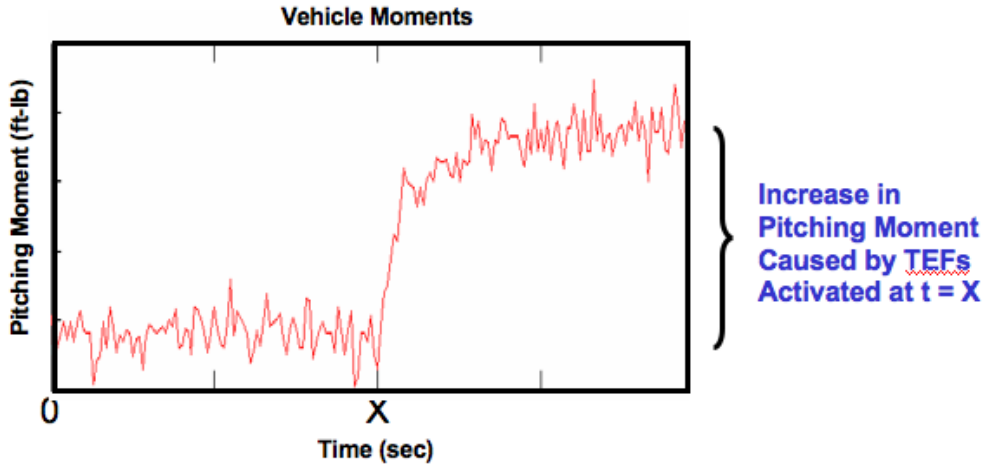

Figure 2.2. Change in Vehicle Moment Caused by a TEF

A study of variation of rotor moments produced by trailing edge flap deflection is performed. The TEF geometry is varied in span ratio ($\frac{b_f}{R}$), and non-dimensional inboard span-wise TEF location. The chord ratio ($\frac{c_f}{c}$) is set to 0.2 because this is a common chord size for trailing edge flaps; other sizes could be considered if necessary. All other settings in GENHEL are held constant throughout the analysis and are listed in Appendix A. In each iteration, a three-degree cyclic TEF

deflection is given; this is the maximum desired TEF deflection chosen, based on current actuation abilities described in Chapter 1. The resulting rotor moment, whose magnitude is indicated by color, caused by each TEF command is plotted in the following figures. Each contour plot demonstrates how the rotor moment varies with TEF span ratio (on the vertical axis) and TEF location (on the horizontal axis). For example, by looking at the black circle in Figure 2.3, one can see that a TEF that spans from 75 to 95 percent of the rotor blade radius can produce an approximately 2750 foot-pound rotor pitching moment a three-degree longitudinal deflection command.

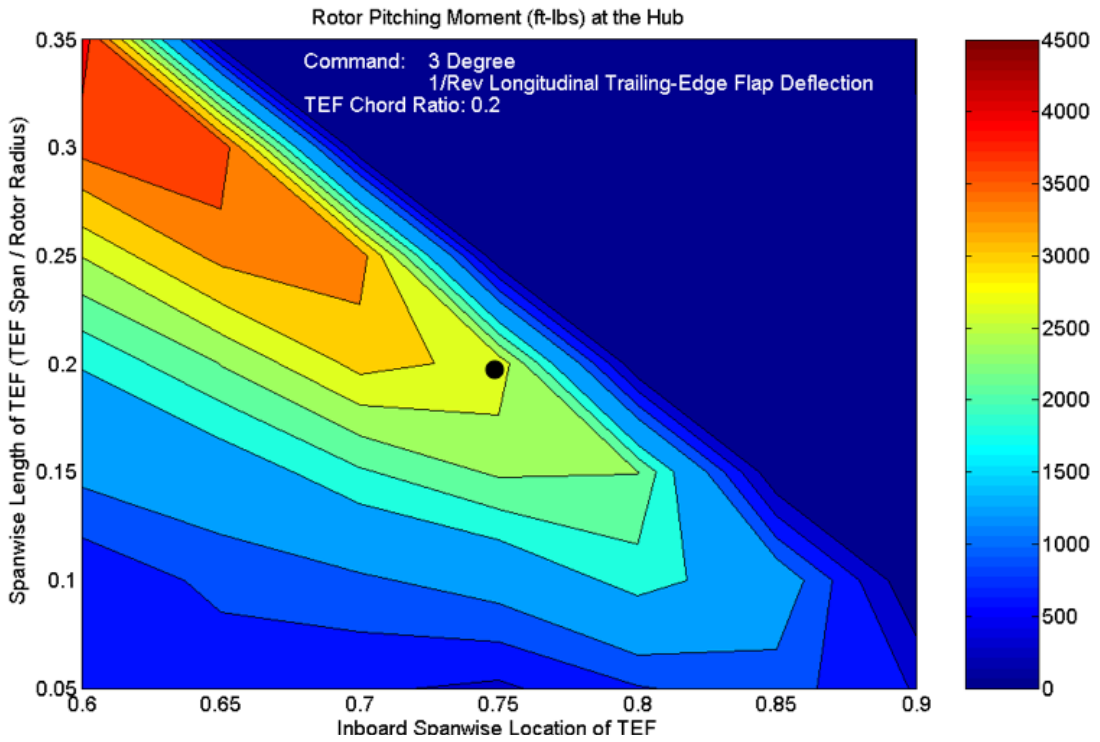

Figure 2.3. Example of Pitching Moment Authority of Trailing Edge Flaps

The required level of authority is chosen to be equal to the rotor moment produced by the maximum cyclic pitch deflections that have been used successfully in previous swashplate-based gust alleviation research performed by Horn, et al. [5].

Using the same simulation model, GENHEL, it is determined that the maximum deflection is approximately 0.5 degrees of cyclic pitch. Thus, by commanding this maximum deflection to GENHEL via the stick, the rotor moments necessary for gust alleviation are determined. These values are plotted on the contour plots as solid lines. Additionally, the moments produced by a full one-degree of cyclic pitch are shown. Plots illustrating the TEF authority are shown in Figures 2.4 and 2.5.

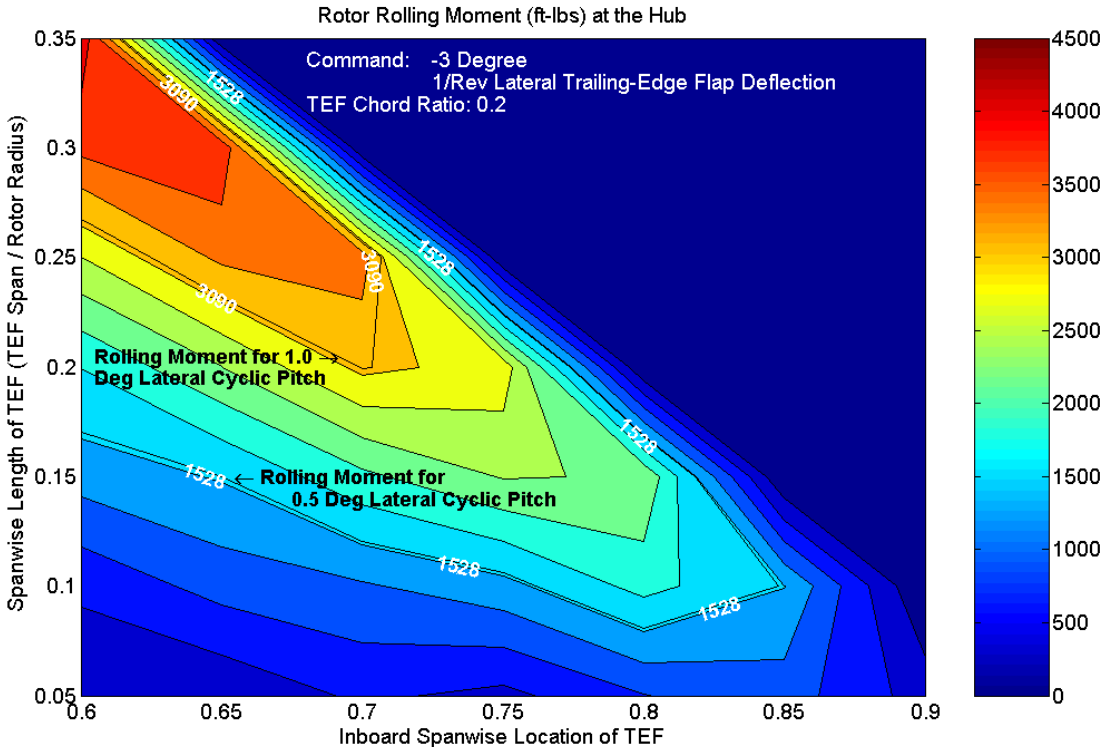

Figure 2.4. Rolling Moment Authority of Trailing Edge Flaps

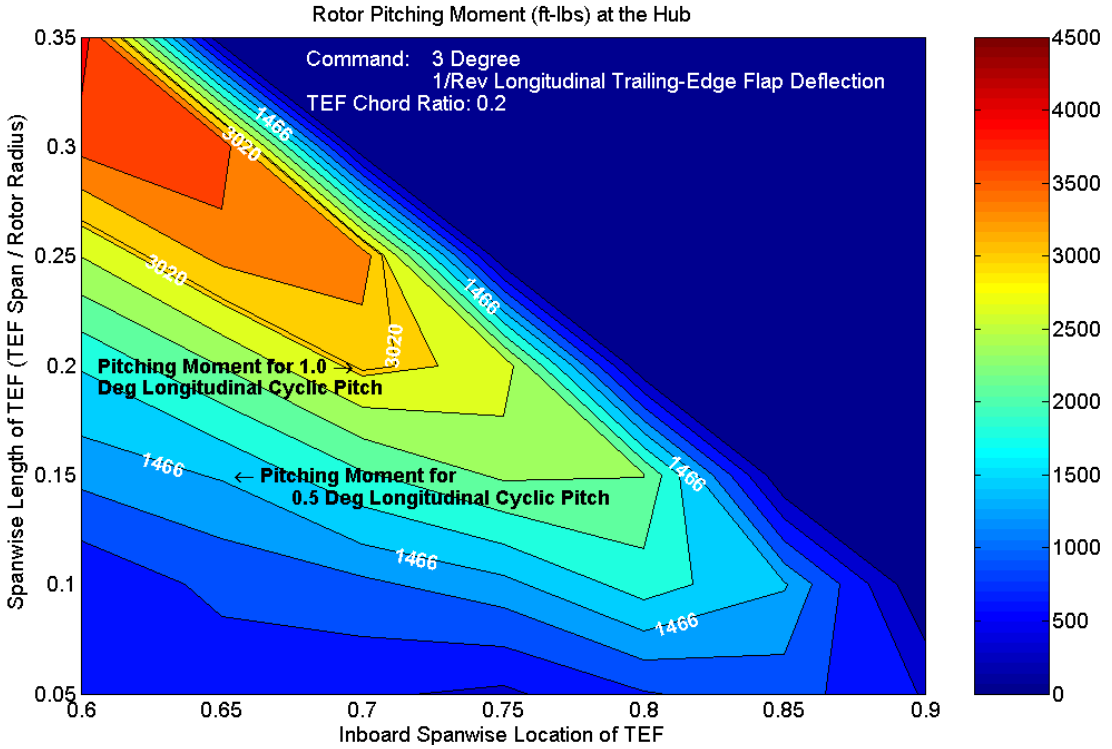

Figure 2.5. Pitching Moment Authority of Trailing Edge Flaps

Preliminary sizing of the trailing edge flap is performed based on this authority analysis. This selection is illustrated by the purple circles in the contour plot in Figure 2.6. The size of this TEF is within the range of sizes most often used in vibration control and swashplateless rotor studies (12 percent to 20 percent of the blade span, and 15 percent to 25 percent of the blade chord [14], [22], [23], [24]). The chosen chord ratio, span ratio, and span-wise location for the TEF are

$$\begin{aligned} \frac{c_f}{c} &= 0.2, \\ \frac{b_f}{b} &= 0.15, \\ \text{Location} &= 0.7R - 0.85R. \end{aligned} \tag{2.15}$$

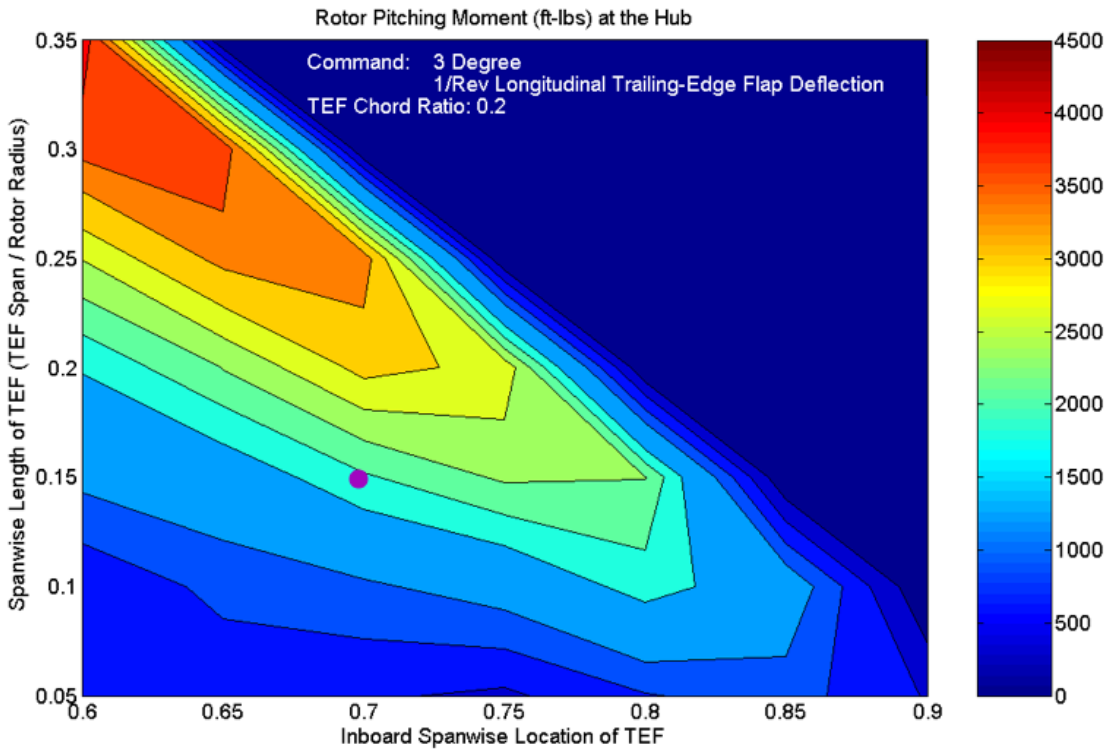

Figure 2.6. Authority of Trailing Edge Flaps with TEF Size Indicated

Chapter 3

Control Development

3.1 Overall Vehicle Control Method

The control architecture used in this analysis is comprised of two distinct controllers with separate actuators that work together to provide primary flight control and to reject the helicopter's response to the ship airwake. The primary flight control system is a standard model-following controller (MFC) architecture, modeled after the work detailed by Horn, et al. [5]. This uses the swashplate and pedals to ensure that the vehicle follows a desired response to pilot inputs, based on handling qualities specifications. Separately, the airwake compensator, which uses trailing edge flaps for control, rejects the disturbances caused by the ship airwake. In this way, command tracking – accomplished by feeding forward the pilot commands and using the MFC – is decoupled from disturbance rejection, which is performed by feeding back the angular response of the vehicle and using TEFs. This chapter outlines both components of the control system.

3.2 Model-Following Control Method

The model-following controller serves as the primary flight control system, augmenting pitch, roll, and yaw. The collective axis is left open loop for the present study. This MFC is identical to that used by Horn, et al. [5]. Prior work by Horn, et al. [4] used a modified SAS to reject disturbances while using similar levels of actuator activity as the baseline SAS. However, the closed loop response to pilot input was altered in the range of one to four radians per second – the magnitude peak in the spectral properties of airwake disturbances. Adding feed forward compensation with a model-following control method improved the closed loop response to pilot input [5]. Now feedback is only used to compensate for external disturbances from the gusts and for model inversion errors. Based on that experience, this study also uses the MFC with feed forward pilot compensation. The model-following method used in this study is detailed in this section.

3.2.1 Overall Control Architecture

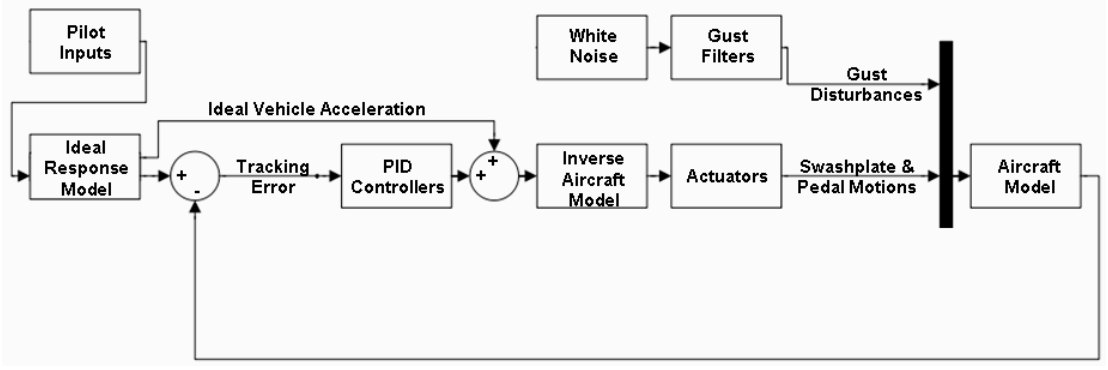

Figure 3.1. Model-Following Controller

The commands generated by the MFC are based on the angular rate tracking error, as shown in Figure 3.1. After the pilot gives a command, an ideal response model

computes the desired vehicle response in each axis. The desired responses are based on meeting Level 1 handling qualities specifications. The observed vehicle angular rates are compared to the desired values; the difference is the angular rate tracking error. PID controllers operate on the tracking error, producing additional commands in terms of vehicle response that attempt to drive the tracking error to zero. The outputs of the PID controllers are summed with the desired vehicle angular accelerations to create "pseudo-commands." The inverse model converts the pseudo-commands, which are given in terms of the desired body angular accelerations, into the stick and pedal commands that are necessary to produce them. Then, the commands are sent to the swashplate and pedals. The actuators are approximated by second order transfer functions:

$$\underline{G}_{act}(s) = \begin{bmatrix} \frac{\omega_n^2}{s^2+2\zeta\omega_n s+\omega_n^2} & 0 & 0 \\ 0 & \frac{\omega_n^2}{s^2+2\zeta\omega_n s+\omega_n^2} & 0 \\ 0 & 0 & \frac{\omega_n^2}{s^2+2\zeta\omega_n s+\omega_n^2} \end{bmatrix}. \tag{3.1}$$

The natural frequency and damping ratio are

$$\begin{aligned} \omega_{n_{act}} &= 40, \\ \zeta_{act} &= 0.8. \end{aligned} \tag{3.2}$$

During the linear control design phase, a 23-state linear model is used to represent the aircraft. It includes states for the vehicle translational and rotational motions, as well as the main rotor rigid blade flap and lag dynamics, and three states for inflow dynamics. During simulation and analysis, GENHEL is used to compute the vehicle response to the controller outputs. The individual components of the controller are discussed in this chapter.

3.2.2 Ideal Response Model and PID Control

The ideal response model, or command filter, computes the "ideal" response of the vehicle to the pilot commands, in terms of desired attitudes, attitude rates, and angular accelerations. The ideal response is based on satisfying ADS-33 requirements. The MFC controller is designed for attitude command/attitude hold (ACAH) response in the roll and pitch axes, using a second order model to meet small amplitude response requirements. Thus, a natural frequency of 2.0 and a damping ratio of 0.9 are used. The yaw axis uses a rate command response with a first order ideal response model and a time constant of 0.4 [5]. Based on these requirements, the ideal response is given by

$$\begin{bmatrix} \phi_c \\ \theta_c \\ r_c \end{bmatrix} = \begin{bmatrix} \frac{\omega_n^2}{s^2+2\zeta\omega_n s+\omega_n^2} & 0 & 0 \\ 0 & \frac{\omega_n^2}{s^2+2\zeta\omega_n s+\omega_n^2} & 0 \\ 0 & 0 & \frac{1}{\tau s+1} \end{bmatrix} \begin{bmatrix} \phi_{cmd} \\ \theta_{cmd} \\ r_{cmd} \end{bmatrix}, \tag{3.3}$$

$$\begin{bmatrix} \dot{\phi}_c \\ \dot{\theta}_c \\ \dot{r}_c \end{bmatrix} = \frac{d}{dt} \begin{bmatrix} \phi_c \\ \theta_c \\ r_c \end{bmatrix}, \tag{3.4}$$

and

$$\begin{bmatrix} \ddot{\phi}_c \\ \ddot{\theta}_c \end{bmatrix} = \frac{d^2}{dt^2} \begin{bmatrix} \phi_c \\ \theta_c \end{bmatrix}, \tag{3.5}$$

in which ϕ_c, θ_c, and r_c are the ideal roll and pitch Euler angles and the ideal yaw rate. ϕ_{cmd}, θ_{cmd}, and r_{cmd} are values based on pilot input. The first derivative of the body axis angular rates are assumed to be approximately equal to the second derivative of the roll and pitch Euler angles ($\dot{p} \approx \ddot{\phi}$ and $\dot{q} \approx \ddot{\theta}$).

After the ideal response model computes the desired vehicle response, PID controllers operate on the error between the ideal and observed vehicle responses. Proportional-derivative (PD) controllers are used in the roll and pitch axes, acting on the error in attitudes and attitude rates. The yaw axis uses a proportional-integral (PI) controller that operates on the error in yaw rate. The PID gains are chosen to give the error dynamics similar characteristics as the ideal response model. In the roll and pitch axes,

$$K_D = 2\zeta\omega_n \tag{3.6}$$

and

$$K_P = \omega_n^2, \tag{3.7}$$

where the damping ratio and natural frequency are those of the ideal response model. This choice causes the bandwidth associated with gust disturbances to be equal to the bandwidth associated with pilot commands. For the yaw axis,

$$K_P = 2\zeta\omega_n \tag{3.8}$$

and

$$K_I = \omega_n^2. \tag{3.9}$$

The output of the PID controllers is summed with the acceleration output of the ideal response model in order to create the pseudo-commands, given by the vector $\vec{\nu}$:

$$\nu_\phi = \ddot{\phi}_c + K_P(\phi_c - \phi) + K_D(\dot{\phi}_c - \dot{\phi}), \tag{3.10}$$

$$\nu_\theta = \ddot{\theta}_c + K_P(\theta_c - \theta) + K_D(\dot{\theta}_c - \dot{\theta}), \tag{3.11}$$

and

$$\nu_r = \dot{r}_c + K_P(r_c - r) + K_I \int (r_c - r)dt. \tag{3.12}$$

The reduced inverse aircraft model computes the actuator commands from the pseudo-commands:

$$\begin{bmatrix} \delta_{lat} \\ \delta_{long} \\ \delta_{ped} \end{bmatrix} = \underline{B}^{-1}_{pqr} \left(\begin{bmatrix} \nu_p \\ \nu_q \\ \nu_r \end{bmatrix} - \underline{A}_{pqr} \begin{bmatrix} p \\ q \\ r \end{bmatrix} \right). \tag{3.13}$$

It is the inverse of the simplified 3-state aircraft model:

$$\begin{bmatrix} \dot{p} \\ \dot{q} \\ \dot{r} \end{bmatrix} = \underline{A}_{pqr} \begin{bmatrix} p \\ q \\ r \end{bmatrix} + \underline{B}_{pqr} \begin{bmatrix} \delta_{lat} \\ \delta_{long} \\ \delta_{ped} \end{bmatrix}. \tag{3.14}$$

Details for the roll axis controller are shown in Figure 3.2.

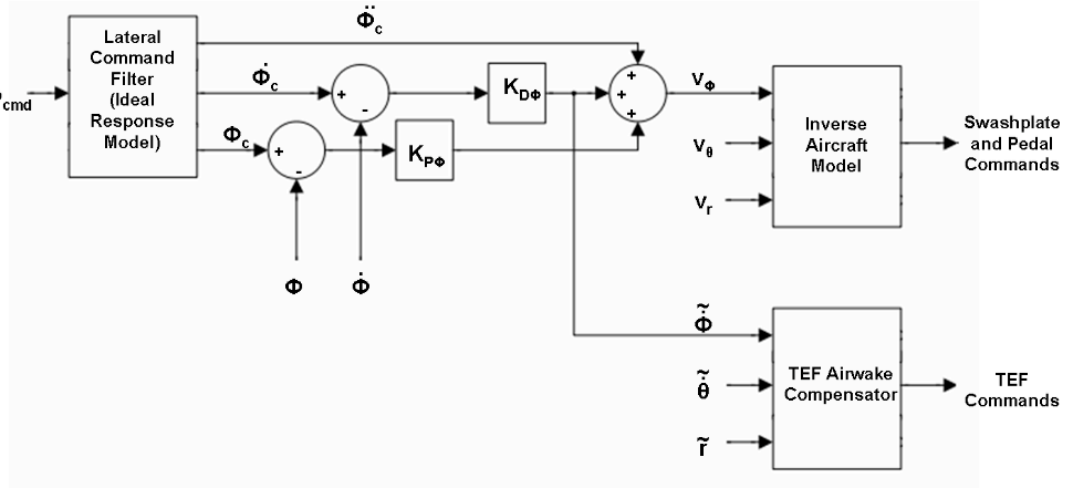

Figure 3.2. Model-Following Controller with Trailing Edge Flaps (Roll Axis)

3.2.3 Linear Models

Linear models are used in multiple instances within this study in order to allow the use of linear control methods. They are derived from the nonlinear GENHEL simulation using a numerical perturbation method, which is detailed in Appendix B. The linear model represents the trim state open-loop dynamics for the WOD speed being considered. The extracted model has 28 states including vehicle, rotor, inflow, and engine dynamics. During the control design, a 23-state linear model is used to compute the vehicle response to control inputs. Engine dynamics are excluded since RPM is assumed to be constant. That model is reduced and inverted to a 3-state model (vehicle angular rates) for use within the model-following controller for conversion from pseudo-commands to actual control inputs. The MFC compensates for errors associated with using a simplified inversion model. Additionally, an 8-state linear model, consisting of vehicle translational rates, angular rates, and roll and pitch attitudes, is used in the creation of the gust filters. The linear models are used during the control design and initial analysis phase. All

conclusions of this study are based on simulations conducted in the nonlinear GENHEL flight dynamics environment.

3.2.4 Translational Rate Command Controller

As in a previous study [5], an outer loop is added to the model-following controller in order to allow the vehicle to hold station without pilot input. This provides translational rate command (TRC) control over the vehicle by relating pilot inputs to speed commands, which are then related to commanded vehicle attitudes via a PI controller. Details of the TRC controller used in this research can be found in Reference [5]. This portion of the control is used solely to hold the vehicle stationary during simulation; its commands are in a lower frequency range than both the MFC and the TEF controller. Consequently, they have minimal impact on the conclusions that can be drawn based on the MFC and TEF controller.

3.3 Airwake Compensator

The portion of the controller that rejects the ship airwake disturbances uses trailing edge flaps and is detailed in this section. The architecture is the same as that of the swashplate-based airwake compensator developed by Horn, et al. [5]. The airwake compensator (AWC) operates as an additional feedback loop in the system, as shown in Figure 3.3, and can be engaged or disengaged as desired. Additionally, different TEF controllers could be interchanged within one existing MFC. Because it operates on the angular rate tracking error, the TEF controller has no effect if the pilot inputs are already being tracked. This is advantageous since it eliminates interference between the pilot commands and the TEF commands. For instance, even if the pilot input is at the same frequency as the ship airwake, which the

TEFs are trying to reject, the TEFs will not reject the input if the desired vehicle response is seen. Thus, if there is no disturbance to the system, the trailing edge flaps will not move.

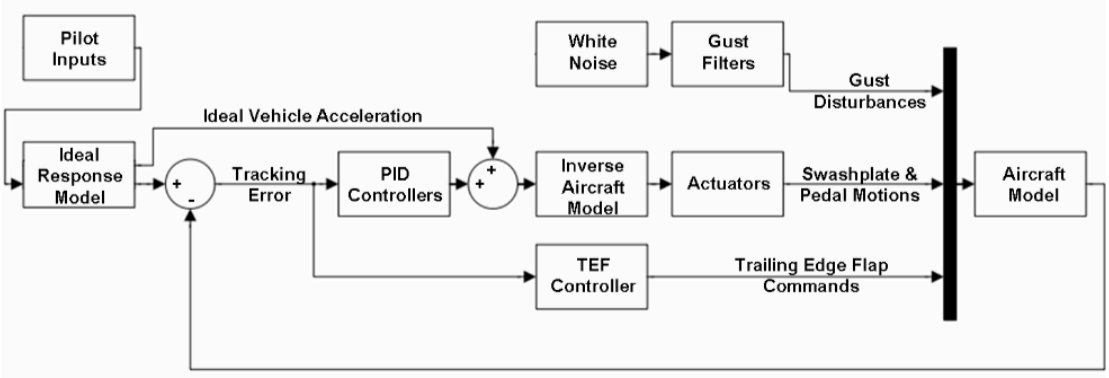

Figure 3.3. Model-Following Controller with Trailing Edge Flap Airwake Compensator

3.3.1 Overall Airwake Compensator Design Method

The TEF controller is designed as an additional feedback loop around the closed-loop system that consists of the model-following controller and the aircraft. An augmented plant model represents the closed-loop system, as shown in Figure 3.4. The augmented model includes the model-following controller and includes the outputs of the TEF controller as system inputs, while the inputs of the TEF controller contribute to the outputs of the augmented plant model. The inputs to the plant model include four TEF commands produced by the AWC, six gust disturbance inputs, and three sensor noise inputs. The sensor noise inputs,

$$\underset{\sim}{W}_{noise}(s) = 0.5 \begin{bmatrix} \frac{\pi}{180} & 0 & 0 \\ 0 & \frac{\pi}{180} & 0 \\ 0 & 0 & \frac{\pi}{180} \end{bmatrix}, \tag{3.15}$$

are not included in the TEF controller design separately; they are used to con-

tribute to the vehicle angular rate feedback. Outputs of the augmented plant model include four TEF actuator weighting functions, three performance weights on the vehicle angular rates, and three AWC inputs that are the angular rate errors with noise estimates.

Correspondingly, the following are inputs to the airwake compensator itself: three vehicle angular rate errors including noise estimates, three performance weighting functions, and four TEF actuator weighting functions. The effects of the values used for the performance and actuator weighting functions will be presented in Chapter 4. The outputs of the airwake compensator consist of the four trailing edge flap commands in the fixed frame. The augmented plant model is linearized within Simulink and used in the linear control design of the TEF controller.

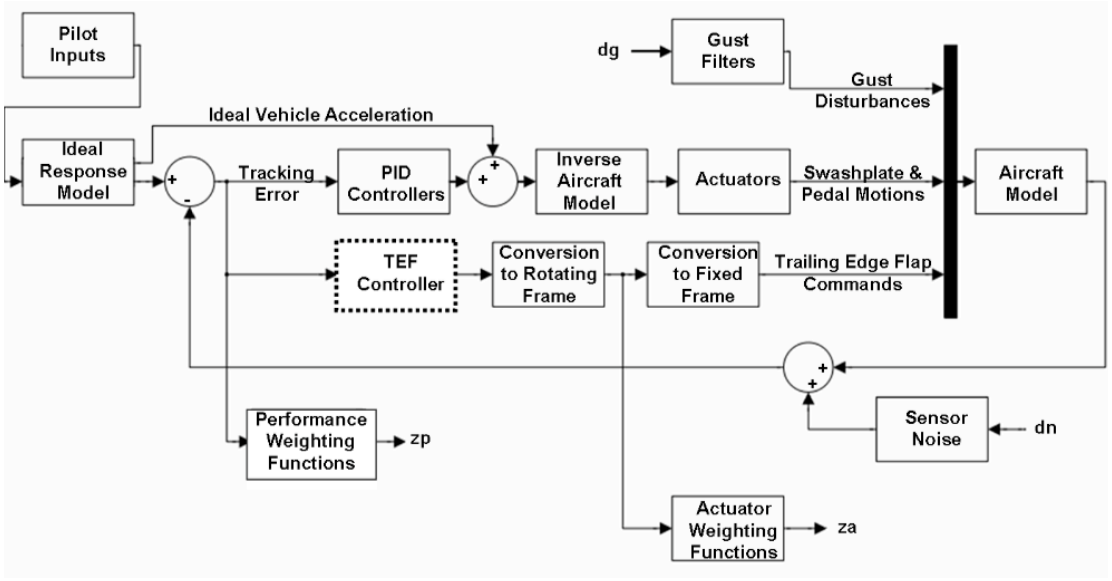

Figure 3.4. Augmented Plant Model Used for Control Design

3.3.2 Gust Filters

A gust disturbance model that replicates the airwake spectral properties is incorporated in the control synthesis of the TEF controller. This allows the controller to be tuned specifically for rejection of airwake-induced disturbances. A method for determining equivalent airwake disturbance models from simulation was developed by Horn, et al. [36]. First, simulations are run in GENHEL with the ship airwake while a specified station is held using a pilot model. The details of the pilot model can be found in Reference [15]. The vehicle response output of the simulations and a reduced 8-state linear model with the trim states removed are used. A gust vector,

$$\vec{w} = \underline{G}^{+}\left(\dot{\vec{x}} - \underline{A}\vec{x} - \underline{B}\vec{u}\right), \tag{3.16}$$

is computed, in which $\underline{G}^{+}$ is the pseudo-inverse of $\underline{G}$. The gust vector has six components: three for average gust velocity in three directions, and three for the angular rate components of the gust field. The mean disturbance is removed, since that is caused by the constant wind. This leaves the equivalent perturbations in vehicle response caused by the stochastic component of the gust [4]. A power spectral density (PSD) of the equivalent gust disturbances is calculated using the Welch method and Hamming windowing.

The gust filters are transfer functions that are fit to the PSD of the vehicle response. The filters are fit to the equivalent disturbance data using least squares curve fitting methods [4]. When driven by zero mean unity white noise, the filters generate a disturbance time history similar to the vehicle disturbances caused by the airwake in terms of its power spectral density.

Gust filters can be created for each WOD condition and landing spot. An

example of a gust filter created for the roll axis in a 30-degree, 30-knot WOD condition is shown in Figure 3.5. These filters are used to model the disturbances during the control synthesis. Simulation testing uses the CFD data, as opposed to the filters.

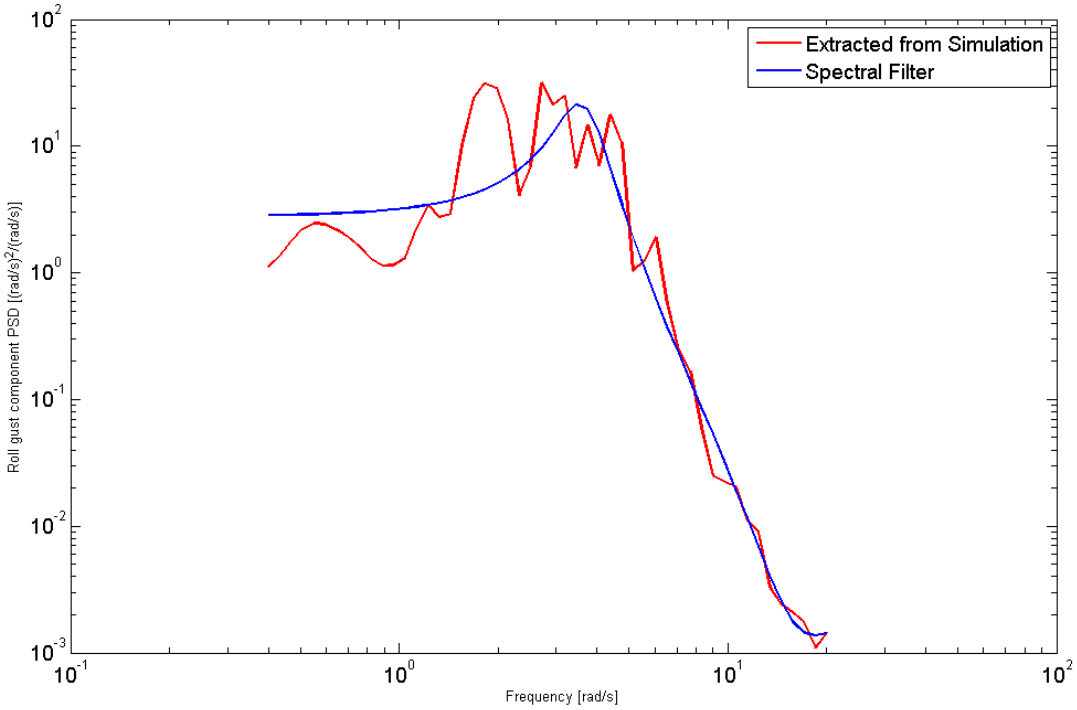

Figure 3.5. PSD of Roll Airwake Disturbances

3.4 Trailing Edge Flap Controller Development

3.4.1 Trailing Edge Flap Limitations

The potential of the TEFs is affected by assumptions and modeling choices. In this thesis, the TEFs are restricted to moving according to fixed-frame commands – δ_0, δ_{1C}, δ_{1S}, and δ_2. Those commands are converted to individual blade commands, with

$$\delta_f^k = \delta_0 + \delta_{1C}\cos(\psi_k) + \delta_{1S}\sin(\psi_k) + \delta_2(-1)^k, \tag{3.17}$$

where k is the blade number, and ψ_k is the azimuth location of the k^{th} blade. Commands in the fixed frame are similar to those that are possible via the swashplate:

$$\theta = \theta_0 + \theta_{1C}\cos(\psi_k) + \theta_{1S}\sin(\psi_k). \tag{3.18}$$

Another modeling choice that affects the perceived performance of the TEFs is the lack of a TEF actuator model. This model assumes that the TEFs are capable of moving instantaneously to the commanded deflection. Limits on the possible TEF deflection magnitude are included.

Because the trailing edge flap deflections and rates are limited by current actuator technology, it is necessary to incorporate those limits within the control design. In GENHEL, the TEF deflection is limited to a specified maximum deflection (in this case, five degrees) immediately before the command is sent to each blade. Thus, the saturation occurs in the rotating frame. The controller, however, outputs fixed frame commands. It is important to saturate the TEF deflection in the rotating frame because saturating in the fixed frame could result in the magnitude of all four TEFs being reduced even if only one is beyond actuation limits. In the Simulink model, the desired TEF deflections are computed in the fixed frame. These are then used to compute the individual TEF deflections, according to

$$\vec{\delta}_f^{\,k} = \underline{R}(\psi_k)\vec{\delta}_f^{\,FF},$$

$$\begin{bmatrix} \delta_f^1 \\ \delta_f^2 \\ \delta_f^3 \\ \delta_f^4 \end{bmatrix} = \underline{R}(\psi_k) \begin{bmatrix} \delta_0 \\ \delta_{1C} \\ \delta_{1S} \\ \delta_2 \end{bmatrix}, \tag{3.19}$$

in which

$$\underline{R}(\psi_k) = \begin{bmatrix} 1 & \cos(\psi_1) & \sin(\psi_1) & -1 \\ 1 & \cos(\psi_2) & \sin(\psi_2) & 1 \\ 1 & \cos(\psi_3) & \sin(\psi_3) & -1 \\ 1 & \cos(\psi_4) & \sin(\psi_4) & 1 \end{bmatrix}. \tag{3.20}$$

The individual deflections are saturated as necessary, and the saturated fixed frame commands are

$$\vec{\delta}_f^{\,FF} = \underline{R}^{-1}(\psi_k)\vec{\delta}_f^{\,k}. \tag{3.21}$$

By placing limits on the individual TEF deflections rather than the fixed frame commands, each flap is able to deflect to the maximum before saturation.

3.4.2 H_2 Control Synthesis

Once the augmented plant model is linearized, it is used in a robust control design of the trailing edge flap controller. A robust control method is chosen because of the uncertainties in the gust disturbances as well as errors in the linear models. For this study, an H_2 control synthesis based on the method of Haddad and Bernstein [37] is performed. This method is outlined here.

The goal of the H_2 synthesis is to minimize the H_2 norm of the transfer function

from the disturbances to the performance variables,

$$\|T_{z\omega}(s)\|_2 = \sqrt{\frac{1}{2\pi}\int_{-\infty}^{\infty} tr\left\{T_{z\omega}^*(j\omega)T_{z\omega}(j\omega)\right\}d\omega}, \tag{3.22}$$

while stabilizing the open loop system with a real, rational controller $\underline{K}(s)$.

In H_2 analysis, γ approaches infinity. The other matrices in the algebraic Riccati equations are

$$\underline{A}_Q^T\underline{Q} + \underline{Q}\underline{A}_Q - \underline{Q}\underline{R}_Q\underline{Q} + \underline{Q}_Q = 0, \tag{3.23}$$

$$\underline{A}_P^T\underline{P} + \underline{P}\underline{A}_P - \underline{P}\underline{R}_P\underline{P} + \underline{Q}_P = 0, \tag{3.24}$$

$$\underline{A}_Q = \left(\underline{A} - \underline{B}_1\underline{D}_{21}^T\left[\underline{D}_{21}\underline{D}_{21}^T\right]^{-1}\underline{C}_2\right)^T, \tag{3.25}$$

$$\underline{Q}_Q = \underline{B}_1\underline{B}_1^T - \underline{B}_1\underline{D}_{21}^T\left[\underline{D}_{21}\underline{D}_{21}^T\right]^{-1}\underline{D}_{21}\underline{B}_1^T, \tag{3.26}$$

$$\underline{R}_Q = \underline{C}_2^T\left[\underline{D}_{21}\underline{D}_{21}^T\right]^{-1}\underline{C}_2 - \gamma^{-2}\underline{C}_1^T\underline{C}_1, \tag{3.27}$$

$$\underline{A}_P = \underline{A} - \underline{B}_2\left[\underline{D}_{12}^T\underline{D}_{12}\right]^{-1}\underline{D}_{12}^T\underline{C}_1, \tag{3.28}$$

$$\underline{Q}_P = \underline{C}_1^T\underline{C}_1 - \underline{C}_1^T\underline{D}_{12}\left[\underline{D}_{12}^T\underline{D}_{12}\right]^{-1}\underline{D}_{12}^T\underline{C}_1, \tag{3.29}$$

$$\underline{R}_P = \underline{B}_2\left[\underline{D}_{12}^T\underline{D}_{12}\right]^{-1}\underline{B}_2^T - \gamma^{-2}\underline{B}_1\underline{B}_1^T. \tag{3.30}$$

The state-space form of the controller is given by

$$\underline{K}(s) = \begin{bmatrix} \underline{A}_K & \underline{B}_K \\ \underline{C}_K & \underline{D}_K \end{bmatrix} \tag{3.31}$$

with

$$\underline{A}_K = \underline{A} + \underline{B}_2\underline{C}_K - \underline{B}_K\underline{C}_2 + \gamma^{-2}\underline{Q}\left(\underline{C}_1^T\underline{C}_1 + \underline{C}_1^T\underline{D}_{12}\underline{C}_K\right), \tag{3.32}$$

$$\underline{B}_K = \left(\underline{Q}\underline{C}_2^T + \underline{B}_1\underline{D}_{21}^T\right)\left[\underline{D}_{21}\underline{D}_{21}^T\right]^{-1}, \tag{3.33}$$

$$\underline{C}_K = -\left[\underline{D}_{12}^T\underline{D}_{12}\right]^{-1}\left(\underline{B}_2^T\underline{P} + \underline{D}_{12}^T\underline{C}_1\right)\left[\underline{I} - \gamma^{-2}\underline{Q}\underline{P}\right]^{-1}, \tag{3.34}$$

$$\underline{D}_K = \underline{0}. \tag{3.35}$$

For the control synthesis, the augmented plant model is reorganized according to

$$\dot{\vec{x}} = \underline{A}\vec{x} + \underline{B}\begin{bmatrix} \vec{u} & \vec{w} \end{bmatrix} \tag{3.36}$$

and

$$\begin{Bmatrix} \dot{\vec{x}} \\ \vec{z} \\ \vec{y} \end{Bmatrix} = \begin{bmatrix} \underline{A} & \underline{B}_2 & \underline{B}_1 \\ \underline{C}_1 & \underline{D}_{12} & \underline{D}_{11} \\ \underline{C}_2 & \underline{D}_{22} & \underline{D}_{21} \end{bmatrix} \begin{Bmatrix} \vec{x} \\ \vec{u} \\ \vec{w} \end{Bmatrix}. \tag{3.37}$$

Here, the gust terms are incorporated within the $\underline{B}$ matrix. The vector $\vec{z}$ includes the performance variables, while $\vec{y}$ includes the output variables.

The H_2 controller is designed based on the linearized augmented plant model

within Matlab. After finding the minimal realization of the system, the resulting matrix $\underline{K}(s)$ is a 52 by 52 matrix (corresponding to 52 states) that is output to a file and read into GENHEL during simulation.

Chapter 4

Results

The model-following controller with trailing edge flap airwake compensation is implemented in GENHEL with the ship airwake. Results of varying parameters within the control design are presented in this chapter, along with results of varying the TEF size and location. Additionally, a few WOD conditions are considered. Finally, comparisons with a similar swashplate-based airwake compensator are shown.

4.1 Description of Simulated Flight Conditions

All of the results presented here are for a UH-60A Black Hawk helicopter hovering 17 feet above landing spot 8 of an LHA-class ship. The landing spots can be seen in Figure 4.1. For each WOD condition, the same airwake data is used for every simulation for consistency. The WOD condition is dependent on the wind speed and azimuth angle from the bow of the ship. The variation in the severity of wind conditions – as produced by the CFD data developed by Long, et al. – can be seen in Figure 4.2, which shows a vorticity magnitude isosurface for the 0-degree and 30-degree WOD conditions with a 30-knot wind [18]. No pilot stick input is

used; the translational rate controller and the model-following controller hold the vehicle stationary.

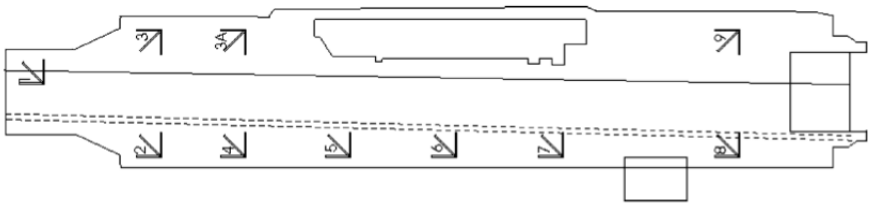

Figure 4.1. Top View of LHA Class Ship [18]

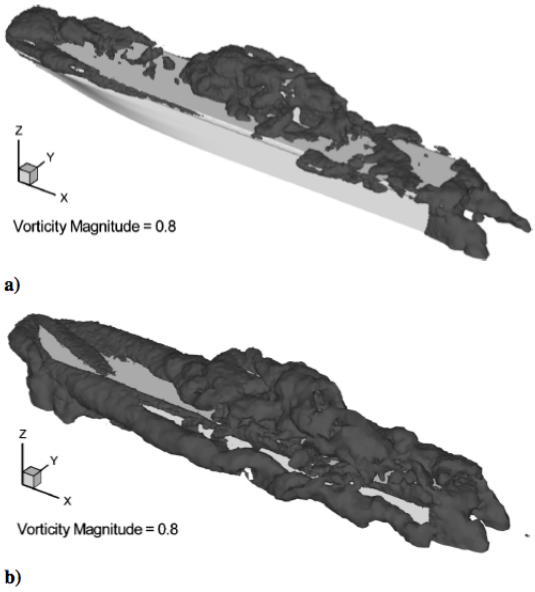

Figure 4.2. Vorticity Magnitude Isosurface for a) 0-deg and b) 30-deg WOD Cases [18]

4.2 Analysis of Trailing Edge Flap Control

4.2.1 General Analysis of Results

For each simulated case, several plots are shown. The first two presented – examples of which are illustrated in Figures 4.3 and 4.4 – show the vehicle angular rates

and attitudes. Note that trailing edge flaps have no direct control over vehicle yaw motion. Ordinarily, the tail rotor provides this control. Changes in yaw behavior of the vehicle are caused by coupling between axes rather than direct TEF control. If desired, tail rotor control could easily be incorporated within the airwake compensator. This study is focused on TEF control only.

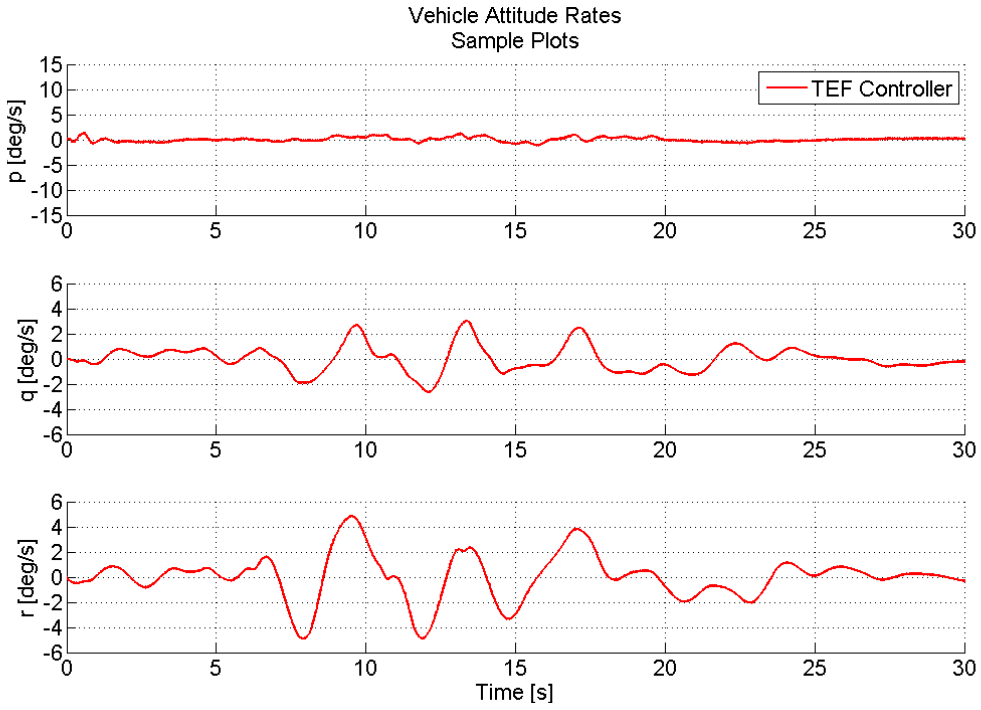

Figure 4.3. Vehicle Attitude Rates: Sample Case

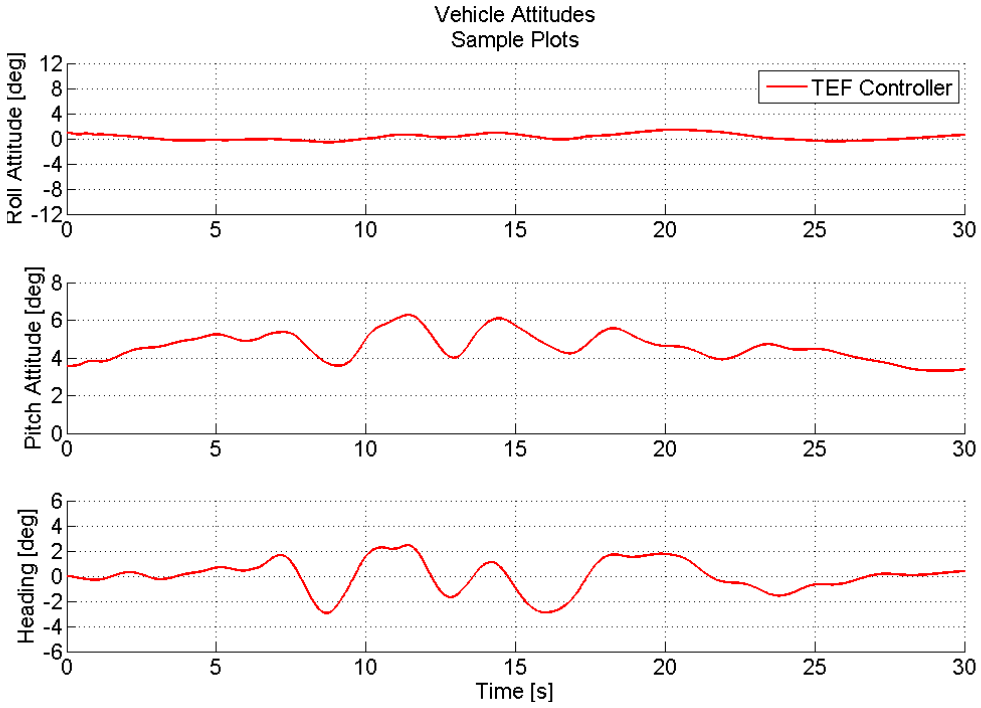

Figure 4.4. Vehicle Attitudes: Sample Case

The rest of the plots presented for each case relate to the trailing edge flaps. The first shows a time history of flap deflection on a single blade (the blade that starts at zero degrees azimuth angle at the start of the simulation). An example of this plot is shown in Figure 4.5. On this figure, the enforced saturation limits of the TEFs are shown at a magnitude of five degrees. The TEFs are not permitted to exceed this deflection at any time during simulation. Assuming that TEF actuators can produce five degrees deflection is optimistic. Thus, a line indicating three degrees deflection is also included. The majority of TEF deflections remain below three degrees.

As can be seen in Figure 4.5, the TEFs do not move harmonically. Their motion is time-varying depending on the current motion of the vehicle, as expected. In order to examine how all four TEFs deflect, a shorter time history is shown in

Figure 4.6. Each flap moves according to the fixed-frame commands, restricting their phases relative to another. Because the motion of the four TEFs are prescribed and consistently behave similar to Figure 4.6, the presented results only include one blade for clarity.

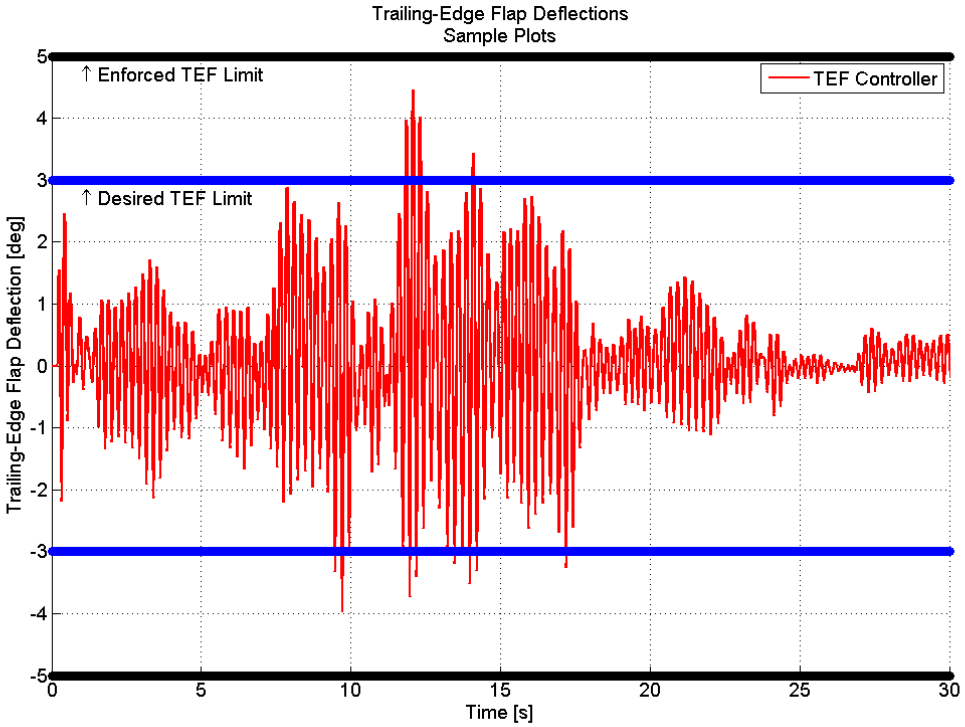

Figure 4.5. TEF Deflections: Sample Case

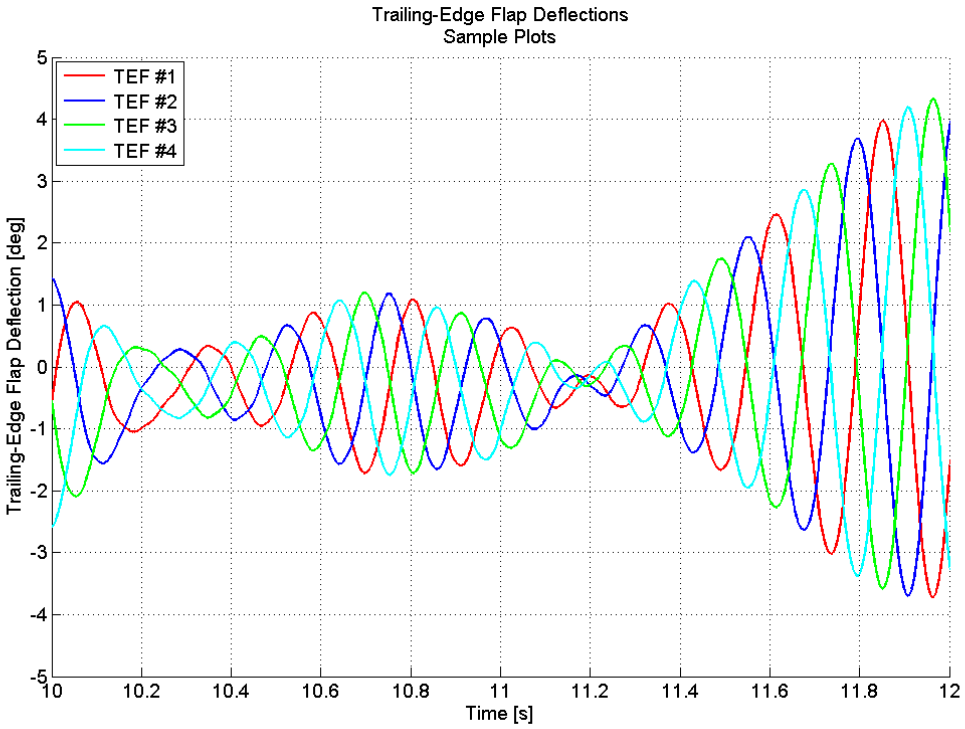

Figure 4.6. TEF Deflections For All Four Blades: Sample Case

When considering TEF deflections, it is also pertinent to examine the desired deflection rates and frequencies. The TEFs remain sufficiently below current actuator capabilities. For example, if TEFs can deflect to magnitudes of plus and minus three degrees (for a total deflection of six degrees) at rates of up to 30 Hertz, then their equivalent maximum deflection rate is 180 degrees per second. This limit is indicated in the example Figure 4.7. Additionally, the power spectral density (PSD) of the TEF deflection is shown in Figure 4.8. Because this application is for vehicle handling qualities augmentation, the dominating frequencies of TEF deflection are less than once per revolution, or approximately 4.3 Hertz for the Black Hawk. Thus, the frequency and deflection rates are within current actuator technology. Based on the commanded TEF motion amplitude, frequency, and rate, the limiting factor for remaining within actuator capabilities is the magnitude of

trailing edge flap deflection.

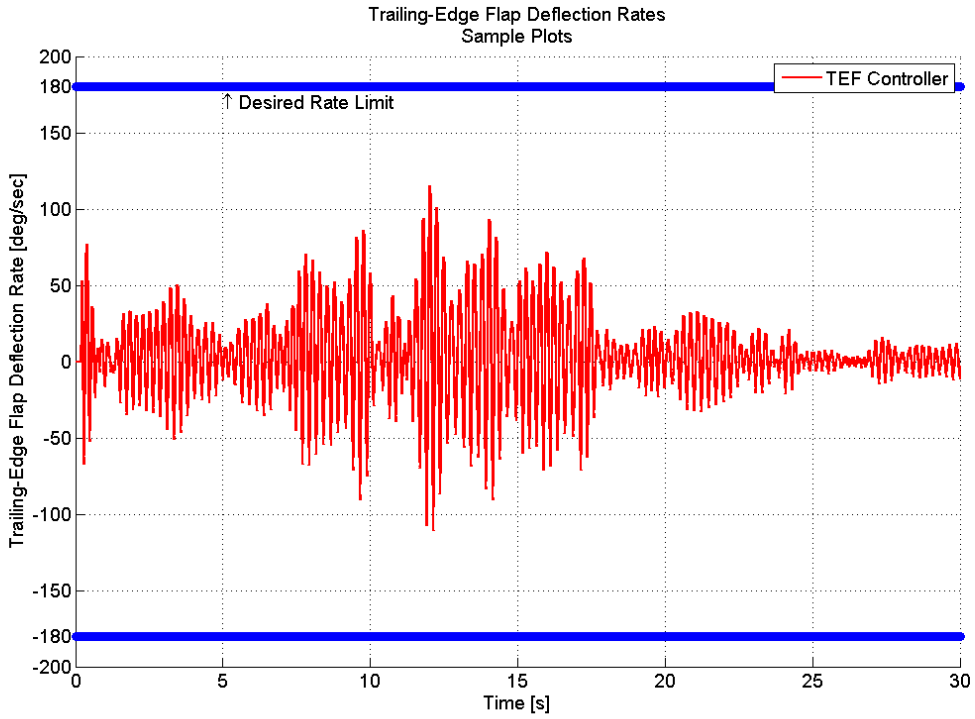

Figure 4.7. TEF Deflection Rates: Sample Case

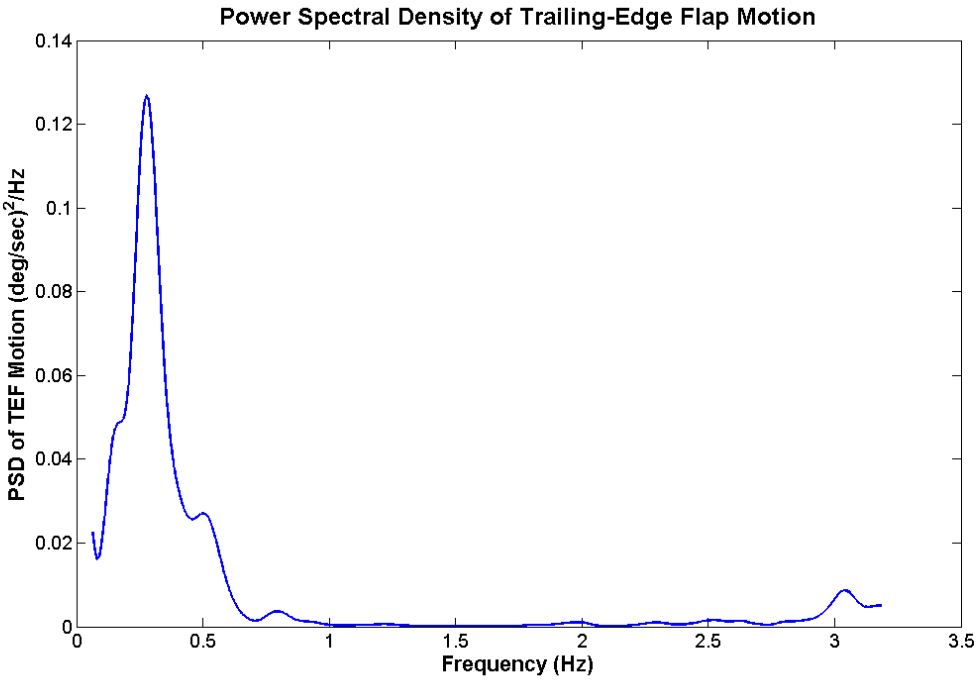

Figure 4.8. PSD of TEF Deflections: Sample Case

4.2.2 Effect of Actuator Weighting Choices

Within the TEF control design, actuator weighting variables are included in order to give preference to certain frequency ranges of actuator activity. The actuator weighting function is

$$\underline{W}_{act} = \begin{bmatrix} \frac{s-z}{s-p} & 0 & 0 & 0 \\ 0 & \frac{s-z}{s-p} & 0 & 0 \\ 0 & 0 & \frac{s-z}{s-p} & 0 \\ 0 & 0 & 0 & \frac{s-z}{s-p} \end{bmatrix}. \tag{4.1}$$

The values chosen for the zero (z) and the pole (p) locations, given in radians per second, determine the frequency behavior of the actuators. High frequency TEF activity is penalized over low frequency activity. The effects of the pole location in

the weighting functions are analyzed. The zero location is held constant throughout the analysis.

With an actuator weighting function of

$$\underline{W}_{act} = \begin{bmatrix} \frac{s+2}{s+10} & 0 & 0 & 0 \\ 0 & \frac{s+2}{s+10} & 0 & 0 \\ 0 & 0 & \frac{s+2}{s+10} & 0 \\ 0 & 0 & 0 & \frac{s+2}{s+10} \end{bmatrix}, \tag{4.2}$$

10 radians per second is the desired upper frequency limit – the limit above which the TEF motion is most penalized. This upper value (the pole location of the transfer function) is varied over a series of simulations for the 30-degree / 30-knot WOD condition. TEFs are capable of moving up to 30 Hertz (188.5 radians per second). However, the upper frequency limit is varied for a number of simulations in order to examine its effect. Results for simulations using controllers designed with upper frequency limits of between 5 and 30 radians per second are shown in Figure 4.9 – 4.12. In this series of simulations, the TEF spans from 70 percent to 90 percent of the blade span and has a chord ratio of 0.2. The results indicate that giving a preference to lower TEF frequencies in the control synthesis results in smaller TEF deflections and smoother vehicle response. For this reason, an upper frequency variable of 10 radians per second is used in the final control design.

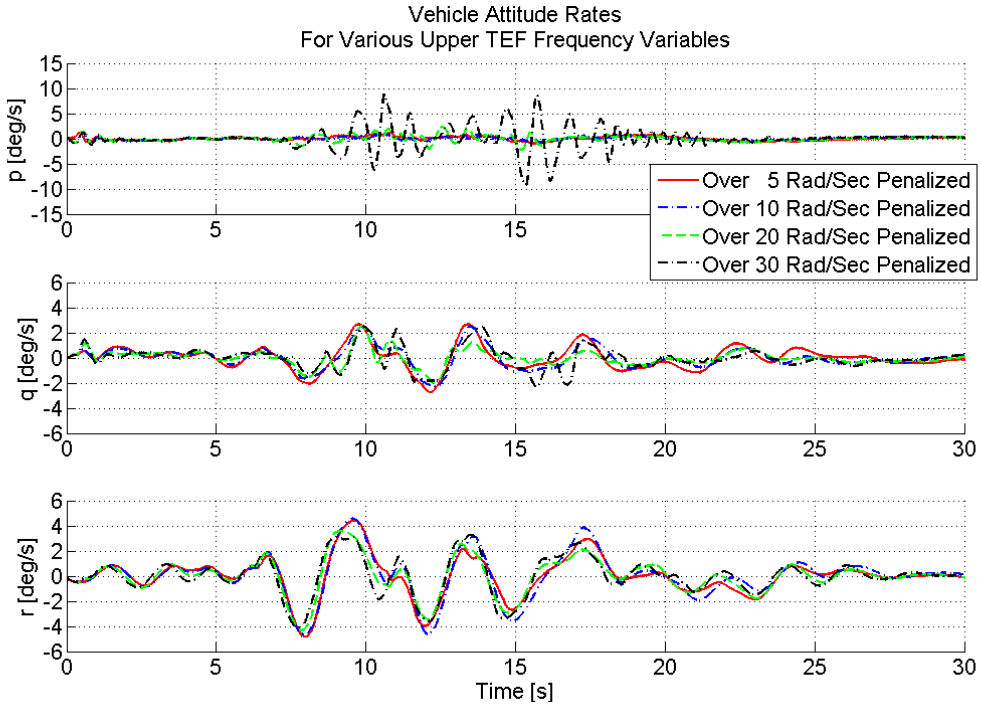

Figure 4.9. Vehicle Attitude Rates: Varying Desired Upper TEF Frequency

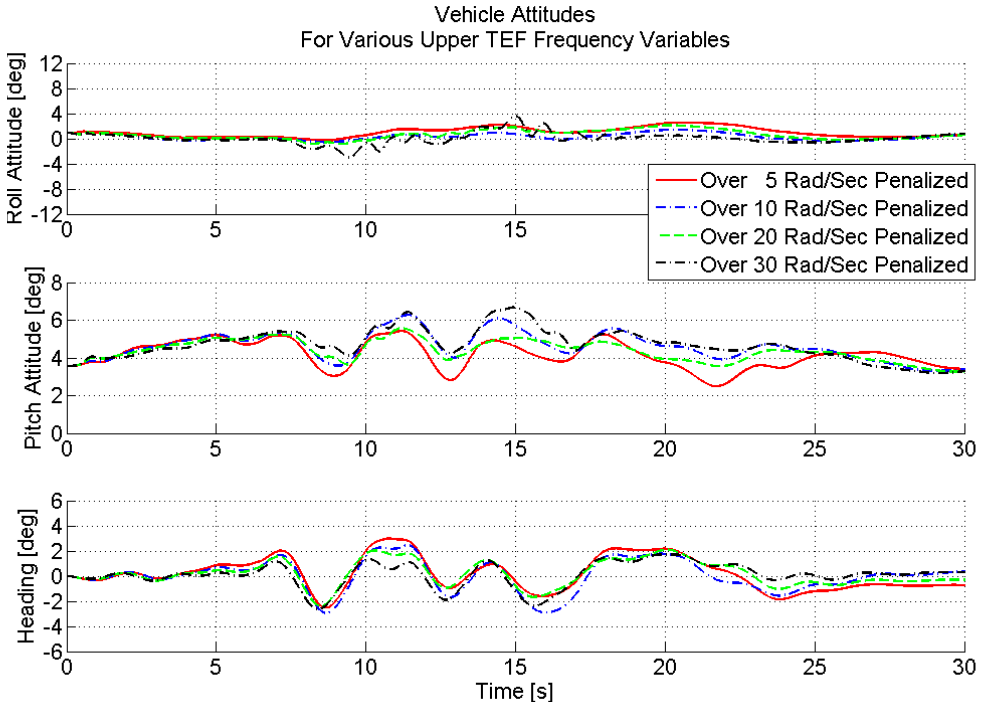

Figure 4.10. Vehicle Attitudes: Varying Desired Upper TEF Frequency

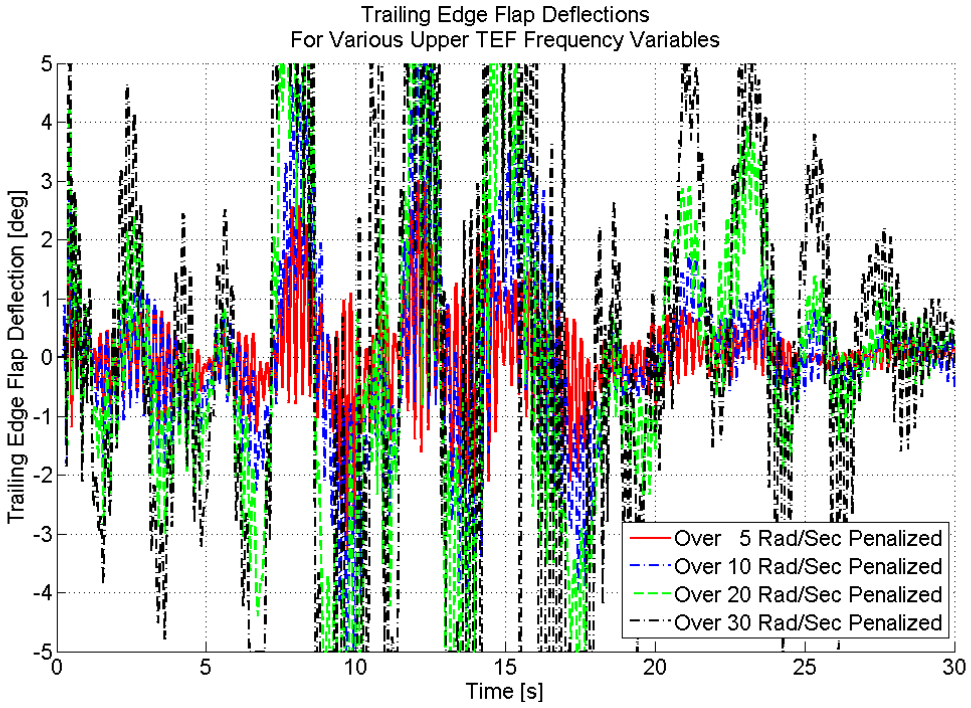

Figure 4.11. TEF Deflections: Varying Desired Upper TEF Frequency

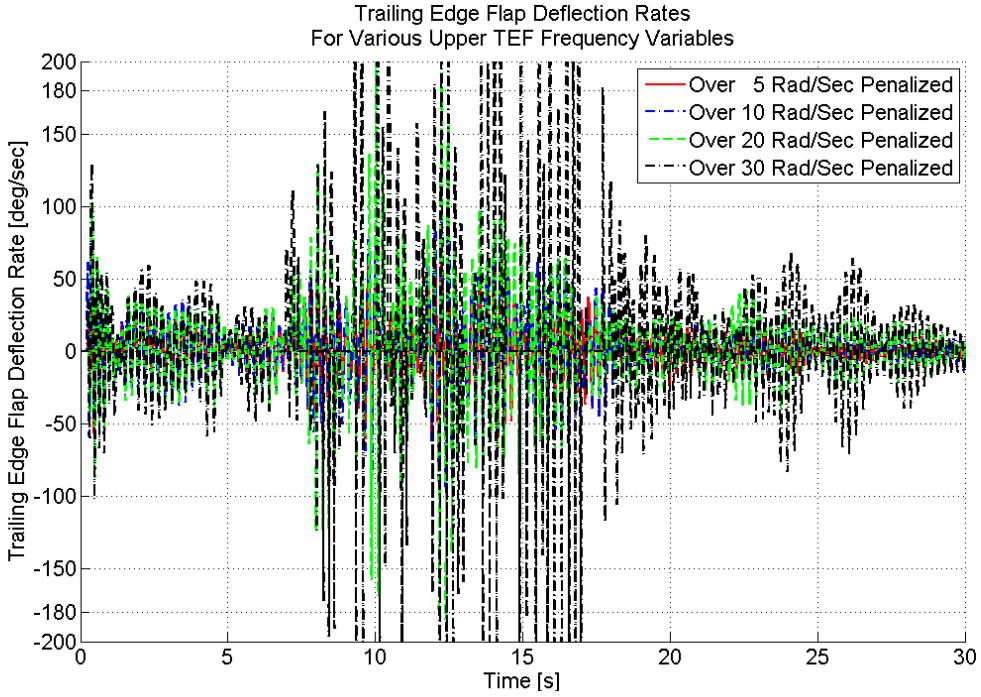

Figure 4.12. TEF Deflection Rates: Varying Desired Upper TEF Frequency

4.2.3 Effect of Performance Weighting Choices

The control synthesis also includes performance weighting functions for each output variable (p, q, and r), with the vehicle angular rates measured in degrees per second. Because the performance of the airwake compensator is based on disturbance rejection, the performance variables are not frequency-dependent. The chosen base performance weighting matrix is the identity matrix, based on previous research [5]. This puts an equal weight on the angular rate response in degrees per second in all three axes. Results with the identity matrix are presented in Figures 4.13 – 4.16. In this series of simulations, the TEF spans from 70 percent to 90 percent of the blade span and has a chord ratio of 0.2.

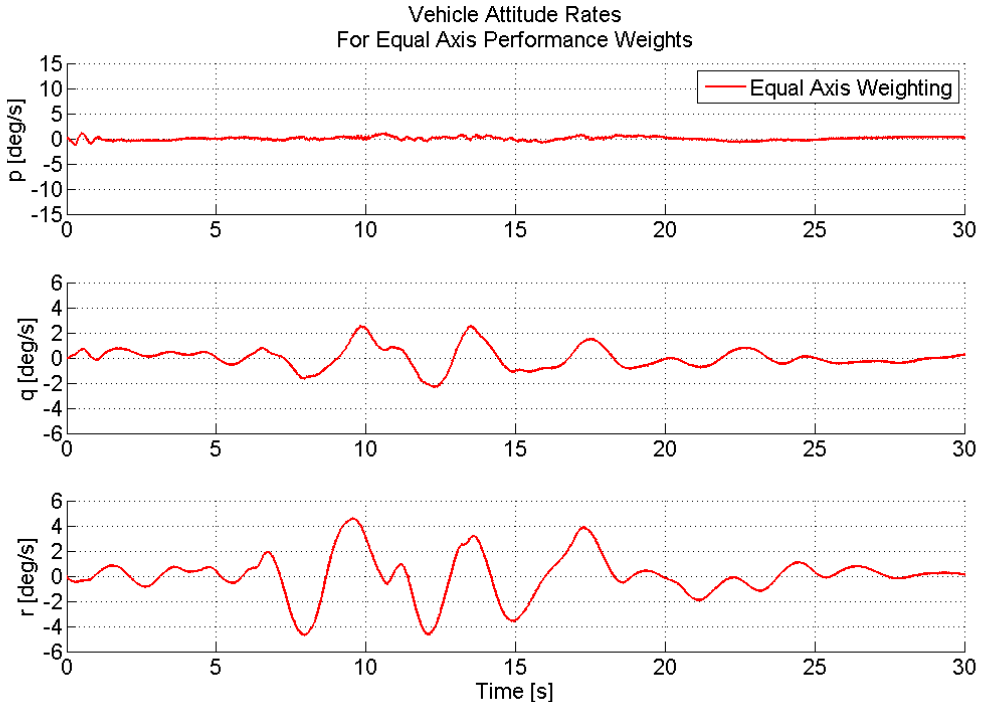

Figure 4.13. Vehicle Attitude Rates: Equal Axes Performance Weights

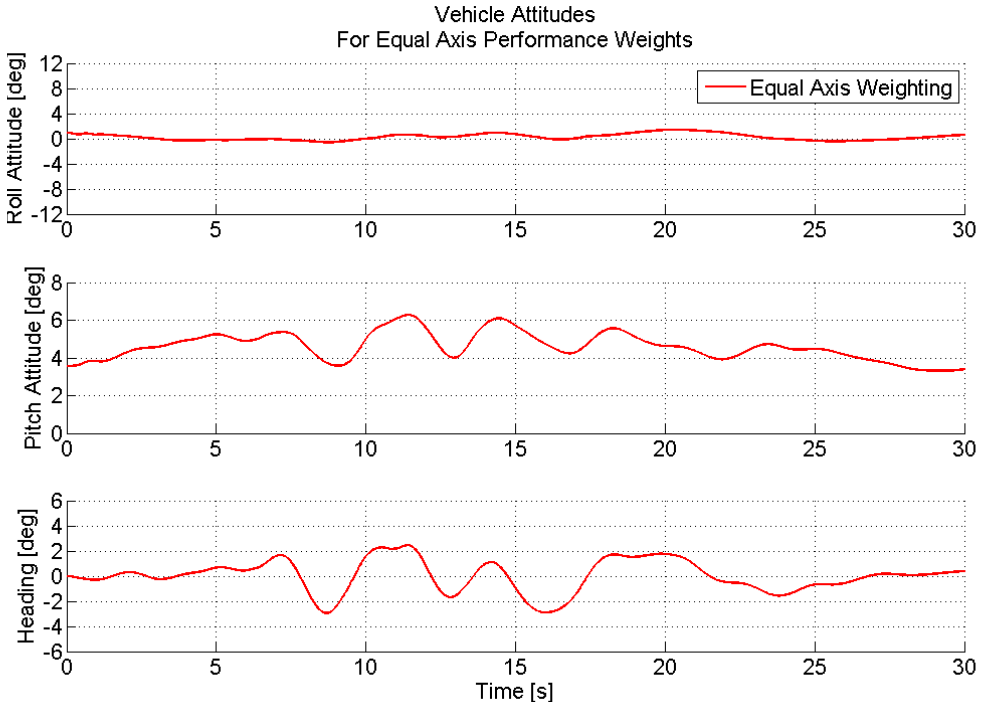

Figure 4.14. Vehicle Attitudes: Equal Axes Performance Weights

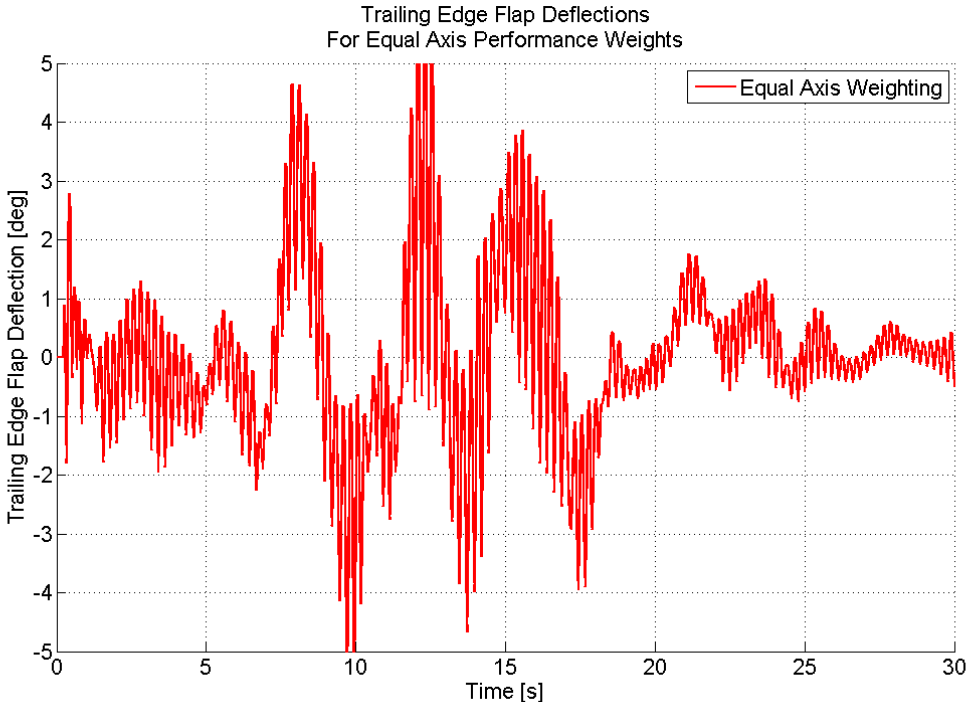

Figure 4.15. TEF Deflections: Equal Axes Performance Weights

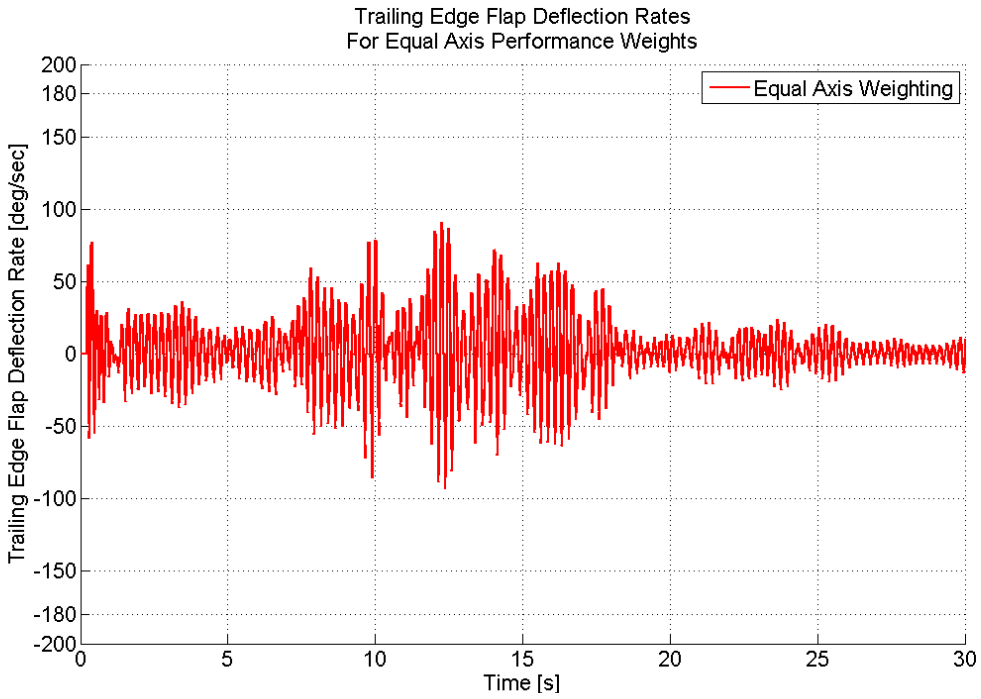

Figure 4.16. TEF Deflection Rates: Equal Axes Performance Weights

However, especially with using trailing edge flaps for disturbance rejection and no tail rotor, potential improvements could be found by adjusting the weights in each axis according to how much authority the TEFs have over degrees of freedom in that axis. For example, the roll inertia on a conventional helicopter is much lower than the pitch inertia. Thus, TEFs can more easily affect roll motion than pitch motion. Additionally, the TEFs have no direct authority over yaw motion. Rather, any changes in yaw motion are due to coupling effects between the axes. Consequently, it can be presumed that decreasing the performance weighting function in the yaw axis would have minimal effect on the vehicle response.

To explore the effects of changing the performance weighting variables in each axis, a series of simulations are performed. In one set of simulations, the pitch axis weight is decreased while both the roll and yaw axis weights remain equal to one. The results of this study are presented in C.1 – C.4 of Appendix C. Reducing

the pitch axis performance weight to 75 percent that of the roll axis reduces TEF deflections slightly while maintaining performance. The overall effect is small until the weight is reduced to below 50 percent, at which point it has a negative impact on vehicle response. This is logical since TEFs have direct authority over pitch motion, but to a lesser degree than roll. Thus, in the final controller, a pitch axis performance weight of 0.75 is used.

The effects of the yaw axis performance weight are shown in Figures C.5 – C.8. The yaw axis performance weight is decreased while the roll weight is held at one and the pitch axis is 0.5. Here, the pitch axis value is chosen for the sole purpose of making it easier to inspect the effect of the yaw axis changes. As expected, changing the yaw axis performance variable has a negligible effect on the vehicle response. In fact, the most obvious impact of decreasing the yaw axis performance weight is to decrease the commanded TEF deflections dramatically, as seen in Figure 4.17. For this reason, the yaw axis performance weighting variable is set to zero in the final control design. If, however, future designs incorporate the tail rotor, the value should be reset to one.

Figure 4.17. TEF Deflections: Varying Yaw Axis Performance Weights

As shown in this analysis, tailoring the performance weights is an essential part of the control synthesis. By reducing the performance weighting functions in the pitch and yaw axes, the overall vehicle response is improved and the TEF deflection requirements are lowered. The resulting weighting functions are

$$\underline{W}_p = \begin{bmatrix} 1 & 0 & 0 \\ 0 & 0.75 & 0 \\ 0 & 0 & 0 \end{bmatrix}. \tag{4.3}$$

4.2.4 Effect of Trailing Edge Flap Size

The physical size of the trailing edge flaps is the subject of the next series of simulations and studies. In Chapter 2, the authority analysis predicted that a TEF with a 0.2 chord ratio located from 70 to 85 percent of the blade span would

be adequate to reject gusts in a 30-degree, 30-knot WOD condition. Using a controller designed with this size flap, a series of simulations are performed while varying both span ratio, span-wise location, and chord ratio. Here, the values obtained from the previous studies are used for the performance weights (given by Eqn. 4.3) and the upper actuator frequency design variable (10 radians per second).

The results of the span-wise variations are illustrated in Figures C.9 – C.12. The locations of the TEFs that are considered are: 0.7R – 0.85R, 0.75R – 0.9R, 0.7R – 0.9R, and 0.65 – 0.9R, where R is the rotor radius. Different TEF spans and locations result in minimal differences in performance as each size considered was able to reduce the vehicle response by approximately 90 percent in roll rate and 30 percent in pitch rate. As expected, the longer flaps are able to do this with smaller TEF deflections. The same is true for moving the flap outboard. Increasing the TEF span ratio from 15 percent to 25 percent reduces the maximum deflection by 0.5 degrees (with the center of the flap at the same location in each case). The magnitude of deflections for all of the span ratios remain below the saturation point of five degrees. Thus, the original TEF span ratio and location are sufficient for gust alleviation.

The results of the chord ratio study are included in Figures C.13 – C.16. Chord ratios of 0.15c, 0.2c, and 0.25c are considered. As was the case in the span-wise study, the vehicle angular response is very similar with each chord ratio. Using the largest trailing edge flap, however, reduces the maximum required TEF deflection by 0.4 degrees, though deflections in all cases remain below five degrees. These results support the original TEF sizing as sufficient for gust alleviation. If smaller deflections are needed in future analyses, the size and location of the TEF could be altered accordingly.

4.2.5 Resulting Trailing Edge Flap Size and Controller

Based on the results of the previous variational studies, parameters in the control design synthesis and the trailing edge flap size are chosen. Controllers designed with these variables are used for the remainder of the simulations. The performance weighting functions on the vehicle angular rate in degrees per second are given by

$$\underline{W}_p = \begin{bmatrix} 1 & 0 & 0 \\ 0 & 0.75 & 0 \\ 0 & 0 & 0 \end{bmatrix}. \tag{4.4}$$

The actuator weighting functions are

$$\underline{W}_{act} = \begin{bmatrix} \frac{s+2}{s+10} & 0 & 0 & 0 \\ 0 & \frac{s+2}{s+10} & 0 & 0 \\ 0 & 0 & \frac{s+2}{s+10} & 0 \\ 0 & 0 & 0 & \frac{s+2}{s+10} \end{bmatrix}. \tag{4.5}$$

The trailing edge flap size is

$$\begin{aligned} \frac{c_f}{c} &= 0.2, \\ \frac{b_f}{b} &= 0.15, \\ \text{Location} &= 0.7R - 0.85R. \end{aligned} \tag{4.6}$$

4.3 Trailing Edge Flap Controller Results

Simulations are performed for various WOD conditions while the helicopter is hovering over landing spot 8. Because the gust filters for a specific airwake are incorporated in the TEF controller design, the controller should be scheduled by

WOD condition. The results of simulations in a 30-degree, 30-knot WOD airwake of the controller designed specifically for that condition are shown in Figures 4.18 – 4.22. This flight condition was found to have unacceptably high pilot workload during the JSHIP program [5] and is used as the design point for this analysis. The maximum vehicle roll rate response is reduced by 91 percent, while the pitch rate response is reduced by 32 percent. The attitude response is reduced by 79 percent and 13 percent in the roll and pitch axes, respectively. In order to achieve this response, the TEFs see a maximum deflection of 4.5 degrees (Figure 4.20). Although this exceeds the desired maximum deflection of three degrees, it remains below the saturation point of five degrees. If the chosen actuator cannot achieve these deflections at the time of implementation, the performance would be degraded at the instances when the controller calls for the high deflections. However, the flaps remain below three degrees deflection for 98 percent of the time; thus, current actuator technology is capable of producing the reduction in vehicle response demonstrated for the vast majority of the flight. TEF deflection rates do not come close to their limit at any point in this flight condition.

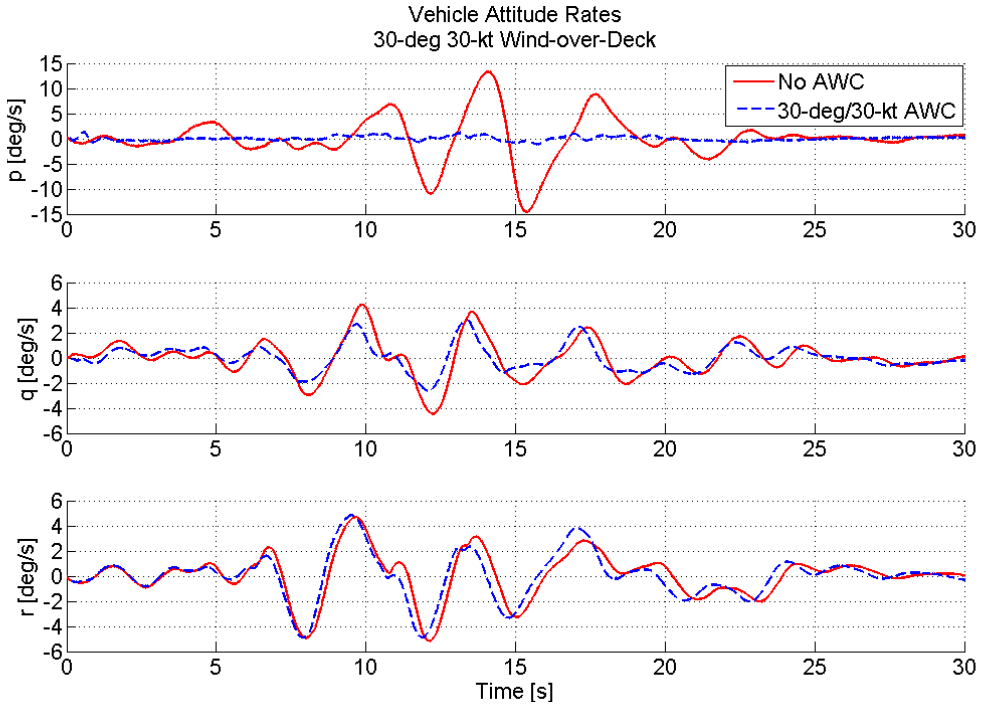

Figure 4.18. Vehicle Attitude Rates: 30-degree, 30-knot Wind-over-Deck

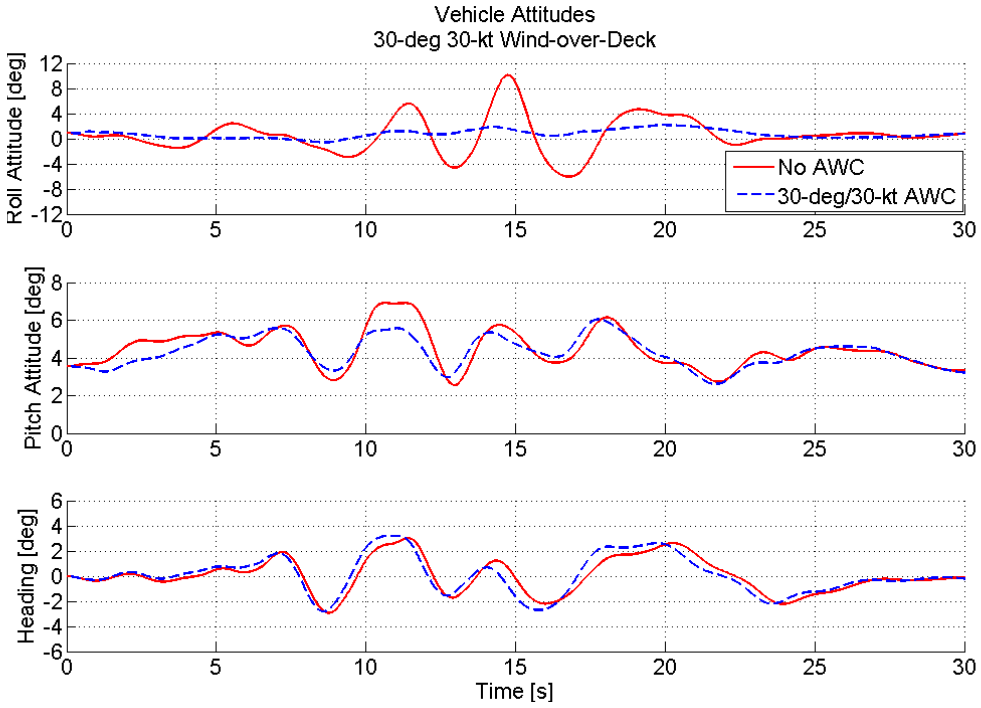

Figure 4.19. Vehicle Attitudes: 30-degree, 30-knot Wind-over-Deck

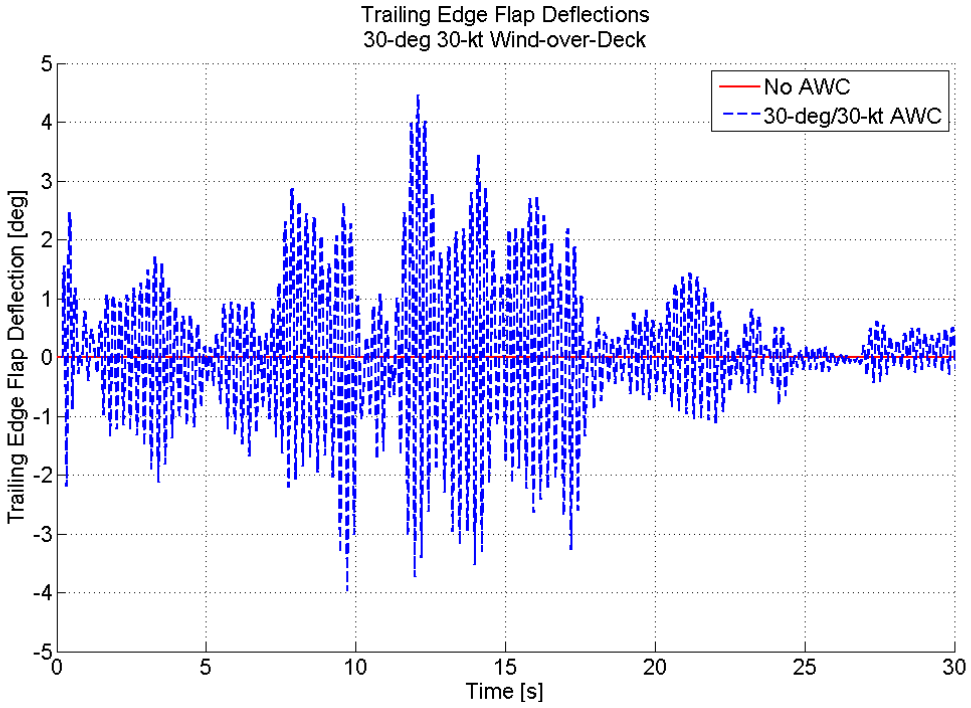

Figure 4.20. TEF Deflections: 30-degree, 30-knot Wind-over-Deck

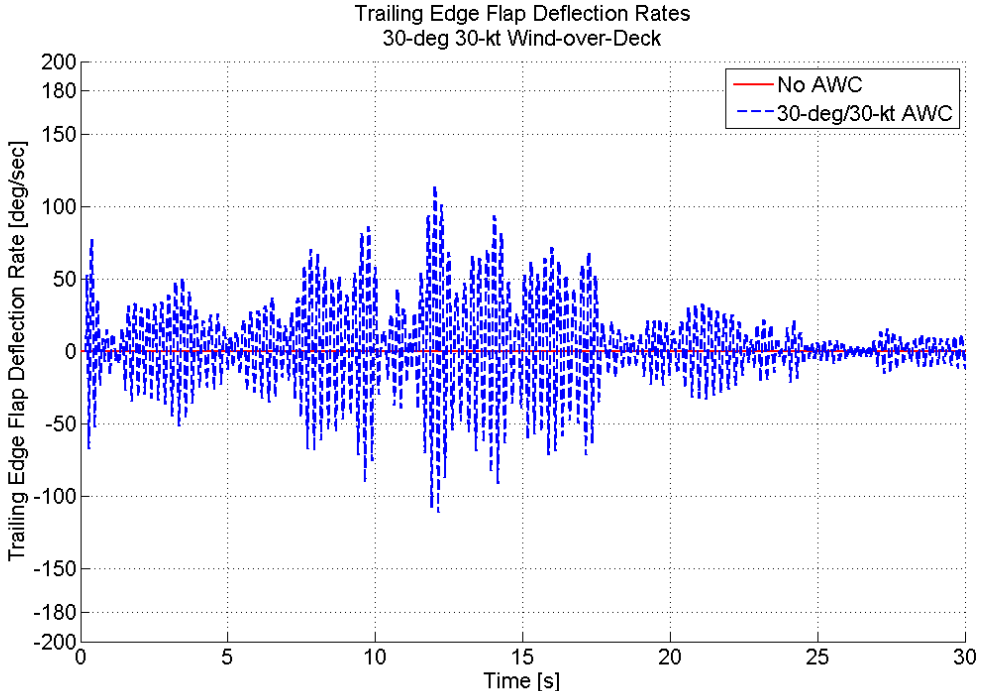

Figure 4.21. TEF Deflection Rates: 30-degree, 30-knot Wind-over-Deck

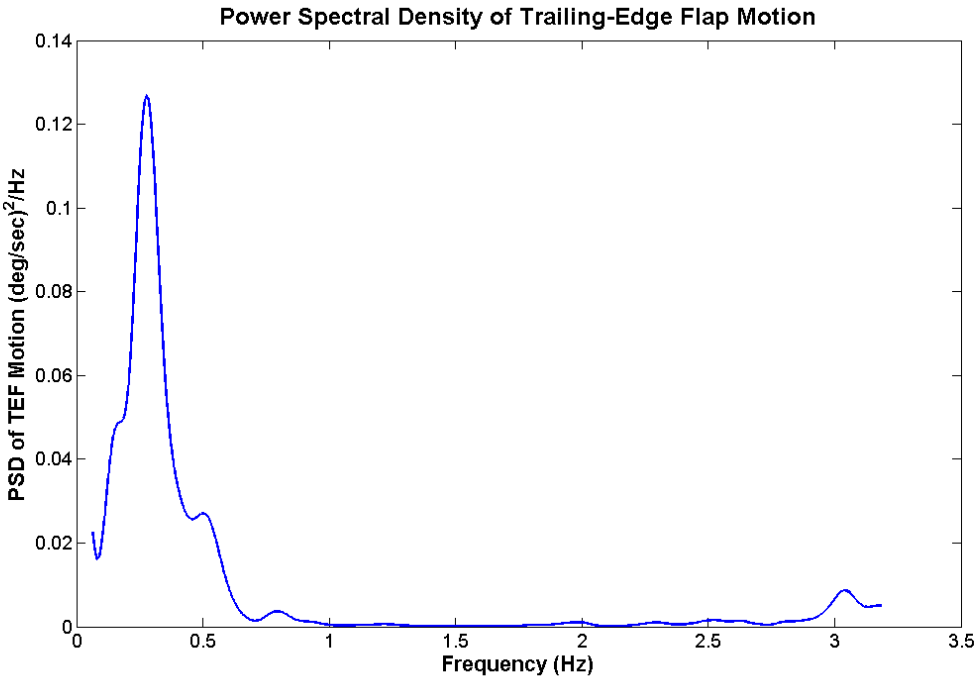

Figure 4.22. PSD of TEF Deflections: 30-degree, 30-knot Wind-over-Deck

Because the TEF airwake compensator is decoupled from the primary flight control system, switching to scheduled compensators would be relatively straightforward. They should be scheduled by the combination of helicopter, ship, landing spot, and WOD condition. However, a single controller chosen for a specific helicopter, ship, and landing spot – excluding the WOD condition – would be simpler. Thus, the next results illustrate the effects of using the controller designed for the 30-degree, 30-knot WOD condition on other wind conditions. In Figures C.17 – C.20, the results of a 0-degree, 30-knot wind are examined without a TEF controller, with a TEF controller designed for the WOD condition, and with a TEF controller designed for a 30-degree, 30-knot wind. Between the two controllers, the reduction in vehicle response is almost indistinguishable. Although the TEF deflection history varies slightly, the deflections are both well below actuator limits. Thus, the controllers are equally effective.

Since the 30-degree, 30-knot controller was effective in the less severe flight condition than for which it was designed, it is tested on other cases. Figures C.21 – C.24 show a 0-degree, 40-knot wind. This condition is substantially less severe than the 30-degree, 30-knot case due to the ship's superstructure, which causes higher azimuth-angled winds to create more vorticity in the airwake. Thus, the TEFs can eliminate the gust response easily, without exceeding positive or negative one degree of deflection.

The most severe case considered – 30-degree, 40-knot WOD – is shown in Figures 4.23 – 4.26. The 30-degree, 30-knot controller is able to reduce the maximum roll rate by 84 percent, pitch rate by 41 percent, roll attitude by 59 percent, and pitch attitude by 12 percent. However, the commanded TEF deflections exceed three degrees approximately 4 percent of the simulation time. A scheduled controller may be able to reduce these deflection requirements. Regardless, the alleviation in vehicle response is substantial.

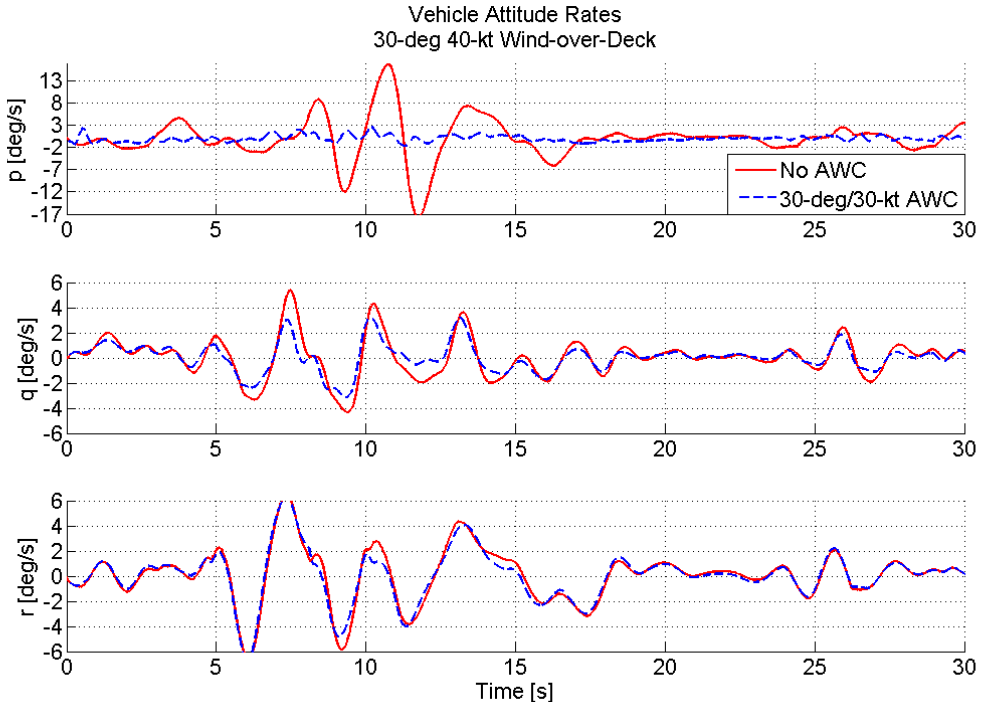

Figure 4.23. Vehicle Attitude Rates: 30-degree, 40-knot Wind-over-Deck

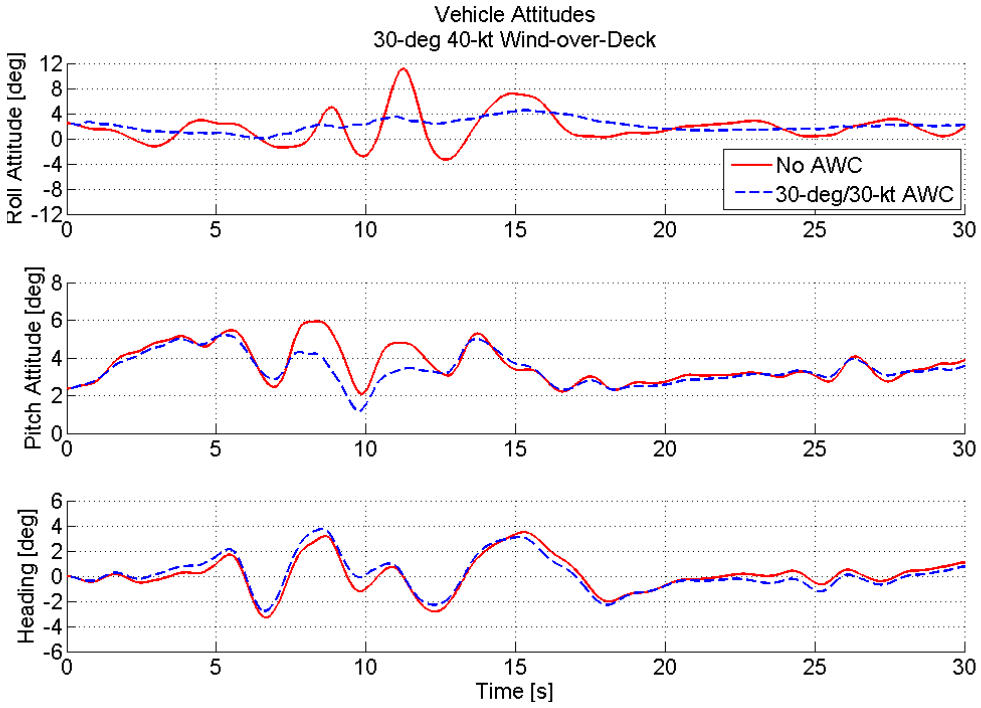

Figure 4.24. Vehicle Attitudes: 30-degree, 40-knot Wind-over-Deck

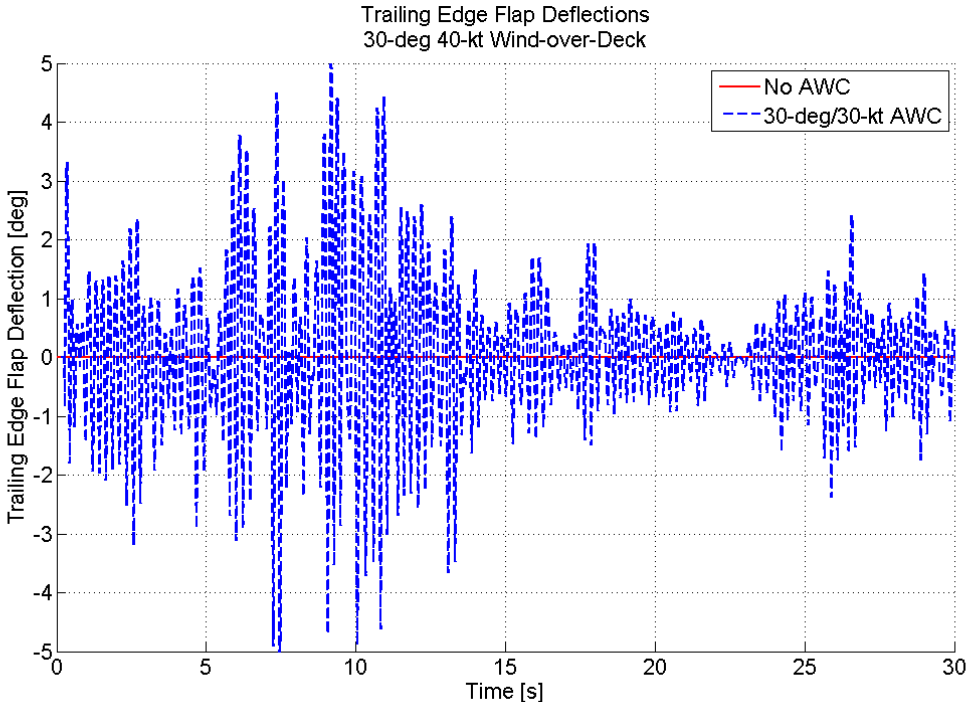

Figure 4.25. TEF Deflections: 30-degree, 40-knot Wind-over-Deck

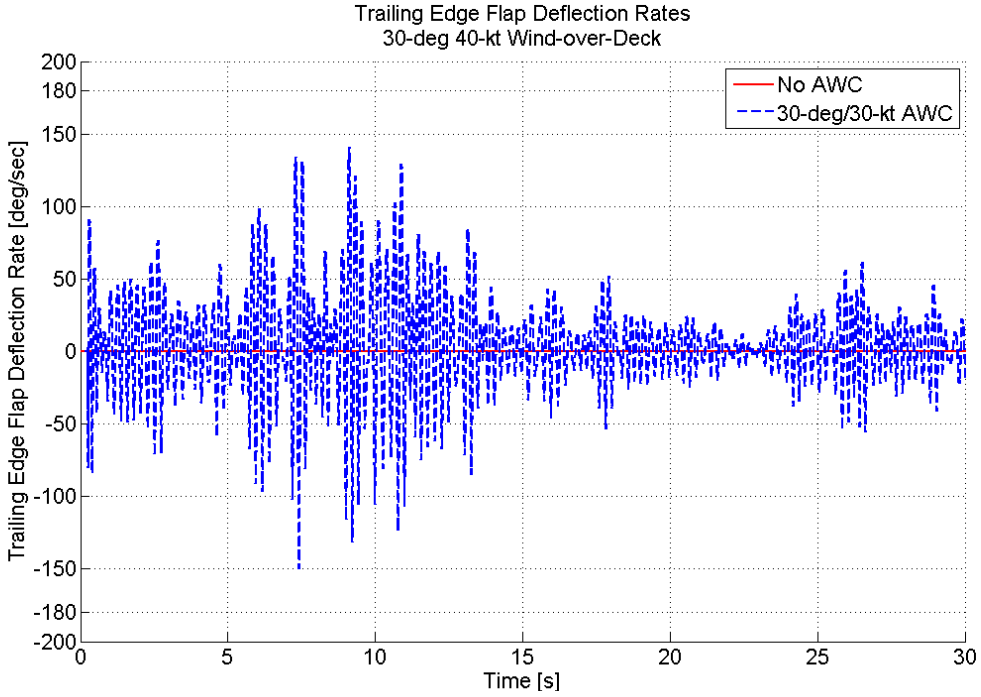

Figure 4.26. TEF Deflection Rates: 30-degree, 40-knot Wind-over-Deck

4.4 Comparison with Swashplate-Based Method

To provide an initial comparison of the effectiveness of the trailing edge flap airwake compensator to that of a swashplate-based method, a similar compensator that uses the swashplate and pedals is designed. Previous researchers [5] designed such an airwake compensator. After testing, the controller was modified to improve its performance and to reduce its order [5]. It is desirable to use an unmodified version of a swashplate controller since the states of the TEF controller are not changed after initial testing. Thus, a new swashplate controller is designed specifically for this study. Like the trailing edge flap controller, it uses H_2 analysis and is full-order. The actuator weighting and performances matrices that are used by Horn et al. [5] are used and are

$$\underline{W}_p = \begin{bmatrix} 1 & 0 & 0 \\ 0 & 1 & 0 \\ 0 & 0 & 1 \end{bmatrix} \tag{4.7}$$

and

$$\underline{W}_{act} = \begin{bmatrix} 20\frac{s+2}{s+20} & 0 & 0 \\ 0 & 20\frac{s+2}{s+20} & 0 \\ 0 & 0 & 37\frac{s+2}{s+20} \end{bmatrix}, \tag{4.8}$$

where the performance variables are the three vehicle body axis angular rates, measured in degrees per second. The inputs to the system that are affected by the actuator weighting functions are the equivalent lateral and longitudinal control stick deflections and the pedal deflection, all given in inches. The maximum possible deflection of the pedals is different than the range of the control stick. Thus,

the scale factors are chosen to put equal percentage weighting on each control input. Using these values for weighting functions, an H_2 synthesis is performed to create the airwake compensator.

The resulting swashplate and pedals controller is compared to the trailing edge flap controller for a 30-degree, 30-knot wind in Figures 4.27 – 4.30. The vehicle response is shown in Figures 4.27 – 4.28. In the roll axis, the TEFs are slightly more effective than the swashplate; however, the swashplate is more effective in the pitch motion alleviation. The difference may be attributed to the chosen performance variables. As expected, the yaw response is only alleviated by the controller that uses the pedals and the tail rotor. Overall, the performance of the TEFs is comparable to that of the swashplate.

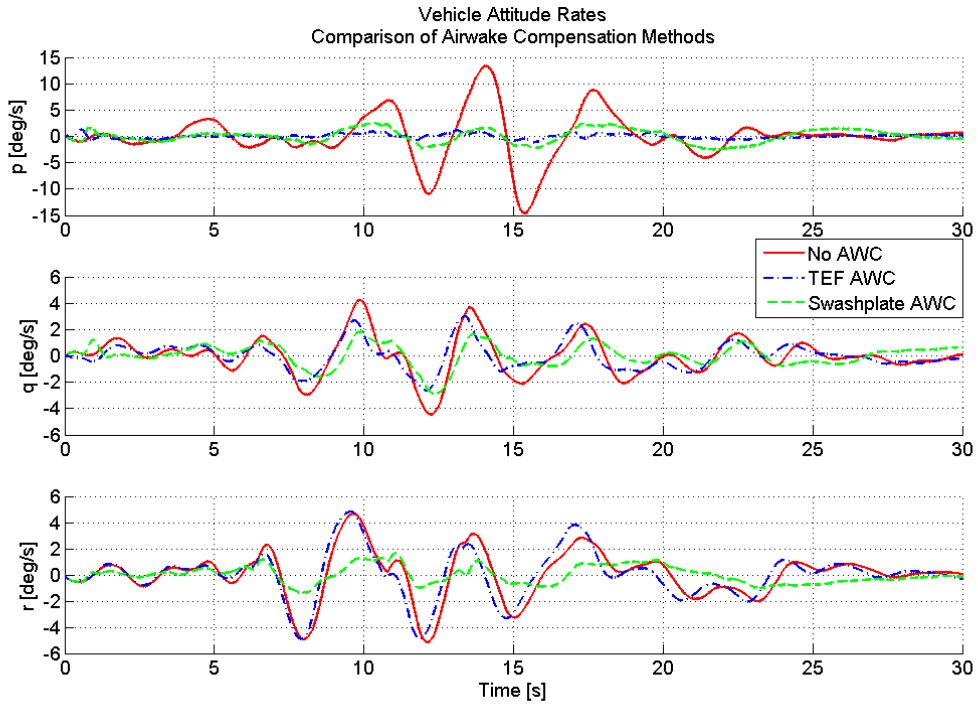

Figure 4.27. Vehicle Attitude Rates: Airwake Compensation Method Comparison

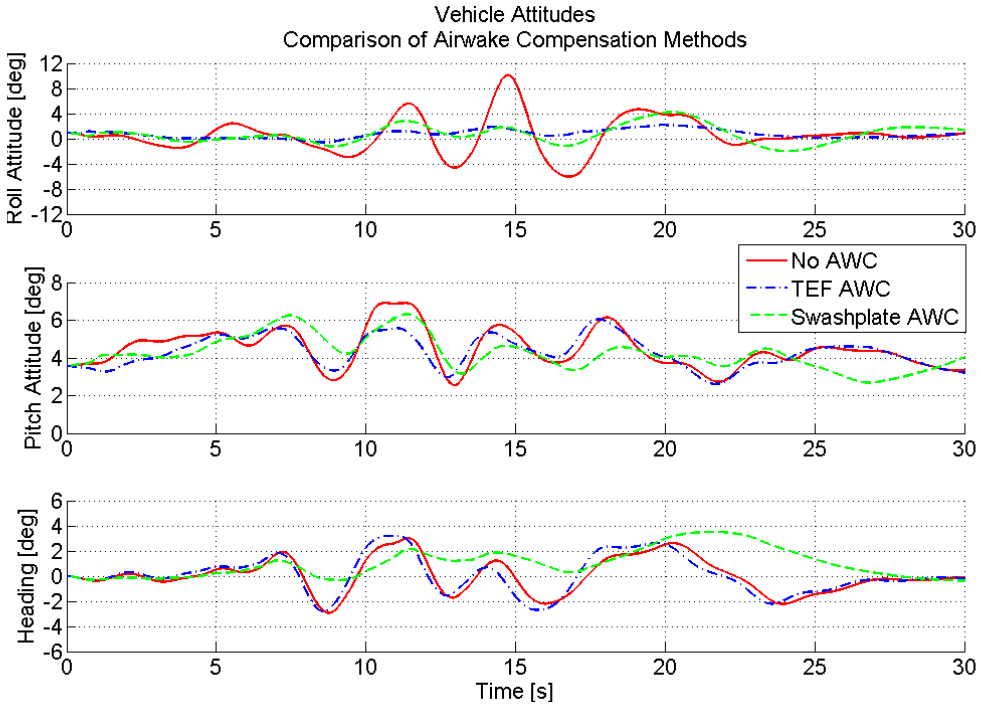

Figure 4.28. Vehicle Attitudes: Airwake Compensation Method Comparison

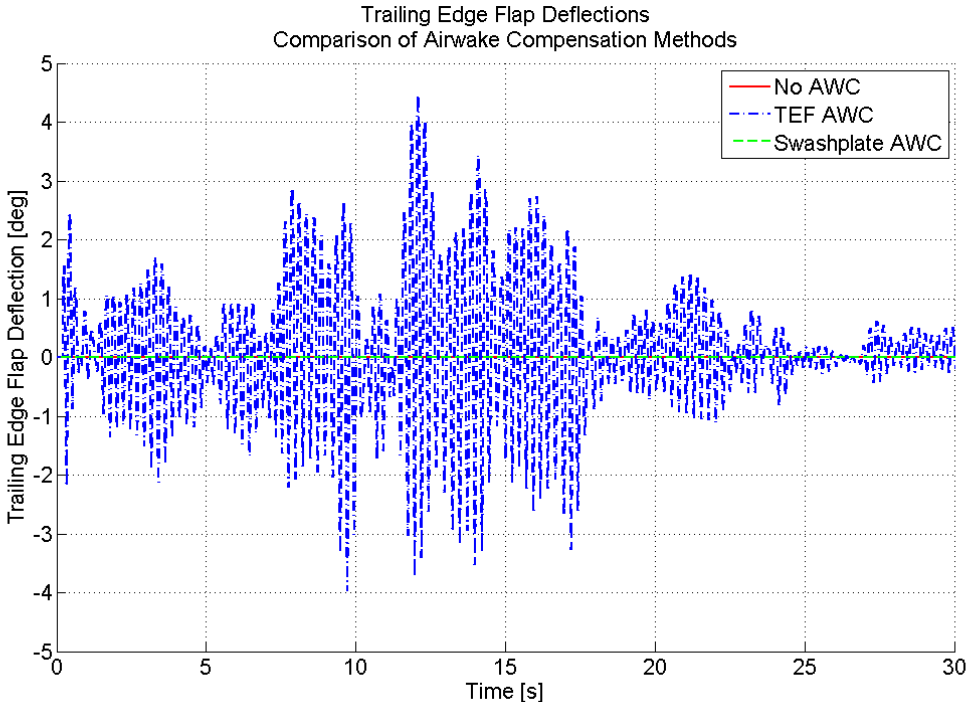

Figure 4.29. TEF Deflections: Airwake Compensation Method Comparison

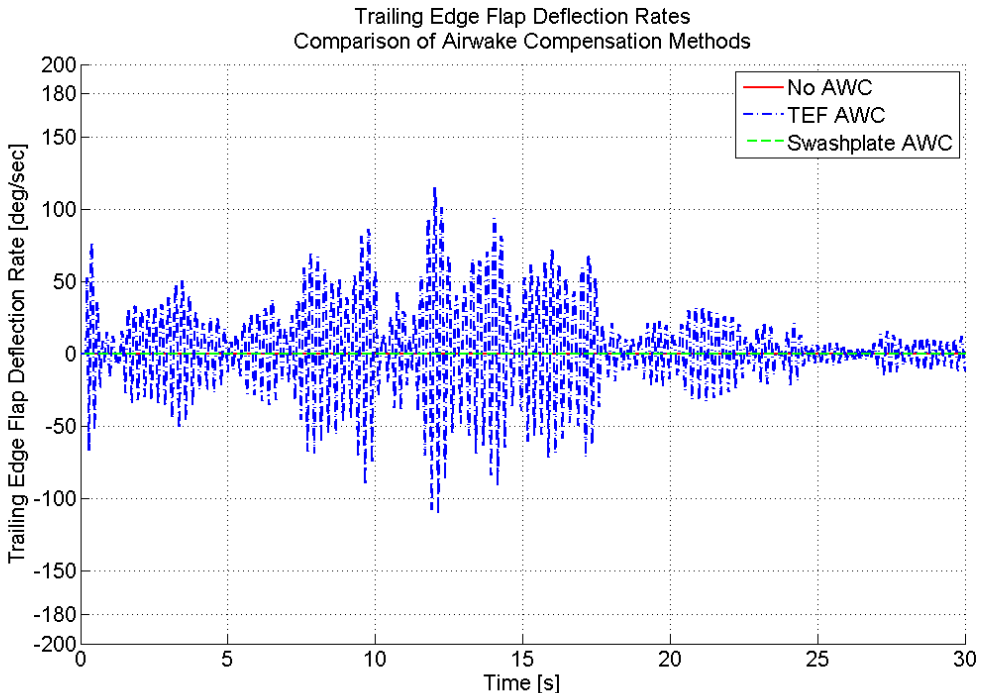

Figure 4.30. TEF Deflection Rates: Airwake Compensation Method Comparison

Chapter 5

Summary, Future Work, and Conclusions

Operating near a ship is one of the most challenging missions for a helicopter. The turbulent, unsteady flowfield can result in sudden and large vehicle motions. For safety purposes, operational limits are imposed based on the helicopter, the ship, and the current wind environment. If vehicle response could be alleviated and pilot workload could be reduced, operational capabilities could potentially be expanded. For this purpose, trailing edge flaps are investigated as gust alleviation mechanisms during helicopter shipboard dynamic interface operations.

Until now, time-domain, non-harmonic controllers have seen little use for automated on-blade actuation, since the primary uses for TEFs – vibration control, noise reduction, and blade loads control – use harmonic control. Additionally, using on-blade actuation is a novel method for gust alleviation. Previous research has used the primary flight control effectors, including the swashplate and tail rotor. This study expands upon that by combining the benefits of on-blade actuation and gust alleviation control methods. The system uses trailing edge flaps for gust disturbance rejection, while the swashplate provides primary flight control.

5.1 Analysis Summary

Using a quasi-steady aerodynamic model to represent the change in lift caused by trailing edge flap deflections, TEFs are added to the existing GENHEL flight dynamics model of the UH-60A Black Hawk helicopter. At each segment along the blade span where the TEF is present, the effect of the TEF is added to that blade segment's lift coefficient. A trailing edge flap that is 20 percent of the blade chord, spanning from 70 percent to 85 percent of the rotor radius, is used.

To incorporate the trailing edge flaps for gust disturbance rejection, a TEF controller is added to a standard model-following controller, both of which operate on the tracking error of the vehicle angular rates. The ship airwake spectral properties are incorporated in the TEF controller design. A robust H_2 control synthesis is performed in order to allow for variations in gust disturbances and model inaccuracies.

Following control development, the trailing edge flap airwake compensator and the model-following controller are implemented in the GENHEL flight simulation environment, along with CFD airwake data for an LHA-class ship. Simulations are performed while various parameters are altered. The effects of trailing edge flap size, trailing edge flap location, performance and actuation weights are analyzed in order to develop the trailing edge flap controller. A similar airwake compensator that uses the swashplate and pedals for gust rejection is designed for comparison.

5.2 Recommendations for Future Work

The performances of the trailing edge flap controller and the swashplate airwake compensator used in this study are comparable in terms of vehicle roll and pitch

rate reductions. Further analysis is required before determining if one system has a distinct advantage over the other. There are many areas that remain to be explored for using trailing edge flaps for gust alleviation that could alter performance or actuator requirements. Some of these involve improving the model, adjusting the controller, and taking new approaches. A few recommendations are detailed in this section.

5.2.1 Improvements in Trailing Edge Flap Model Fidelity

The addition of trailing edge flap pitching moment and drag models are strongly encouraged at this stage and before piloted simulations are performed. The pitching moment was not modeled in this research for several reasons. First, simplicity is desired in an initial feasibility study. Second, after proving that lift flaps are able to alleviate helicopter gust response, it is known that the higher authority moment flaps are also capable. Additionally, the flight dynamics simulation used in this study does not include torsion as a degree of freedom, eliminating the possibility of using moment flaps within the chosen simulation environment.

With pitching moment modeled, it is recommended that moment flaps also be considered for gust alleviation. The performance of trailing edge flaps for gust alleviation could be improved if the flaps were permitted to impart a pitching moment on the blade. Consequently, the TEFs will most likely be able to be smaller in size relative to the rotor blade, and they may be able to use less deflection than the results presented in this study while maintaining similar or even improved performance. Of course, relying on the TEFs to produce a large change in pitching moment requires a low torsional blade stiffness, which may be prohibitive and is another reason they were not considered in this analysis.

5.2.2 Improvements to the Controller Design

Similar to the possibilities of improving the model of the trailing edge flaps themselves, the controller design can also be examined for potential improvements. The improvements could be in terms of a new control approach or an adjusted control law.

5.2.2.1 Unexplored Advantages to Using Trailing Edge Flaps

Changing either the input or output of the TEF controller could impact its performance. One possibility worth exploring is using rotor state feedback. By using rotor states as an input to the controller, one could predict how the rotor blade and the vehicle are about to respond. Thus, one could impart TEF deflections in order to preempt vehicle motion. This could improve overall performance because the motion could be alleviated before it occurs. Additionally, one could command each trailing edge flap separately, providing individual blade control. In the current analysis, the TEFs are restricted with how they can move relative to one another. If they are able to move independently, improvements in performance may be possible.

5.2.2.2 Use of an Alternative Control Method

Another useful area of improvement is in reducing the complexity of the TEF controller design. Robust controllers have yet to see widespread implementation in industry due to the high number of states that are produced in the control synthesis. Model-order reduction could be performed on the current TEF controller; however, the number of states would still be high. Alternatively, one could attempt to construct a non-robust controller for this purpose, while paying close attention

to minimizing the performance degradation. Ultimately, a balance between controller performance and ease of implementation must be sought.

5.2.3 Improvements in Swashplate and Trailing Edge Flap Controller Comparison

The swashplate-based airwake compensator designed for this study uses an identical design method as the TEF controller. Comparison of the two controllers shows that the TEFs are able to reduce vehicle angular response to gusts as well as the swashplate can. However, a more thorough comparison could be conducted. Model order reduction is desirable on both controllers and may impact their performances. Also, the two controllers and their impact on the vehicle response to pilot input should be compared more thoroughly, including in the frequency domain. Additionally, ease of implementation and physical limitations of the system are important. Rate and fatigue limits of both systems should be investigated. Since TEFs are often required to move much faster for vibration and noise reduction, the rate limits should not affect the TEF controller. However, adding an additional system of hardware makes implementation more difficult. On the other hand, separating the actuators of the gust rejection control system from the primary flight control system could be considered preferable. Ultimately, a myriad of factors affect which system is preferable if the performance is comparable.

5.3 Conclusions

Gust response rejection could have a substantial impact on helicopter safety and operational capabilities in the shipboard environment. Based on the results of this study, trailing edge flaps are capable of imparting considerable gust response

reduction in terms of vehicle angular motion. Weighting parameters included in the control design have a significant impact on the magnitude of the TEF deflections required to reject gusts. Giving preference to angular motion reduction in the roll axis and low frequency TEF motions results in the controller with the combination of best performance across the roll, pitch, and yaw axes and lowest TEF deflections. For all cases considered, the trailing edge flap deflections remain below saturation levels. The deflection rates are within actuation capabilities. Substantial reduction in the vehicle angular rate response to the ship airwake is achieved.

The trailing edge flap controller is able to reduce vehicle response in a variety of wind-over-deck condition simulations. While hovering in a 30-degree, 30-knot wind over landing spot 8 of an LHA-class ship, the Black Hawk's maximum roll rate is reduced by 91 percent. The pitch rate is reduced by 32 percent. The maximum trailing edge flap deflection is approximately 4.5 degrees, though it remains below three degrees for 98 percent of the simulation time. In more benign flight conditions, the trailing edge flaps are able to reduce the vehicle gust response as well as the more severe case while using substantially smaller deflections, including less than one degree of deflection for a 0-degree, 40-knot wind. When the controller designed for the 30-degree, 30-knot WOD condition is used on a 30-degree, 40-knot wind, the trailing edge flap deflections saturate at five degrees numerous instances during the simulations and exceed three degrees for four percent of the maneuver time. Despite the deflection limitations, the vehicle response is significantly improved in this worst scenario that was considered. The maximum roll rate is reduced by 84 percent; pitch rate is reduced by 41 percent; roll attitude is alleviated by 59 percent; and pitch attitude is decreased by 12 percent.

The gust alleviation capabilities of this controller are comparable to that of a similar swashplate-based controller, when compared in terms of vehicle roll and

pitch angular motion reduction. Minor differences in performance can be attributed to parameters chosen in the control synthesis. Whether the use of trailing edge flaps or the swashplate is preferable may depend on the outcome of more comprehensive comparisons between the two technologies.

Appendix A

Numerical Simulation Input Data

A.1 UH-60A Black Hawk Properties

Table A.1. Vehicle Properties

Weight	W	16825	lbs
Longitudinal CG Offset	x_{cg}	1.525	ft
Lateral CG Offset	y_{cg}	0	ft
Vertical CG Offset	z_{cg}	-5.825	ft
Lon. Stabilator Offset	x_{ht}	29.925	ft
Lat. Stabilator Offset	y_{ht}	0	ft
Vert. Stabilator Offset	z_{ht}	-5.915	ft
Lon. Tail Rotor Offset	x_{tr}	32.565	ft
Lat. Tail Rotor Offset	y_{tr}	0	ft
Vert. Tail Rotor Offset	z_{tr}	0.805	ft
Distances are measured with respect to the hub.			

Table A.2. Rotor Properties

Number of Blades	N_b	4	
Radius	R	26.8	ft
Chord	c	1.73*	ft
Twist	θ_{tw}	varies	
Angular Velocity	Ω	258	RPM
Shaft Tilt	Ω_{Sx}	3	$degrees forward$
Airfoil Section	SC1095*		
Lock Number	γ	6.5344	
Solidity	σ	0.0822	
Profile Drag Coefficient	c_{d0}	0.0076	
Blade Mass	M_b	7.79	$slugs$
Flap Hinge Offset	e_β	1.25	ft
Lag Hinge Offset	e_ζ	1.25	ft
Root Cut Out		3.83	ft
1^{st} Nondimensional Rotating Flap Frequency	ν_β	1.04	
1^{st} Nondimensional Rotating Lag Frequency	ν_ζ	2.71	
1^{st} Nondimensional Rotating Torsion Frequency	ν_θ	4.27	
Flapping Moment of Inertia	I_β	1861	$slug - ft^2$
Lag Moment of Inertia	I_ζ	1861	$slug - ft^2$
Torsion Moment of Inertia	I_f	0.978	$slug - ft^2$
Inertial Flap – Torsion Coupling	I_x	1.5147	

**varies spanwise*

A.2 GENHEL Settings

Table A.3. Vehicle Properties and Initial Conditions

Weight/CG Location		
Weight	16825	*lbs*
Fuselage Station CG	355	*in*
Waterline Station CG	248.2	*in*
Buttline CG	0	*in*
Initial Conditions		
Barometric Altitude	100	*ft*
Speed	0	*kts*
Latitude Location	0	*deg N*
Longitude Location	0	*deg W*
x CG Offset	0	*ft*
y CG Offset	0	*ft*
Pitch Attitude	0	*deg*
Yaw Attitude	0	*deg*
Heading	0	*deg*
Other Settings		
Inflow Model	Pitt-Peters Dynamic Inflow	
Ground Effect	Yes	
Number of Blade Segments	30	
Zero Sideslip Speed	60	*kts*

A.3 Settings for the Authority Analysis

Table A.4. Control Settings Used in the Trailing Edge Flap Authority Analysis

Active Controllers	Engine Control Unit
	Automatic Stabilitor Control
	TEF Open Loop Harmonic
Commands	Varying 1/rev open loop harmonic TEF commands
Time step	0.00323 seconds (5 degrees)
Wind	0 kts, 0 deg
Turbulence	None

A.4 Settings for the Control Development

Table A.5. Control Settings Used in the Trailing Edge Flap Controller Analysis

Active Controllers	Engine Control Unit
	Automatic Stabilitor Control
	Model Following Controller
	TEF Airwake Compensator
	Translational Rate Controller (TRC)
Commands	None for hover (TRC holds station)
Time step	0.00323 seconds (5 degrees)
Wind	Various WOD Conditions
Turbulence	Various Airwake Conditions

Table A.6. Control Settings Used in the Swashplate Airwake Compensator Analysis

Active Controllers	Engine Control Unit
	Automatic Stabilitor Control
	Model Following Controller
	Airwake Compensator
	Translational Rate Controller (TRC)
Commands	None for hover (TRC holds station)
Time step	0.01 seconds (15.4699 degrees)
Wind	Various WOD Conditions
Turbulence	Various Airwake Conditions

Appendix B

Numerical Methods

B.1 Linear Model Extraction

The linear models used in the model-following controller and the trailing edge flap control design are created numerically from GENHEL using a perturbation method. The mathematical derivation of this method is included here and can be found in Reference [38].

The Taylor series expansion of the state equation taken around the trim point is

$$\dot{\vec{x}} + \delta\dot{\vec{x}} = f(\vec{x}_{trim}, \vec{u}_{trim}, \vec{w}_{trim}) + \frac{\partial f}{\partial \vec{x}}\delta\vec{x} + \frac{\partial f}{\partial \vec{u}}\delta\vec{u} + \frac{\partial f}{\partial \vec{w}}\delta\vec{w} + H.O.T.. \qquad \text{(B.1)}$$

The partial derivative terms represent Jacobian matrices. Higher order terms are neglected.

Because the Taylor series expansion was taken about the equilibrium point,

$$\vec{0} = \dot{\vec{x}} = f(\vec{x}_{trim}, \vec{u}_{trim}, \vec{w}_{trim}). \qquad \text{(B.2)}$$

This yields

$$\delta\dot{\vec{x}} = f(\vec{x}_{trim}, \vec{u}_{trim}\vec{w}_{trim}) + \frac{\partial f}{\partial \vec{x}}\delta\vec{x} + \frac{\partial f}{\partial \vec{u}}\delta\vec{u} + \frac{\partial f}{\partial \vec{w}}\delta\vec{w}. \tag{B.3}$$

This is of the same form as the desired state equations:

$$\dot{\vec{x}} = \underline{A}\vec{x} + \underline{B}\vec{u} + \underline{G}\vec{w}. \tag{B.4}$$

Thus, to obtain the A, B, and G matrices of the linear model, the first partial derivatives are estimated numerically. The Taylor series expansion of a single variable function, $v = v_e$, taken about an equilibrium point is

$$y_{i+1} \equiv y(v_e + h) = g(v_e) + h\frac{\partial g}{\partial v}(v_e) + \frac{h^2}{2!}\frac{\partial^2 g}{\partial v^2}(v_e) + H.O.T., \tag{B.5}$$

$$y_{i-1} \equiv y(v_e - h) = g(v_e) - h\frac{\partial g}{\partial v}(v_e) + \frac{h^2}{2!}\frac{\partial^2 g}{\partial v^2}(v_e) + H.O.T.. \tag{B.6}$$

Thus, the first derivative of the function is

$$\left.\frac{\partial g}{\partial v}\right|_{v=v_{trim}} = \frac{y_{i+1} - y_{i-1}}{2h} - \frac{h^2}{3!}\frac{\partial^3 g}{\partial v^3}(v_e) - H.O.T.. \tag{B.7}$$

Neglecting the higher order terms results in the first partial derivative approximation,

$$\left.\frac{\partial g}{\partial v}\right|_{v=v_{trim}} = \frac{y_{i+1} - y_{i-1}}{2h}, \tag{B.8}$$

which is used to construct the state matrices for the linear model.

Appendix C

Simulation Results

C.1 Performance Weighting Choice Results

C.1.1 Varying Pitch Axis Performance Weight

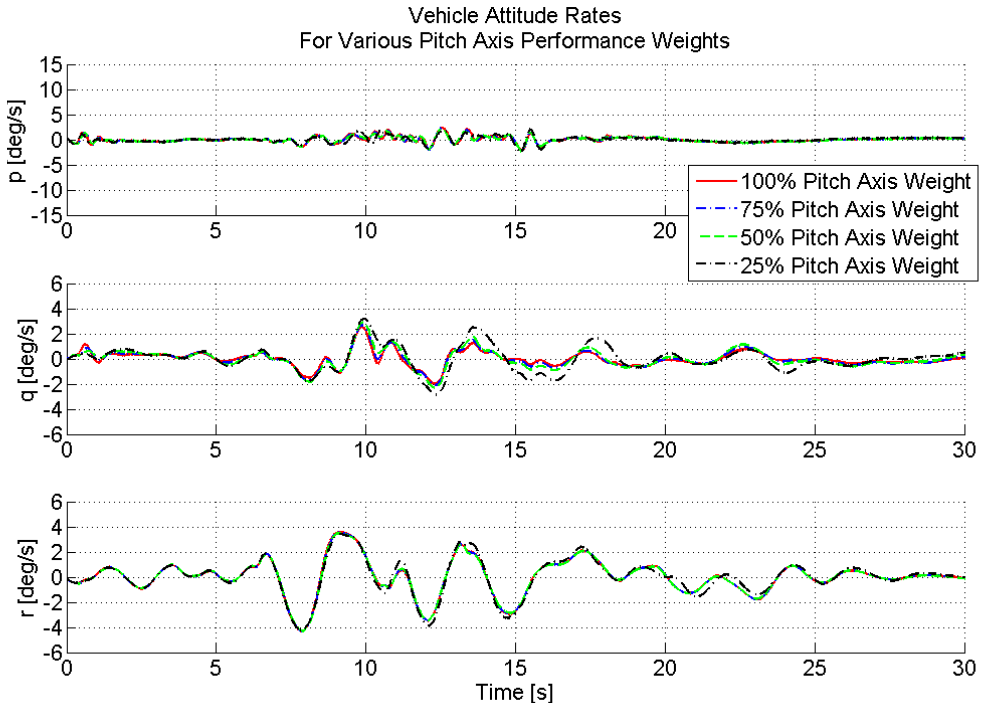

Figure C.1. Vehicle Attitude Rates: Varying Pitch Axis Performance Weights

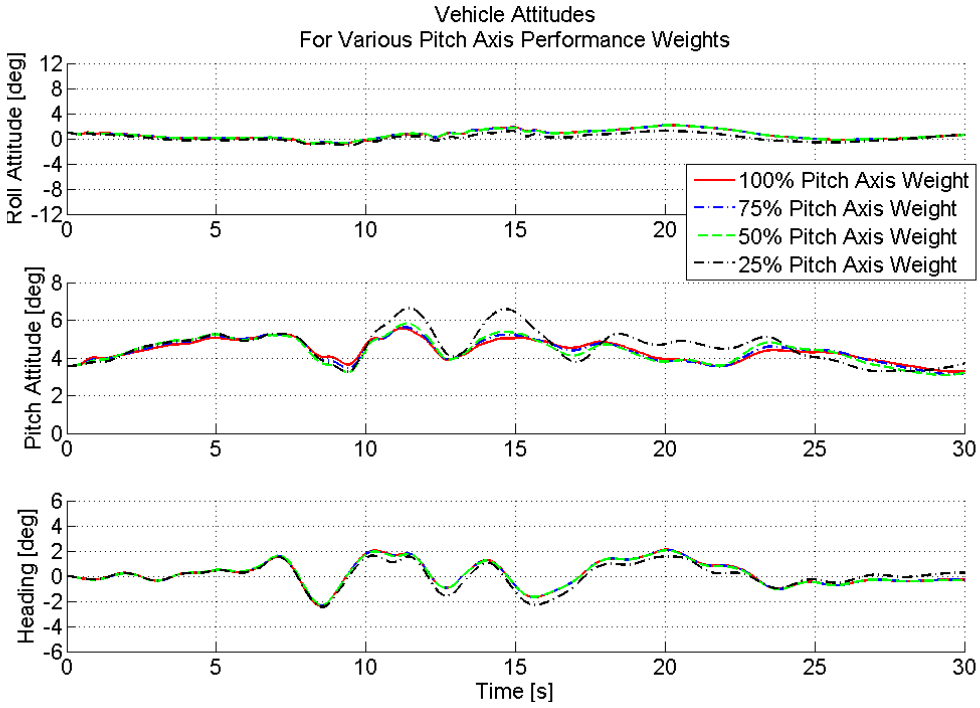

Figure C.2. Vehicle Attitudes: Varying Pitch Axis Performance Weights

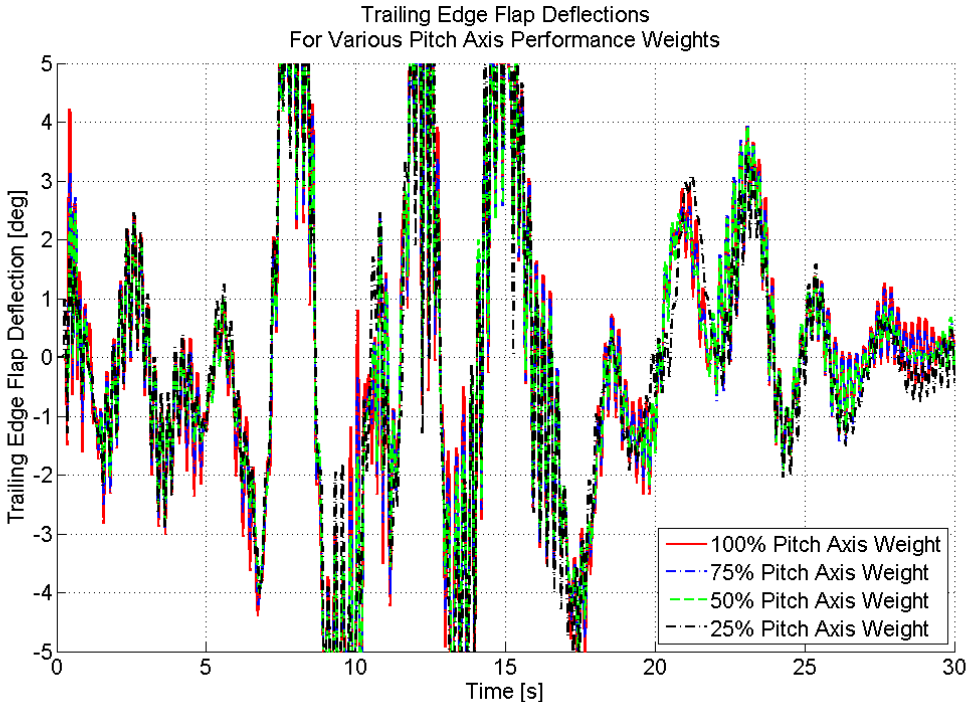

Figure C.3. TEF Deflections: Varying Pitch Axis Performance Weights

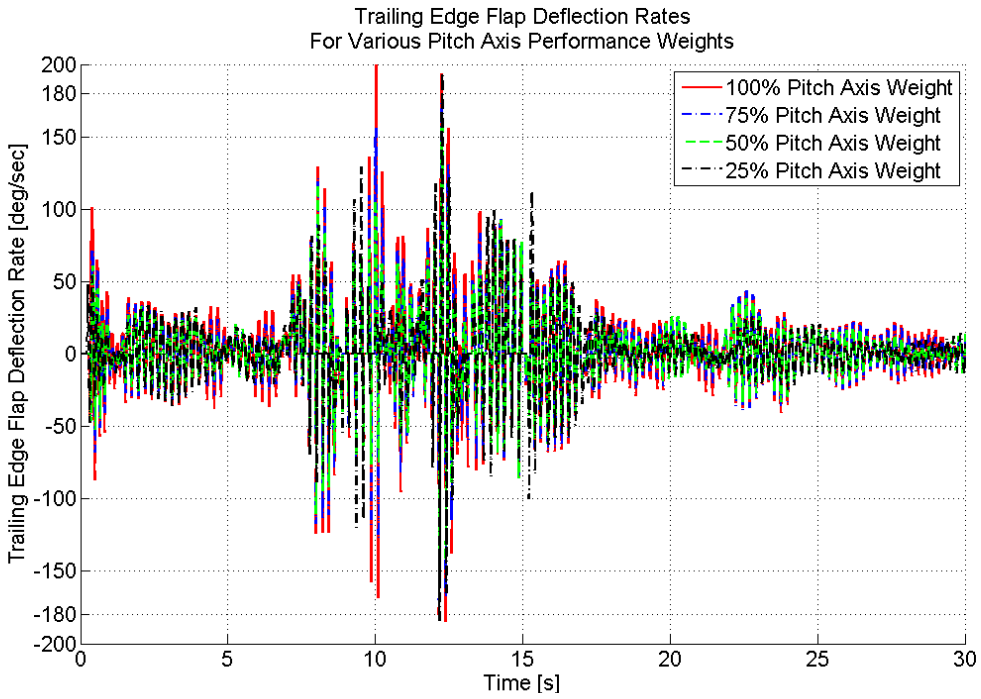

Figure C.4. TEF Deflection Rates: Varying Pitch Axis Performance Weights

C.1.2 Varying Yaw Axis Performance Weight

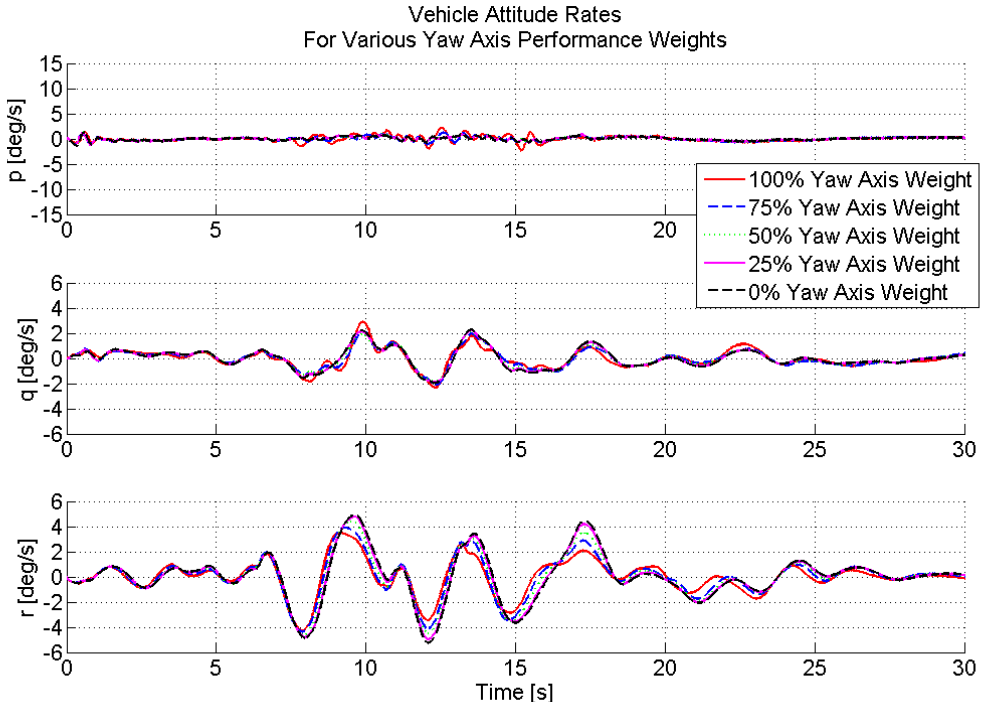

Figure C.5. Vehicle Attitude Rates: Varying Yaw Axis Performance Weights

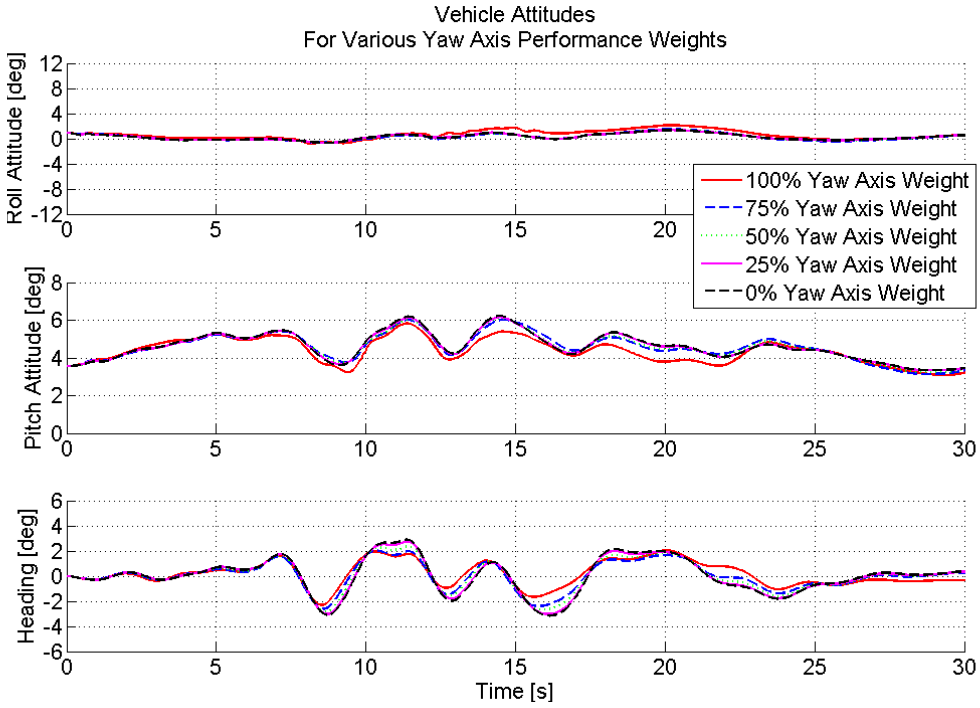

Figure C.6. Vehicle Attitudes: Varying Yaw Axis Performance Weights

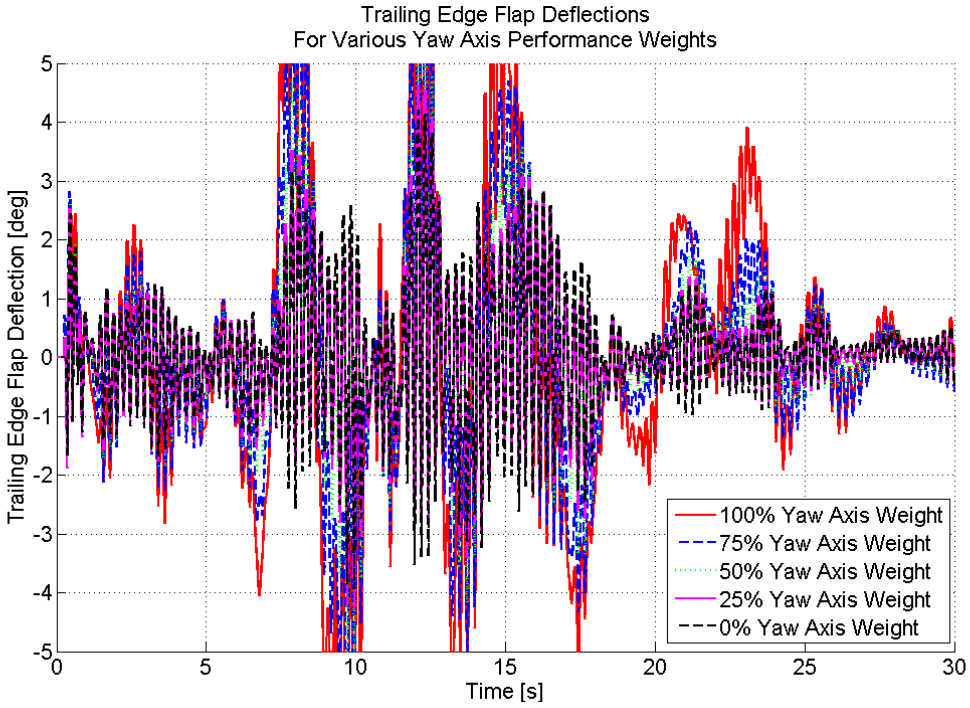

Figure C.7. TEF Deflections: Varying Yaw Axis Performance Weights

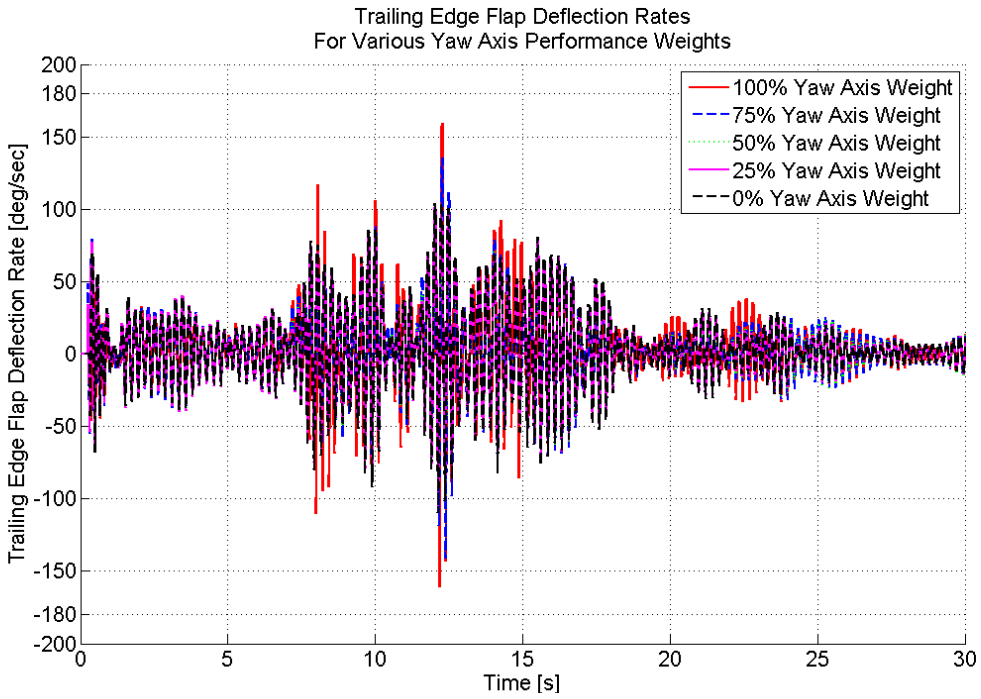

Figure C.8. TEF Deflection Rates: Varying Yaw Axis Performance Weights

C.2 Trailing Edge Flap Geometry Results

C.2.1 Varying TEF Span Ratio and Location

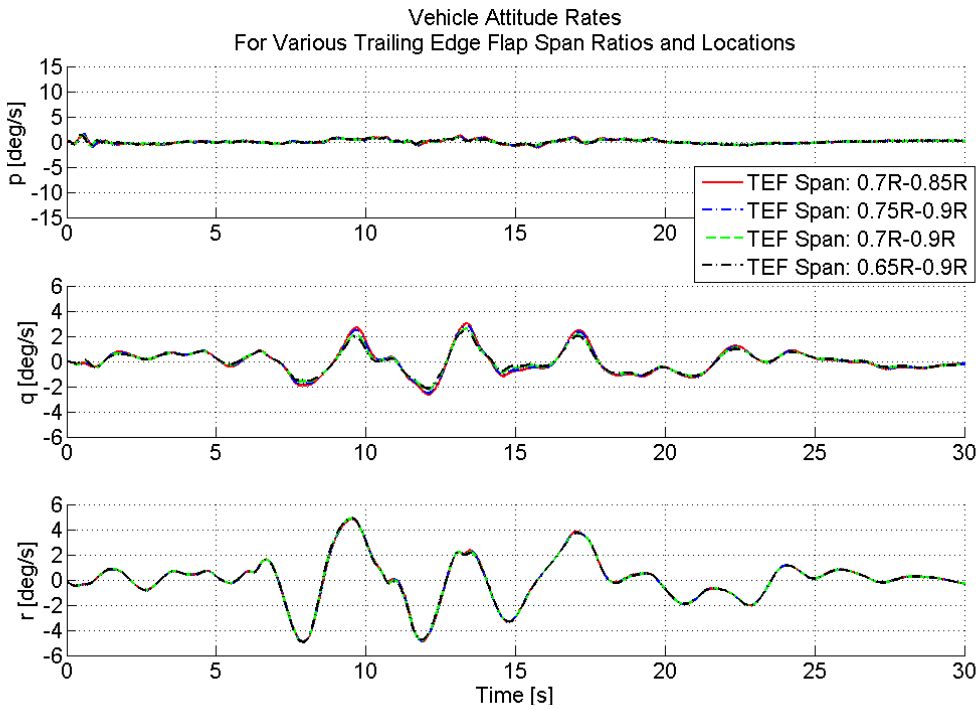

Figure C.9. Vehicle Attitude Rates: Varying TEF Span Ratio and Location

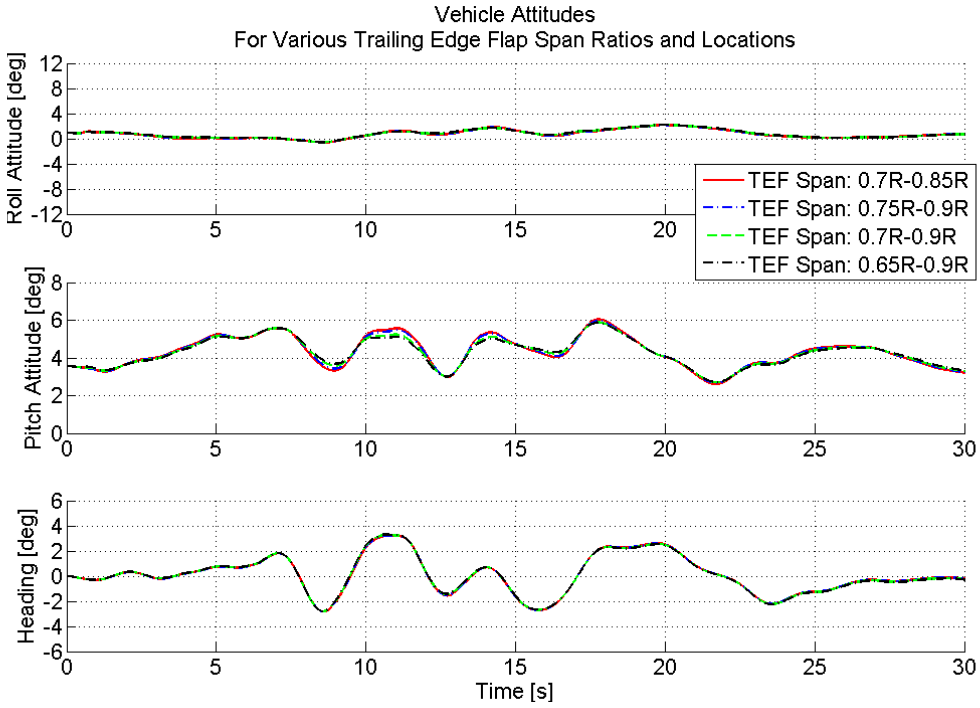

Figure C.10. Vehicle Attitudes: Varying TEF Span Ratio and Location

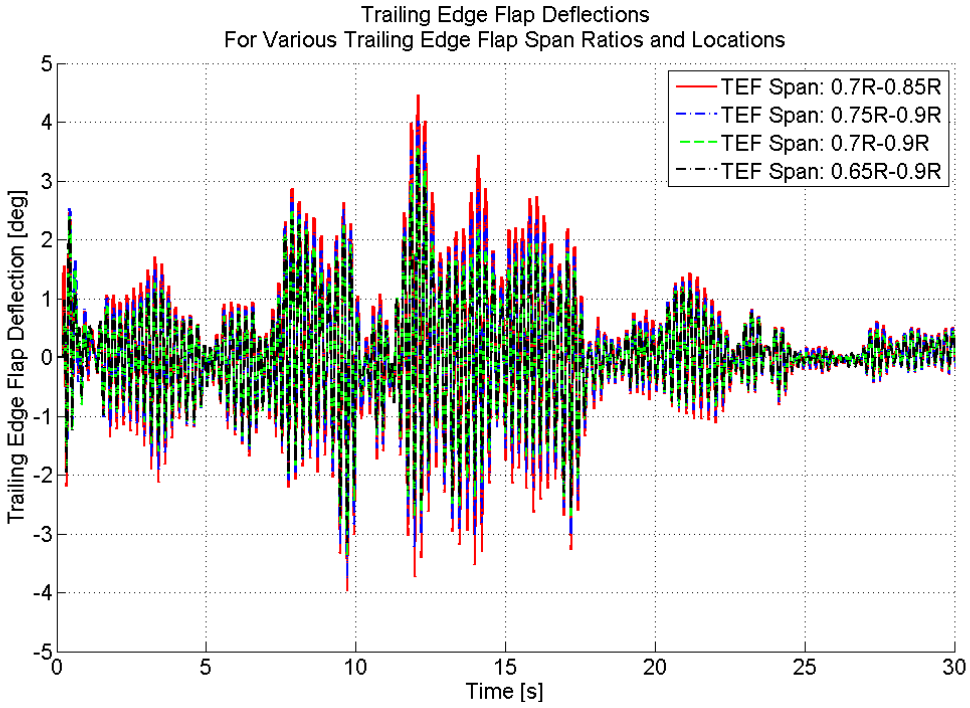

Figure C.11. TEF Deflections: Varying TEF Span Ratio and Location

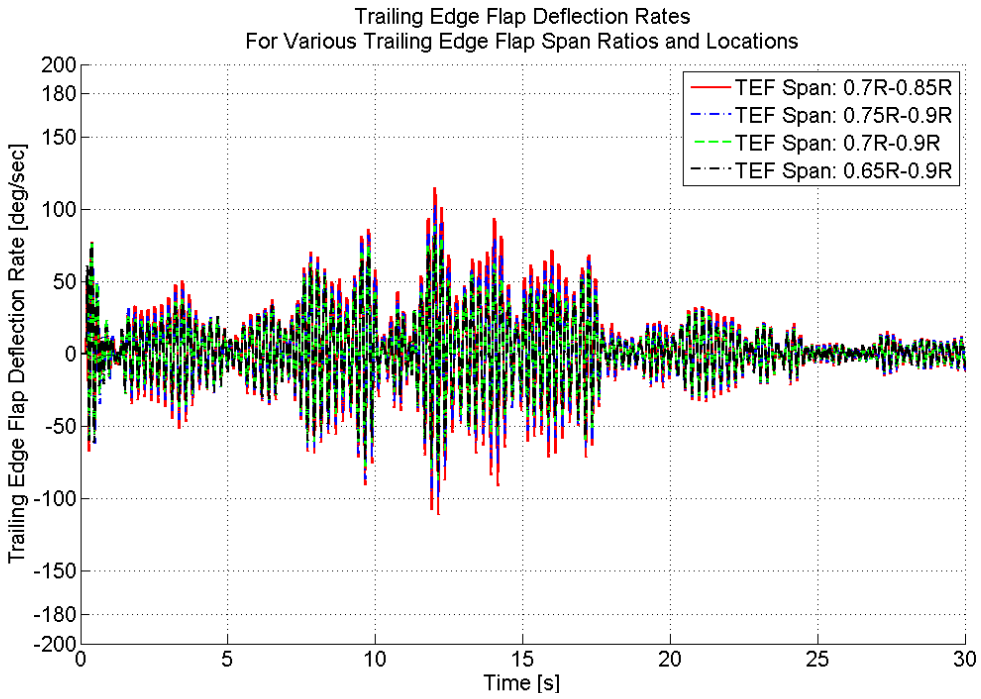

Figure C.12. TEF Deflection Rates: Varying TEF Span Ratio and Location

C.2.2 Varying TEF Chord Ratio

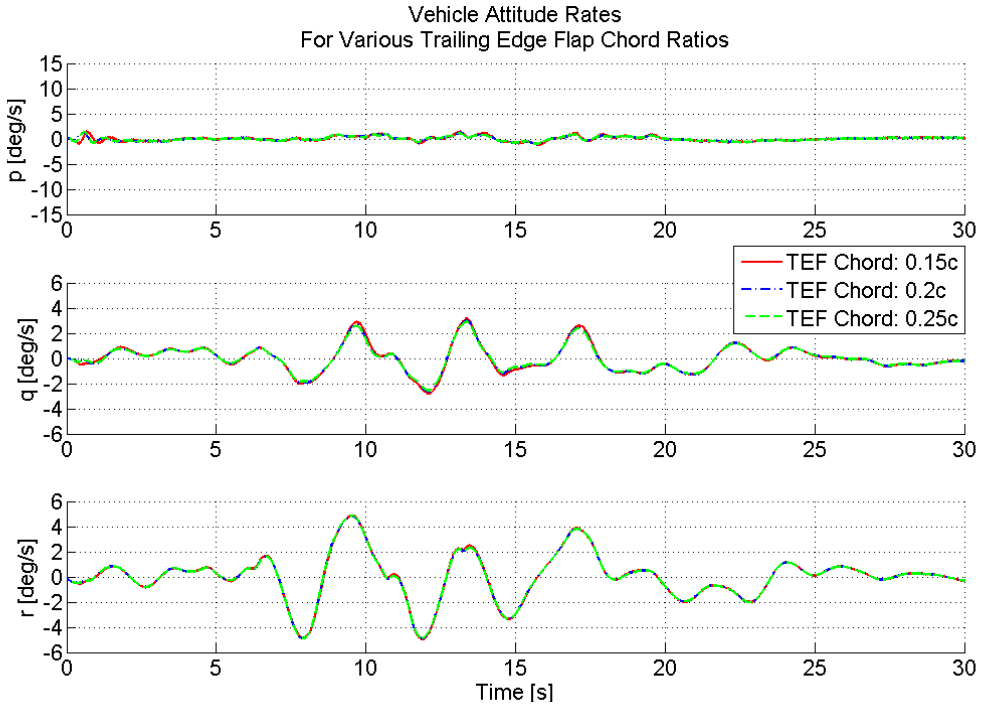

Figure C.13. Vehicle Attitude Rates: Varying TEF Chord Ratio

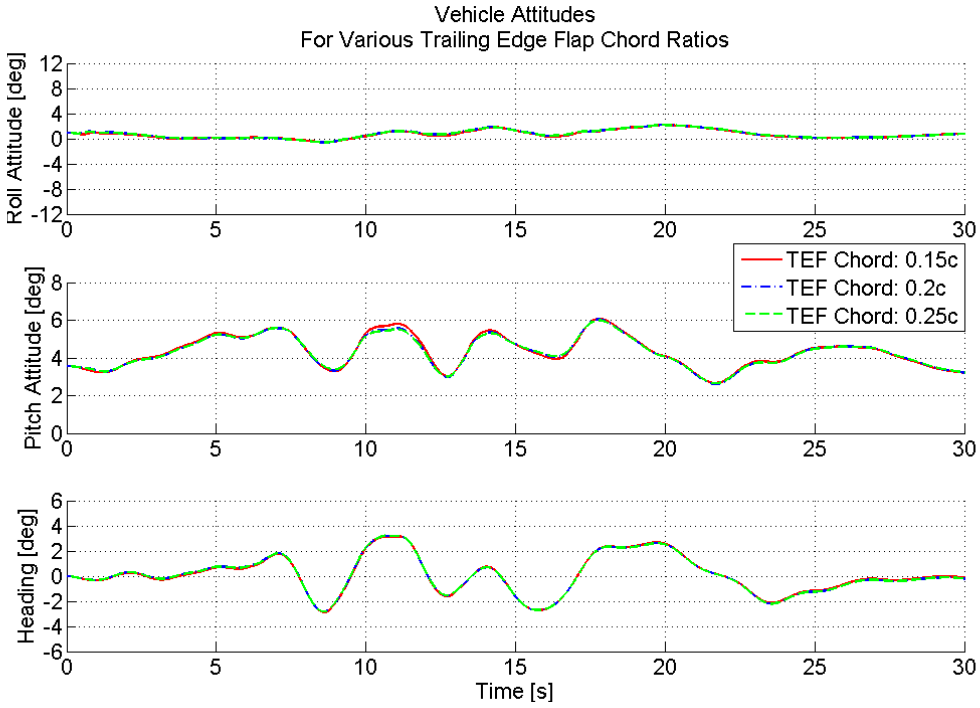

Figure C.14. Vehicle Attitudes: Varying TEF Chord Ratio

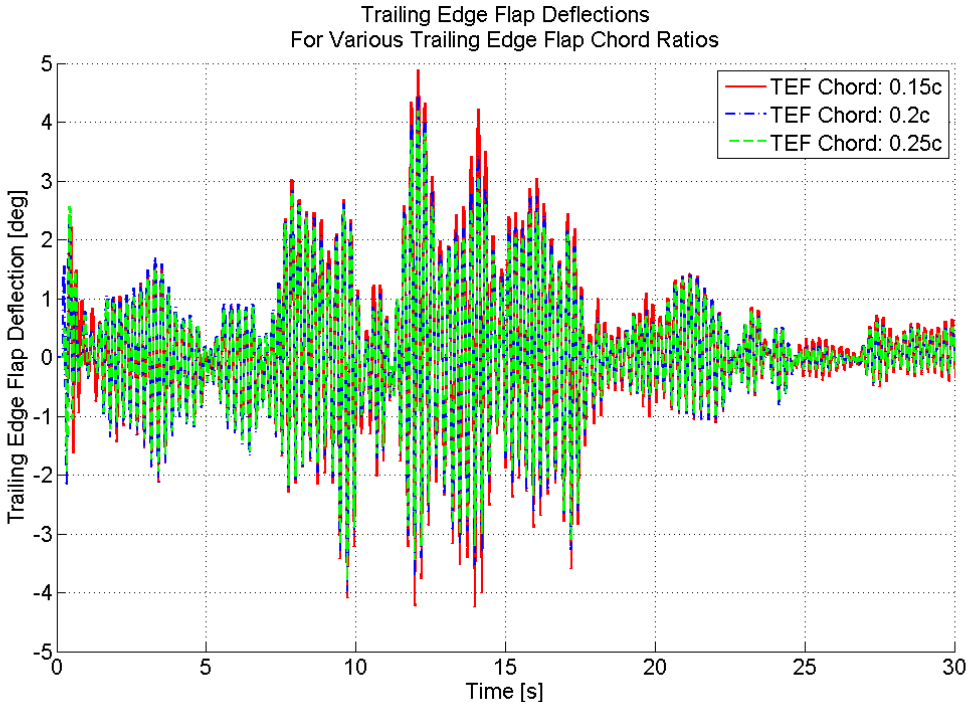

Figure C.15. TEF Deflections: Varying TEF Chord Ratio

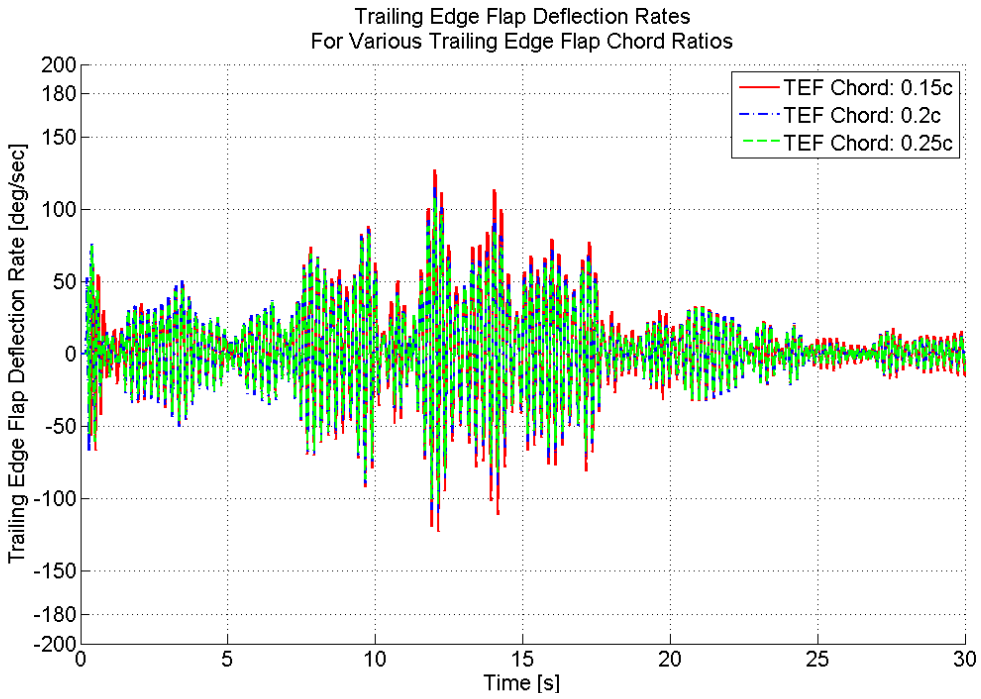

Figure C.16. TEF Deflection Rates: Varying TEF Chord Ratio

C.3 Off-Design Point Flight Condition Results

C.3.1 0-Degree, 30-Knot WOD Flight Condition Results

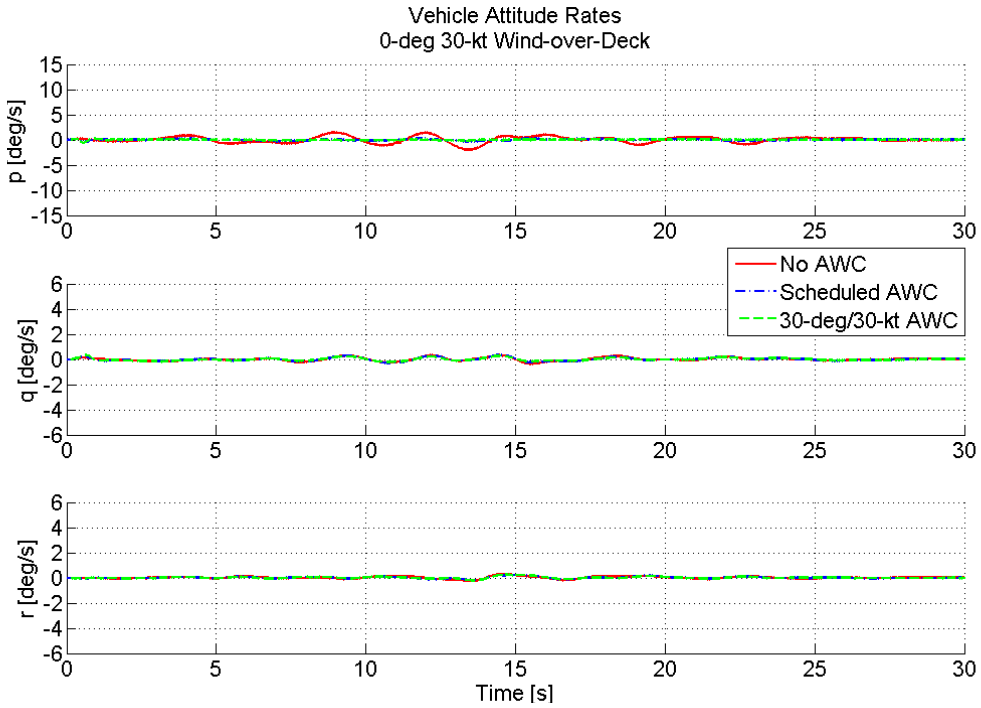

Figure C.17. Vehicle Attitude Rates: 0-degree, 30-knot Wind-over-Deck

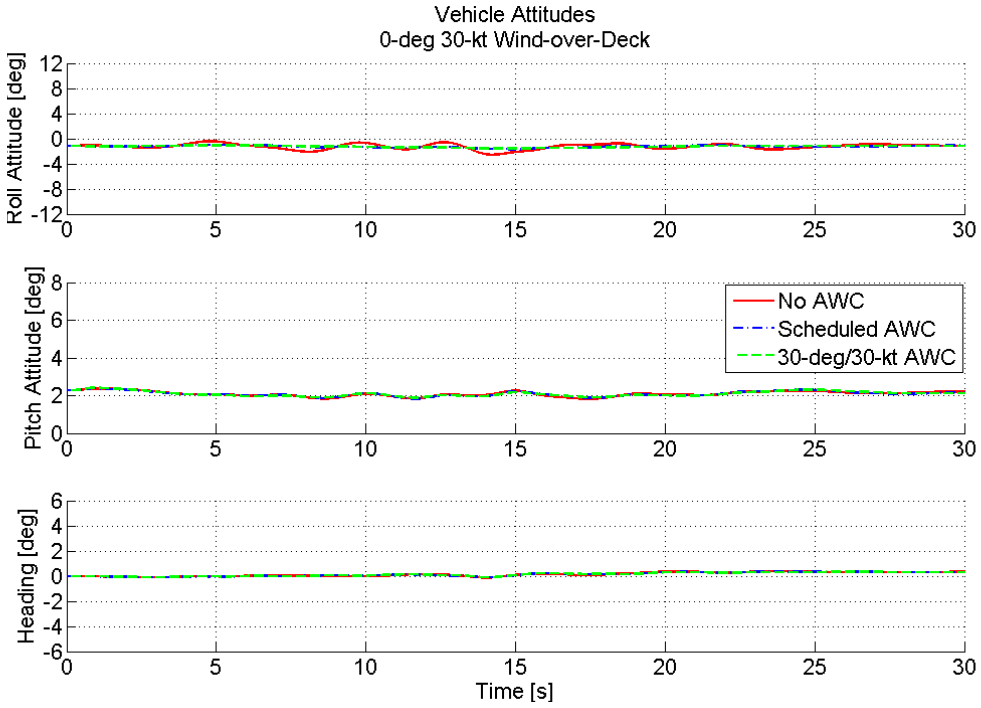

Figure C.18. Vehicle Attitudes: 0-degree, 30-knot Wind-over-Deck

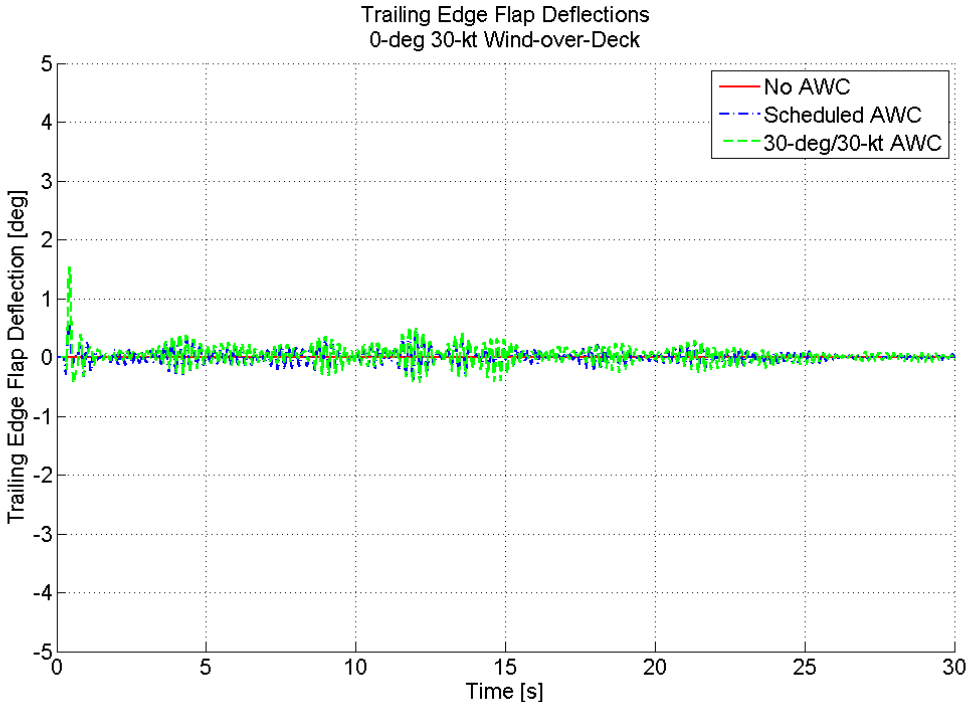

Figure C.19. TEF Deflections: 0-degree, 30-knot Wind-over-Deck

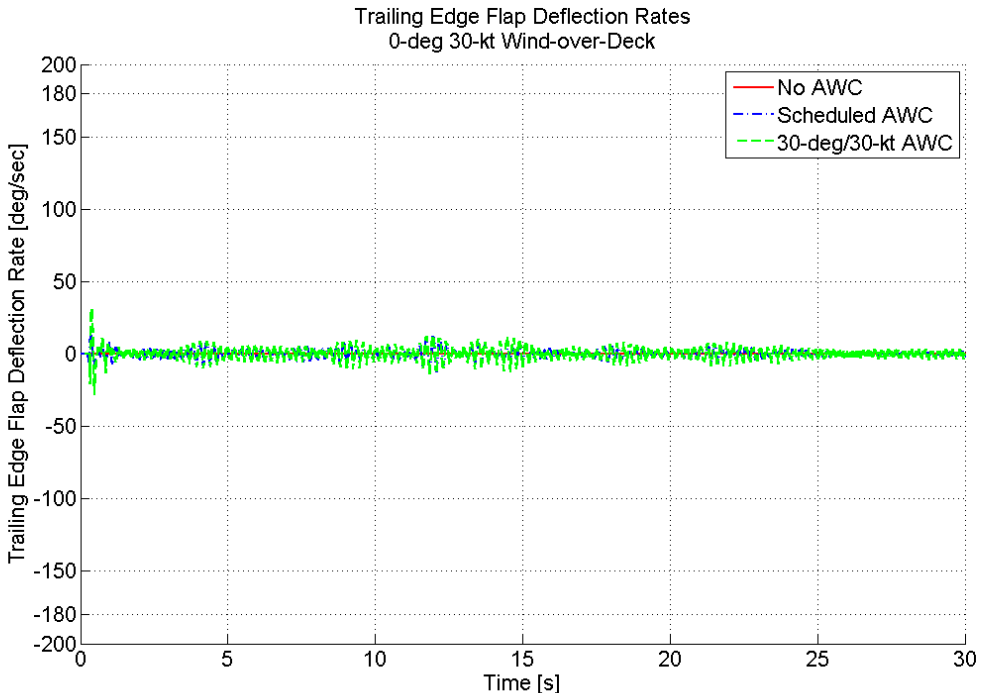

Figure C.20. TEF Deflection Rates: 0-degree, 30-knot Wind-over-Deck

C.3.2 0-Degree, 40-Knot WOD Flight Condition Results

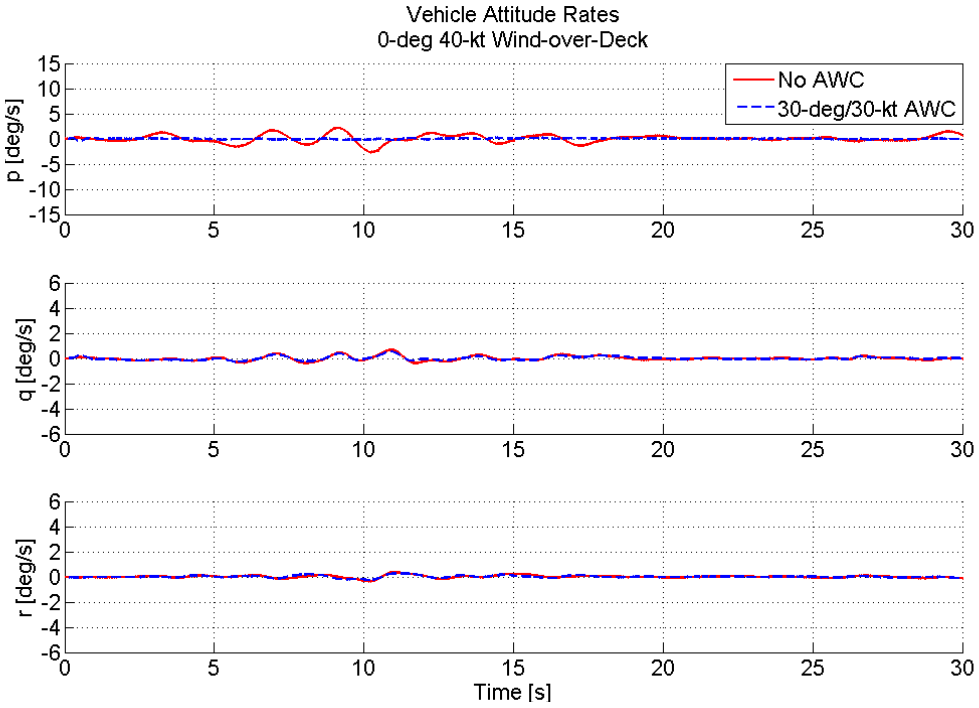

Figure C.21. Vehicle Attitude Rates: 0-degree, 40-knot Wind-over-Deck

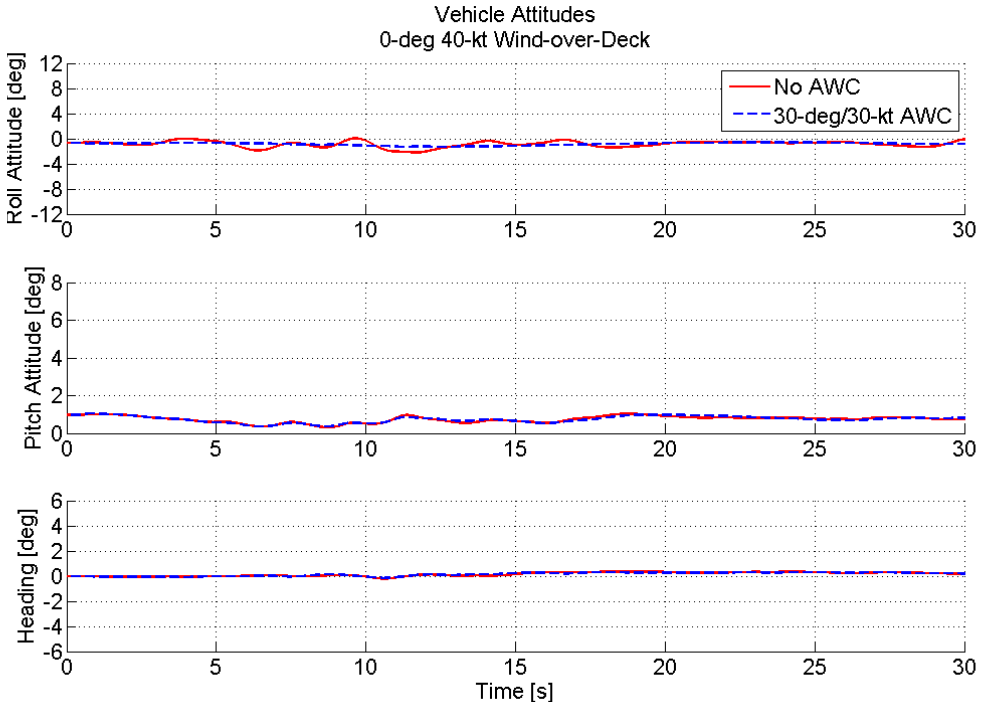

Figure C.22. Vehicle Attitudes: 0-degree, 40-knot Wind-over-Deck

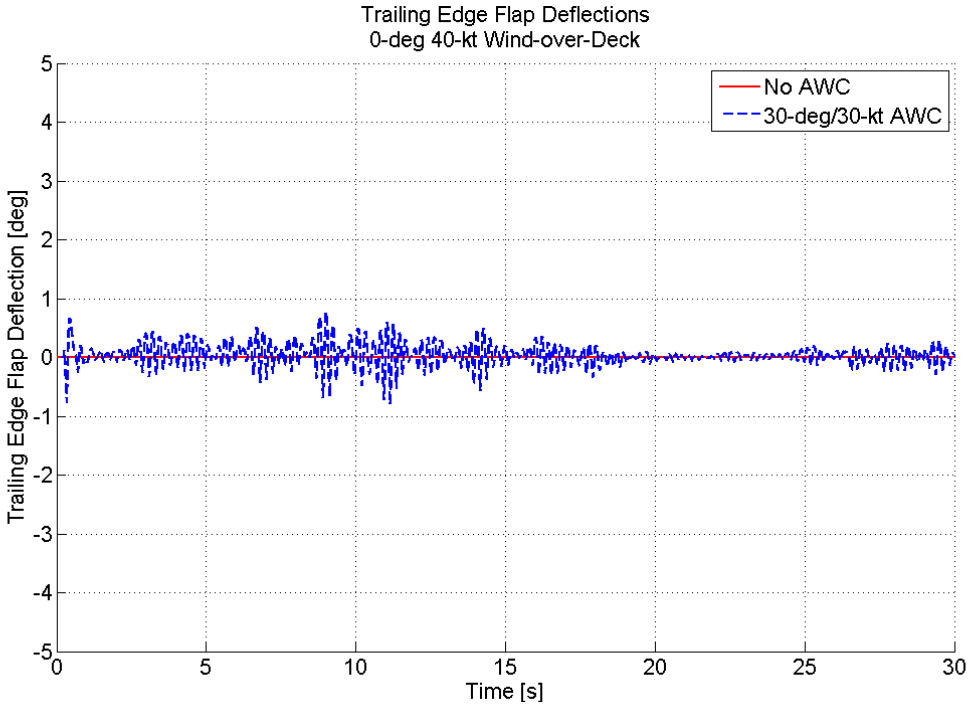

Figure C.23. TEF Deflections: 0-degree, 40-knot Wind-over-Deck

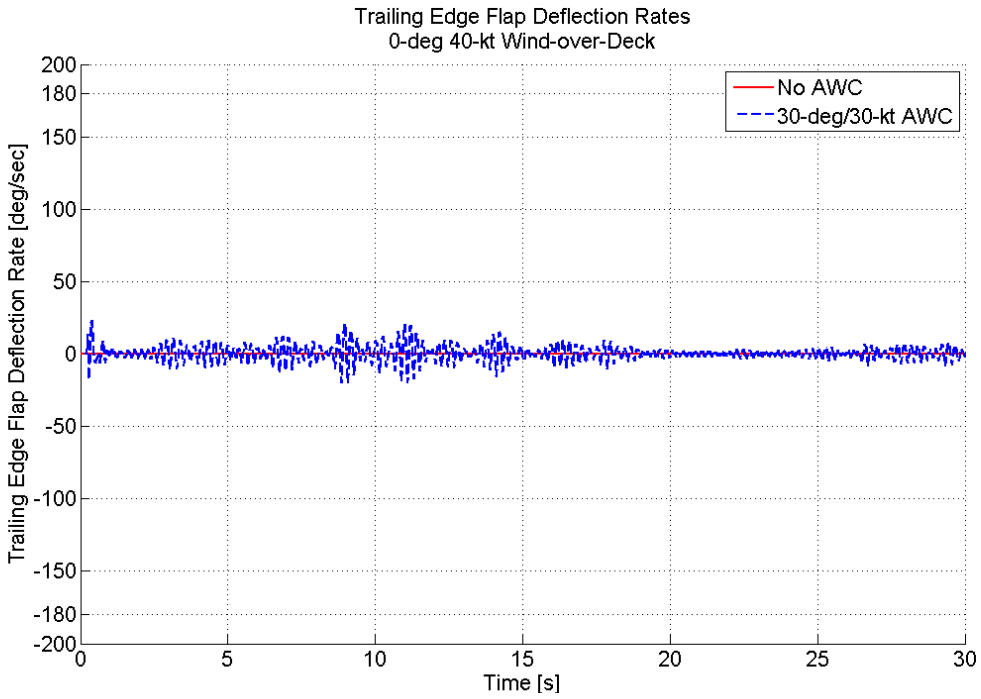

Figure C.24. TEF Deflection Rates: 0-degree, 40-knot Wind-over-Deck

Bibliography

[1] Wilkinson, C.H., Roscoe, M.F., and VanderVliet, G.M., "Determining Fidelity Standards for the Shipboard Launch and Recovery Task," *Proceedings of the AIAA Modeling and Simulation Technologies Conference and Exhibit*, Montreal, Canada, August 2001.

[2] Perrins, J.A. and Howitt, J., "Development of a Pilot Assisted Landing System for Helicopter / Ship Recoveries," *Proceedings of the American Helicopter Society* 57^{th} *Annual Forum*, Washington, D.C., May 2001.

[3] Lee, D. and Horn, J.F., "Optimization of a Helicopter Stability Augmentation System for Operation in a Ship Airwake," *Proceedings of the American Helicopter Society* 61^{st} *Annual Forum*, Grapevine, TX, June 1 – 3, 2005.

[4] Horn, J.F., Bridges, D.O., and Lee, D., "Flight Control Design for Alleviation of Pilot Workload during Helicopter Shipboard Operations," *Proceedings of the American Helicopter Society* 62^{nd} *Annual Forum*, Phoenix, AZ, May 9 – 11, 2006.

[5] Horn, J.F., and Bridges, D.O., "A Model Following Controller Optimized for Gust Rejection during Shipboard Operations," *Proceedings of the American Helicopter Society* 63^{rd} *Annual Forum*, Virginia Beach, VA, May 1 – 3, 2007.

[6] Domke, B., "AH-64A, Paris Airshow," `http://www.b-domke.de/AviationImages/Rotorhead/4191.html` (June 2001).

[7] Shen, J., "Comprehensive Aeroelastic Analysis of Helicopter Rotor with Trailing Edge Flap for Primary Control and Vibration Control," Ph.D. Thesis, Department of Aerospace Engineering, The University of Maryland, College Park, MD, 2003.

[8] Dieterich, O., Enenkl, B., and Roth, D., "Trailing Edge Flaps for Active Rotor Control Aeroelastic Characteristics of the ADASYS Rotor System," *Proceed-*

ings of the 62^{nd} *Annual Forum of the American Helicopter Society*, Phoenix, AZ, May 9 – 11, 2006.

[9] Liu, L., Friedmann, P.P., Kim, I., Bernstein, D.S., "Simultaneous Vibration Reduction and Performance Enhancement in Rotorcraft Using Actively Controlled Flaps," *Proceedings of the* 47^{nd} *AIAA/ASME/ASCE/AHS/ASC Structures, Structural Dynamics, and Materials Conference*, Newport, RI, May 1-4, 2006.

[10] Milgram, J., "A Comprehensive Aeroelastic Analysis of Helicopter Main Rotor with Trailing Edge Flaps for Vibration Reduction," Ph.D. Thesis, Department of Aerospace Engineering, The University of Maryland, College Park, MD, 1997.

[11] Kim, J.S., "Design and Analysis of Rotor Systems with Multiple Trailing Edge Flaps and Resonant Actuators," Ph.D. Thesis, Department of Aerospace Engineering, The Pennsylvania State University, University Park, PA, December 2005.

[12] Li, L., Friedmann, P.P., and Patt, D., "Simultaneous Vibration and Noise Reduction in Rotorcraft – Practical Implementation Issues," *Proceedings of the* 46^{th} *AIAA/ASME/ASCE/AHS/ASC Structures, Structural Dynamics, and Materials Conference*, Austin, TX, April 18 – 21, 2005.

[13] Patt, D., Li, L., and Friedmann, P., "Active Flaps for Noise Reduction: A Computational Study," *Proceedings of the* 61^{st} *Annual Forum of the American Helicopter Society*, Grapevine, TX, June 1– 3, 2005.

[14] Straub, F., and Kennedy, D., "Design, Development, Fabrication and Testing of an Active Flap Rotor System," *Proceedings of the American Helicopter Society* 61^{st} *Annual Forum*, Grapevine, TX, June 1 – 3, 2005.

[15] Lee, D., "Simulation and Control of a Helicopter Operating in a Ship Airwake," Ph.D. Thesis, Department of Aerospace Engineering, The Pennsylvania State University, University Park, PA, August 2005.

[16] Padfield, G.D., *Helicopter Flight Dynamics: The Theory and Application of Flying Qualities and Simulation Modeling*, AIAA Education Series, Virginia, 1996.

[17] Howlett, J.J., "UH-60A Black Hawk Engineering Simulation Program: Volume I – Mathematical Model," NASA CR-177542 USAAVSCOM TR 89-A-001, September 1989.

[18] Lee, D., Sezer-Uzol, N., Horn, J.F., and Long, L.N., "Simulation of Pilot Control Activity during Helicopter Shipboard Operations," *AIAA Journal of Aircraft*, Vol. 42, No. 2, March – April 2005, pp. 448 – 461.

[19] Clement, W.F., Gorder, P.J. and Jewell, W.F., "Development of a Real-Time Simulation of a Ship-Correlated Airwake Model Interfaced with a Rotorcraft Dynamic Model," Technical Report TR-91-C-0176, The Naval Air Systems Command, 1991.

[20] Labows, S.J., Blanken, C.L, and Tischler, M.B., "UH-60 Black Hawk Disturbance Rejection Study for Hover/Low Speed Handling Qualities Criteria and Turbulence Modeling," *Proceedings of the American Helicopter Society* 56^{th} *Annual Forum*, Virginia Beach, VA, May 2000.

[21] Lusardi, J.A., Tischler, M.B., Blanken, C.L., and Labows, S.J., "Empirically Derived Helicopter Response Model and Control System Requirements for Flight in Turbulence," *Journal of the American Helicopter Society*, Vol. 49, No. 3, July 2004, pp. 340 – 349.

[22] Bluman, J.E., "Reducing Trailing Edge Flap Deflection Requirements in Primary Control Through a Moveable Horizontal Tail," M.S. Thesis, Department of Aerospace Engineering, The Pennsylvania State University, University Park, PA, May 2008.

[23] Shen, J. and Chopra, I., "A Parametric Design Study for a Swashplateless Helicopter Rotor with Trailing-Edge Flaps," *Proceedings of the* 58^{th} *Annual Forum of the American Helicopter Society*, Montreal, Canada, June 11– 13, 2002.

[24] Ormiston, R.A., "Aeroelastic Considerations for Rotorcraft Primary Control with On-Blade Elevons," *Proceedings of the* 57^{th} *Annual Forum of the American Helicopter Society*, Washington, DC, May 2001.

[25] Straub, F.K. and Charles, B.D., "Aeroelastic Analysis Of Rotors With Trailing Edge Flaps Using Comprehensive Codes," *Journal of the American Helicopter Society*, Vol. 46, No. 3, July 2001, pp. 192 –199.

[26] Theodorsen, T., "General Theory of Aerodynamic Instability and the Mechanism of Flutter," Technical Report No. 496, NACA, 1935.

[27] Stevens, P.L., "Active Interrogation of Helicopter Main Rotor Faults Using Trailing Edge Flap Actuation," Ph.D. Thesis, Department of Mechanical Engineering, The Pennsylvania State University, University Park, PA, May 2001.

[28] Leishman, J.G., "Unsteady Lift of a Flapped Airfoil by Indicial Concepts," *Journal of Aircraft*, Vol. 31, No. 2, March – April 1994, pp. 288 – 297.

[29] Hariharan, N., "Unsteady Aerodynamics of a Flapped Airfoil in Subsonic Flow Using Indicial Concepts," M.S. Thesis, Department of Aerospace Engineering, University of Maryland, College Park, MD, 1995.

[30] Jose, A., Sitaraman, J., and Baeder, J., "An Investigation Into the Aerodynamics of Trailing Edge Flap and Flap-Tab Airfoils Using CFD and Analytical Methods," *Proceedings of the* 63^{rd} *Annual Forum of the American Helicopter Society*, Virginia Beach, Virginia, May 1 – 3, 2007.

[31] Myrtle, T., and Friedmann, P., "Application of a New Compressible Time Domain Aerodynamic Model to Vibration Reduction in Helicopters Using an Actively Controlled Flap," *Journal of the American Helicopter Society*, January 2001.

[32] Koratkar, N.A., and Chopra, I., "Analysis And Testing Of Mach-Scaled Rotor With Trailing-Edge Flaps," *AIAA Journal*, Vol. 38, No. 7, July 2000.

[33] Straub, F.K., et al., "Smart Material-Actuated Rotor Technology, SMART," *Journal of Intelligent Material Systems and Structures*, Vol. 15, April 2004.

[34] Szefi, J., et al., "Development of a Novel High Authority Piezoelectric Actuator for Rotor Blades with Trailing Edge Flaps," *Proceedings of the* 62^{nd} *Annual Forum of the American Helicopter Society*, Phoenix, AZ, May 9 – 11, 2006.

[35] Leishman, J.G., *Principles of Helicopter Aerodynamics*, Cambridge University Press, New York, NY, 2000.

[36] Lee, D., and Horn, J.F., "Simulation of Pilot Workload for a Helicopter Operating in a Turbulent Ship Airwake," *Journal of Aerospace Engineering – Proceedings of the Institute of Mechanical Engineers Part G*, Special issues on shipborne aviation, Vol. 219, November 2005, pp. 445 – 458.

[37] Haddan, W.M., and Bernstein, D.S., "Generalized Riccati Equations for the full- and reduced-order mixed-norm H_2/H_∞ standard problem," *Systems and Control Letters*, Vol. 14, Issue 3, pp. 185 – 197, 1990.

[38] Stevens, B.L. and Lewis, F.L., *Aircraft Control and Simulation, 2nd Edit.*, John Wiley & Sons, Inc., Hoboken, N.J., 2003, p. 202.